Electronic Theses and Dissertations   Graduate School

2017

Final Muon Cooling For A Muon Collider

John Gabriel Acosta Castillo
University of Mississippi

Recommended Citation

FINAL MUON COOLING FOR A MUON COLLIDER

A Dissertation
presented in partial fulfillment of requirements
for the degree of Doctor of Philosophy
in the Department of Physics and Astronomy
The University of Mississippi

by

JOHN GABRIEL ACOSTA CASTILLO

May 2017

ABSTRACT

To explore the new energy frontier, a new generation of particle accelerators is needed. Muon colliders are a promising alternative, if muon cooling can be made to work. Muons are 200 times heavier than electrons, so they produce less synchrotron radiation, and they behave like point particles. However, they have a short lifetime of 2.2 μs and the beam is more difficult to cool than an electron beam. The Muon Accelerator Program (MAP) was created to develop concepts and technologies required by a muon collider. An important effort has been made in the program to design and optimize a muon beam cooling system. The goal is to achieve the small beam emittance required by a muon collider. This work explores a final ionization cooling system using magnetic quadrupole lattices with a low enough $\beta^\star$ region to cool the beam to the required limit with available low Z absorbers.

DEDICATION

To my parents, to my friends and especially to Sandra Oliveros. For giving me the strength when I was weak, for giving me the faith that sometimes I do not have.

ACKNOWLEDGEMENTS

TABLE OF CONTENTS

LIST OF FIGURES

LIST OF TABLES

CHAPTER 1

INTRODUCTION

The discovery of the Higgs boson at a mass of 125 GeV/c^2 [1, 2] has increased the interest in the development of new lepton machines such as the $\mu^+\mu^-$ collider [3]. Colliding muons offers some advantages over other particles. Muons are 200 times heavier than electrons, so the synchrotron radiation is lower [4]. Also, the collision energy is concentrated in a single point and high mass events can be created with less center of mass energy. For example, for proton collisions the center of mass energy (c.m.) is distributed over all partons that constitute the proton, reducing the effective c.m. collision energy. However, for muons the energy is all concentrated in the collision.

The new generation of muon colliders offers the opportunity to study the properties of the Higgs boson with precision. A $\mu^+\mu^-$ collision can directly produce a Higgs boson. The coupling is proportional to mass squared. New physics can be explored [5]. Production of a muon beam is not an easy task. The muon lifetime is short and to achieve a high muon flux the initial beam has to have a wide energy and transverse momentum spread. To introduce the muons into a collider ring the energy spread and transverse emittance has to be reduced to an acceptable level [6]. That is why the cooling section for the muon collider is crucial. A cooling scheme has been simulated showing a 6D normalized emittance reduction of almost a million to $\epsilon_{6D} = 0.123 \, \text{mm}^3$ [7]. However, the emittance required by a high luminosity muon collider is $\epsilon_{6D} = 0.044 \, \text{mm}^3$ [8], a factor of three lower.

This work will introduce the basic concepts needed to understand muon cooling and proposes a final cooling system scheme based on strong quadrupole focusing [9] that may make it possible to use the muon beam in a high luminosity muon collider ring. There

are several cooling techniques previously introduced to reduce beam emittance [10], but all of them take more time than ionization cooling , which is the focus of this work. Muons do not interact strongly and can tolerate the passage through absorbers that ionization cooling requires. In ionization cooling, strong focusing causes muons in a bunch to pass through absorbers at large angles to maximize the loss of transverse momentum within the bunch. Longitudinal momentum, which is also lost, is replaced by radio frequency cavities. Ionization cooling is being tested at the MUON Ionization Cooling Experiment (MICE) [11–14]. MICE also may be able to measure 6D cooling by doing longitudinal to transverse emittance exchange with a polyethylene wedge [15–17]. Higher momentum muons pass through the thicker part of the wedge. See Fig. 1.1.
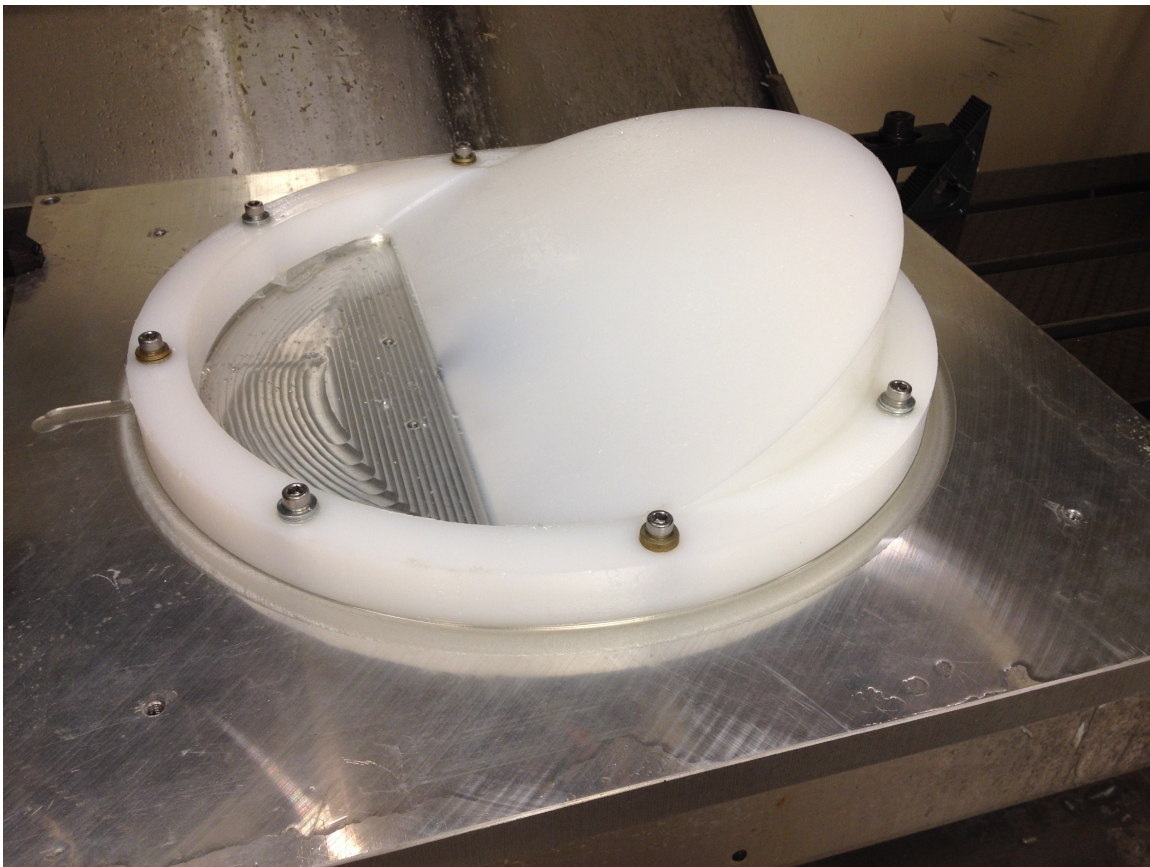
Figure 1.1. Half of a polyethylene wedge for possible use in MICE for emittance exchange.

CHAPTER 2

MUON COLLIDER OVERVIEW

Particle colliders have been used over decades to explore particle interactions and the structure of matter. Quantum field theories have been tested and verified using particle accelerator technology as a tool. A whole new physics branch was developed from the study of subatomic particle interactions.

When the first colliders were developed, the obvious choice was to use electrons and positrons as particles to collide. They are easy to produce and were well known at that time. Even now they are used for collisions and are considered as a valid option for future colliders. Electrons do not have internal structure, that is why electrons are elementary particles. But, in circular colliders, when the particles bend, they lose energy by generating synchrotron radiation. The energy lost by the beam on each orbit is absorbed by the magnets and has to be recovered using radio frequency cavities. It makes the energy consumption high, imposing a limit on the collision energy set by cost and collider ring size.

Another generation of colliders uses protons instead of electrons. The main advantage is that the proton's mass is larger than the electron mass and synchrotron radiation decreases as the fourth power of mass. But protons are not elementary particles, they have internal structure. So, the energy lost by synchrotron radiation is less, but the kinetic energy is distributed over all the constituent quarks and gluons. The momenta of the quarks and gluons is not known, so hadronically produced events contain more backgrounds than those produced at a lepton collider.

Both electron-positron and proton-antiproton colliders use antiparticles that have to be produced first. The most common process to generate antiparticles is to collide a beam

3

with a fixed target. The required antiparticles are selected from all the out going particles. During antiproton production, many pions are produced and usually thrown away. Pions are not elementary particles, they decay into muons that are basically heavy electrons.

Circa 1975, initial concepts to collect, store, and collide muons were proposed. See for example Refs. [18,19]. By the turn of the millennium, preliminary design reports [20–23] were in place, but muon cooling was not complete. In 2011, The Muon Accelerator Program (MAP) was created to develop concepts and technologies required by a muon collider. An important effort has been made in the program in order to design and optimize cooling for muon beams [24].

2.1   Muon Collider Scheme

The muon collider design has been developed for more than 40 years since it was proposed. It is a main goal of the MAP (Muon Accelerator Program). A description of the project is presented in Ref. [6].
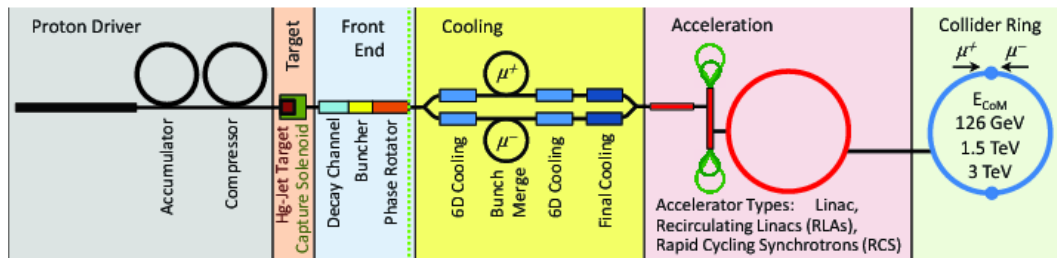
Figure 2.1. Proposed muon collider scheme (MAP) [25]

A proposed muon collider complex is divided in several sections [25]. The first section is where the protons collide with a mercury jet target to produce pions. They are collected by magnets that guide the pions into a beam [26, 27]. Then, they decay into muons and neutrinos producing a strong beam of neutrinos, that might be used by other experiments, and a beam of muons with high initial beam emittance. The second section is designed to reduce the beam emittance to a level that the accelerator section and the collider ring need. Finally, the accelerator section increases the energy and injects the beam into the ring

4

collider where the final collisions occur.

2.1.1 Proton Driver and Front End

A high-intensity proton driver makes a 3 GeV proton beam impact a liquid metal target. The collisions create large numbers of pions. These pions are captured with a high field solenoid and allowed to decay. The out coming muons have a momentum of about 200 MeV/c. According to the upgraded Project X report [28] a source for a 4 MW proton beam will produce approximately 10^{21} muons per year [29]. The current design assumes short (~ 2 ns) bunches of intense protons (2×10^{14}) at a 15 Hz repetition rate. This high intensity pulsed beam heats the carbon target, which is eventually damaged by the beam. An alternative is to use a liquid-metal mercury jet that is continually remade. Mercury was tested by the MERIT experiment at CERN [30].

The pions produced have a wide energy spread. The energy spread needs to be reduced. To transport and focus the muons produced by the decays, a phase rotation has to be implemented as Fig. 2.2 shows. The initial beam travels through a 56 m drift space that makes the initial rotation, then a series of radio frequency cavities capture the beam in several bunches. Then, the bunches travel though another 36 meter long drift space that allows them to rotate, and finally another series of RF cavities accelerate the slower bunches and de-accelerate the faster bunches, making the final energy spread lower to transport the beam using 200 MHz RF cavities [31].

The out-coming positive and negative muons are mixed and they have to be separated. A system composed of bending solenoids and a septum can be used to create dispersion and slice the beams into two beams separating the opposite charges. Another option is to cool the beam and separate the charges after the initial cooling.
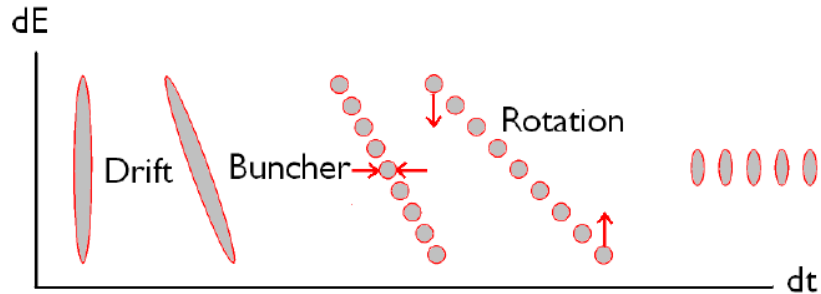
Figure 2.2. Phase rotation concept. The energy spread of muons is lowered at the cost of spreading the muons out in space.

2.2 Muon Cooling

The resulting muon beam has to be cooled in several stages until it can be inserted into an acceleration structure and finally into a collider ring. This is because the final beam emittance is a critical factor in the collider luminosity. Under current designs, the muon beam cooling systems will need to reduce the total 6D emittance by at least six orders of magnitude [32].

The muon beam is produced from a pion beam in the decays $\pi^+ \to \mu^+ \nu_\mu$ and $\pi^- \to \mu^- \bar{\nu}_\mu$. This muon production from the pion decay results in a beam with a high phase space volume. Accepting high emittance pion and muon beams is the only reasonable way to get enough muons. So, the cooling section is crucial for muon collider performance. Fig. 2.3 shows the cooling requirement for each stage.

There are several ways to reduce particle beam emittance. For muons, the fastest method is ionization cooling as Table 4.1 shows [10]. The main challenge for the muon collider is to reduce the beam emittance quickly and minimize the muon losses during the process. Several cooling schemes have been proposed. The two cooling schemes that have the lowest 6D final emittance are the Helical [33] and Rectilinear [7]. channels as Table 2.1 shows.

Both the helical and rectilinear cooling channels achieve good performance in simulation starting with a large initial emittance and reducing it to values close to the Muon

6
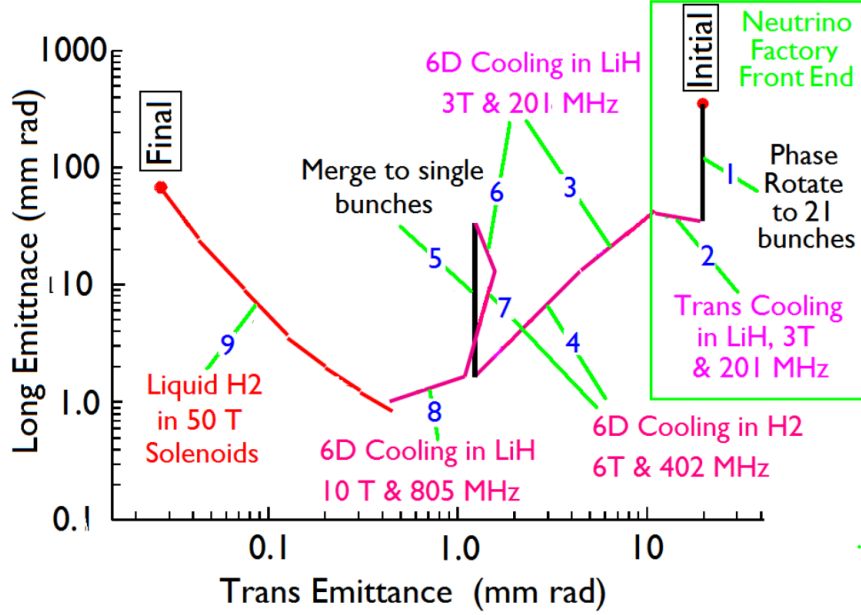
Figure 2.3. Transverse vs. longitudinal emittances before and after each stage [8].

Collider requirement. But, a somewhat cooler beam and higher muon collider luminosity would, of course, be better.

The purpose of this work is to propose a cooling scheme that take the emittance achieved by the rectilinear channel and reduces the emittance to the level that can achieve a higher collider luminosity. The input beam for this work is based on the final beam produced by the rectilinear channel. The channel design has to be consistent with the last rectilinear channel stage.

Table 2.1. Helical and Rectilinear Cooling Channel normalized RMS 6D emittances, ϵ_{6D}, from simulations and emittances required for a muon collider. The channels cool by over five orders of magnitude and need less than a factor of 10 more for a collider. The 21 bunches created after initial phase rotation are merged into one bunch during cooling [34].

| | ϵ_x | ϵ_y | ϵ_y | ϵ_{6D} |
	mm	mm	mm	mm^3
Initial Emittance [7]	48.6	48.6	17.0	40,200
Helical Cooling [33]	0.523	0.523	1.54	0.421
Rectilinear Cooling [7]	0.28	0.28	1.57	0.123
Muon Collider [8]	0.025	0.025	70	0.044

7

2.2.1 Rectilinear Muon Cooling Channel: Brief Description

So far, the Rectilinear Channel [7] achieves the lowest 6D emittance in simulation. The basic cell configuration uses two or four slightly tilted solenoids to focus the beam and to produce a dispersion zone, as Fig. 2.4 shows. Between every solenoid pair a low Z absorber is placed. The absorber has a wedge shape to allow emittance exchange as explained in Section 4.2.1. The wedge decreases longitudinal emittance at the cost of slowing the rate of transverse emittance reduction. The cell solenoids are followed by a set of radio frequency (RF) cavities that recover the longitudinal momentum lost in the absorbers. The RF cavities have been observed to suffer electrical breakdown in high magnetic fields [35, 36]. The addition of medium pressure hydrogen gas into the cavities has been shown experimentally to stop the breakdown [37, 38]. The Rectilinear cooling channel works in simulation with medium pressure hydrogen gas [39, 40]. Most of the energy loss is still in the discrete lithium hydride absorbers. Medium pressure hydrogen gas may also be able to neutralize space charge [41], possibly allowing shorter bunches.
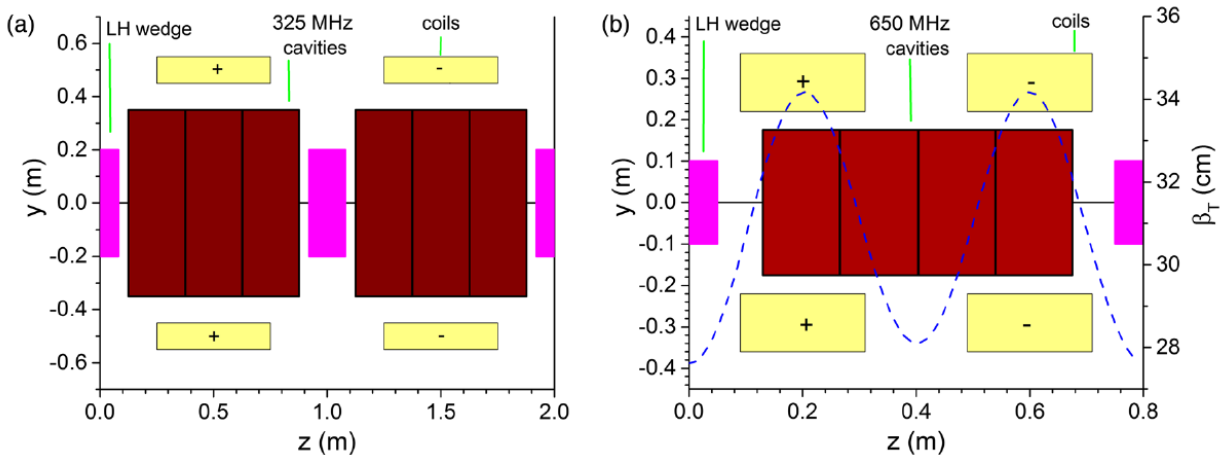
Figure 2.4. Rectilinear Channel solenoidal cell scheme [42].

The Rectilinear Channel is composed of 12 stages, four before bunch recombination and eight after. The total length is 970 meters. A tapered linear cooling channel [43] works better than a cooling ring [44]. The transverse betatron function can be reduced at every

8

stage to optimize the emittance reduction without losing the beam. The last stage needs solenoid magnets with magnetic fields up to 16 T. Superconductor magnets have magnetic field limits as Fig. 2.5 shows. The limit for Nb_3Sn conductor in solenoids is about 16 T.
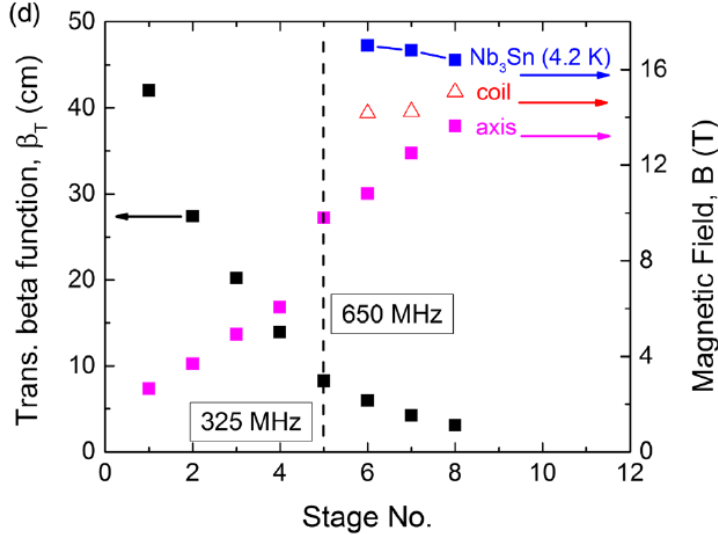
Figure 2.5. Magnetic field requirements for the Rectilinear Cooling Channel [42].

The 6D emittance may be small enough at the end of a cooling channel, but a collider needs a smaller transverse emittance and can tolerate a larger longitudinal than a cooling channel typically generates. Emittance exchange with septa [45] and/or wedges [46] may be a solution.

2.2.2 Acceleration

Radio frequency (RF) cavities are devices that quickly and efficiently accelerate muons to high energies. They also are set up to adjust the energy of a reference particle that arrive with certain phase angle ϕ_s. Particles receive an amount of energy that depends on their arrival time. Higher frequency RF cavities can be used with shorter bunch lengths. The beam momentum after the final muon cooling is about 400 MeV/c, and the muons have to be accelerated to a collision momentum of 63 GeV/c for the Higgs factory, and to higher momentum for an energy frontier muon collider. The acceleration has to be fast because

muons decay constantly. RF cavities cause the muons to gain energy and the bending magnets need to increase the magnetic field to guide the muons.
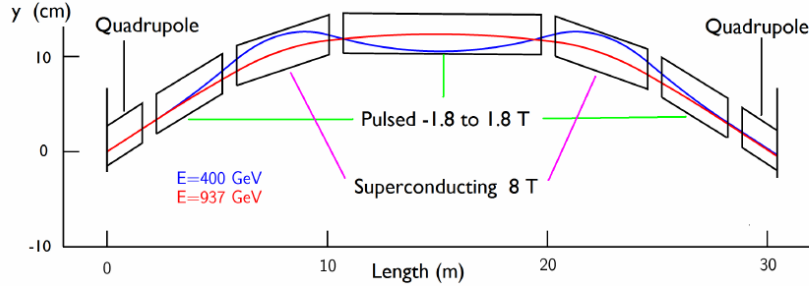
Figure 2.6. Hybrid muon synchrotron ring using interleaved fixed 8 T superconducting dipoles and ± 1.8 T rapid ramping dipoles [47].

To obtain a rapid acceleration into a ring a possible scheme was proposed in [47, 48]. To accelerate muon from 30 GeV to 750 GeV in 72 orbits, two rings of 1000 m radius are needed. The first ring accelerates muons from 30 GeV to 400 GeV in 28 orbits using 14 GV of 1.3 GHz superconducting RF. The second ring accelerates muons from 400 GeV to 750 GeV in 44 orbits using 1.3 GHz superconducting RFs. The second ring uses the magnets shown in Fig. 2.6. At this 1.5 TeV center of mass energy muons are ready to produce collisions. Muons that do not collide continue traveling along the ring and return to the collision point in a fraction of a second [49].

2.2.3 Ring Collider

The muon collider has to face several difficulties due to the relatively low muon lifetime. Accelerating muons to relativistic velocities will however increase the time that muons remain in a system. The average lifetime for muons is about $\tau \sim 2.2\,\mu$s. But, due to time dilation, the lab frame sees a longer lifetime. The relativistic dilation equation time is given by,

$$\tau_{\text{lab}} = \tau \times \gamma \tag{2.1}$$

10

where $\gamma = E/m_\mu$. Thus, at high energies this time increases enough to collect and collide the muons. Increasing the energy will increase the ring size. Therefore, muons will need to travel farther to collide. But, due to relativistic length contraction they will have ~ 1600 turns before decay with $8.33\,\mathrm{T}$ dipoles [18, 50]. Table 2.2 shows four possible accelerator ring scenarios. The accelerating rings magnetic packing fraction factor p_{factor} is taken to be about 67% with a bending magnetic field of 8.33 T, which are the LHC parameters [51].

Table 2.2. Accelerator ring scenarios for the Muon Collider.

Ring Name	$\sqrt{s}$ (TeV)	Ring Circumference (km)	τ_{Lab} s	Turns before decay
Higgs Factory	0.126	0.236	0.00131	1634
Multi-TeV Baseline	1.5	2.807	0.01559	1634
Multi-TeV Baseline	3	5.614	0.03118	1634
LEP Tunnel	14	26.198	0.14549	1634

The required radius R is calculated using eqn. 2.2, where p is the momentum in GeV/c and the magnetic field is given in Tesla.

$$R = \frac{1}{e}\frac{p}{B(p_{factor})} = \left(\frac{1}{0.2998}\frac{Tm}{GeV/c}\right)\frac{p(GeV/c)}{B(T)(p_{factor})} \tag{2.2}$$

Using a ring as large as the LHC ring, allows high energy and is a good place to accelerate muons. The LEP tunnel was built for leptons and is 100 meters underground and slightly tilted to send neutrino radiation below Lake Geneva and the Jura mountains on the other side. Thus, this is a perfect place to put a muon collider.

2.3   Luminosity Requirements

To be competitive, the muon collider should have an acceptable luminosity. This reduces the necessary time to get the 5σ signal required to claim a discovery. The basic luminosity equation to take into account is:

$$\mathcal{L} = \frac{\gamma N_{bunch}^2 f_0(DC)}{4\pi\epsilon_{x,y}\beta^\star} \tag{2.3}$$

taken from [32]. This equation depends on several variables. Each variable can be optimized in order to increase the luminosity.

- N_{bunch} : The beam inside of a collider is not a continuous beam. It is divided in several small packages called bunches that contain limited number of particles. The N_{bunch} variable is the number of muons that each bunch has.

- f_0 : is the frequency at which the bunches cross the interaction point. It depends on the number of bunches running in the ring and the ring circumference.

- DC : Duty cycle. This variable takes into account the fact that after each crossing, some muons are lost by collision, muon decays, and other reasons.

- $\epsilon_\perp$: the normalized rms transverse emittance is a quantity related to the temperature of particles inside each bunch. It is an important variable that measures the beam quality. It is related to the beam size.

- $\beta^\star$: is the betatron function in the collision region. It is related to bunch length.

The muon collider luminosity requirements will depend on the physics that scientists are interested in as Table 2.3 shows. According to the MAP project [25], a 6 TeV collider would be somewhat above 10^{34} cm^{-2} s^{-1} and a Higgs Factory considerably below this number.

Table 2.3. Luminosity parameters for Higgs factory and multi-TeV baselines [25]

Parameter	Units	Higgs Factory	multi-TeV Baseline
CM energy	TeV	0.125	1.5 to 6
Average $\mathcal{L}$	10^{34} cm^{-2} s^{-1}	0.001	1.25
β^*	cm	1.7	0.5 to 2
ϵ_T	π mm-rad	0.2	0.025
ϵ_L	π mm-rad	1.5	70

The variation of the beam parameters affect the luminosity in different ways. Some of them are limited by the collider physical configuration, while others can be optimized in order to increase the luminosity. Increasing the number of particles per bunch N_{bunch} has a huge impact on the luminosity increment. But, the number of muons that can be produced is limited. Designs already assume a 4 MW proton beam for muon production. Combining several bunches into one intense bunch increases the luminosity because it depends of N^2, but the current configuration already assumes just one bunch at the tune shift limit. Also the current configuration makes it difficult to increase the duty cycle DC or the collision frequency without introducing higher field dipoles into the collider ring. The variables that can be improved are $\epsilon_\perp$ and $\beta^\star$/bunch length. We are working to do this in this thesis.

The Higgs factory is not at the beam-beam tune shift limit, so going from one to four detectors as at LEP would quadruple the number of Higgs bosons observed. Energy frontier muon colliders are at the beam-beam tune shift limit, so a method of stabilizing beams between detectors for a few hundred orbits would have to be developed.

CHAPTER 3

BEAM OPTICS

A particle beam is defined as a group of particles that moves with almost equal kinetic energy in same direction. The particles are usually charged particles because they can be collected, accelerated, and driven by electromagnetic fields. Transport of the beam requires a high vacuum to avoid particle interaction with gas. Due to the mutual electric repulsion and subsequent defocusing, quadrupole magnets are needed to keep the particles in the beam without loss. Charged particles in constant magnetic fields generally move on a circular path due to the electromagnetic force that follows the Lorentz force equation:

$$F = \frac{e}{c}(\vec{v} \times \vec{B} + \vec{E}) = \frac{m_o \gamma \, v^2}{\rho} \tag{3.1}$$

Also, the transport system has different kinds of magnets to control the beam path such as quadrupoles, sextupoles, and dipole bending magnets. The reference trajectory usually is at the center of every element. Thus, only dipole magnets change the trajectory of a particle following the reference orbit. The reference orbit is usually take as a circular path or a straight line, if there are not bending magnets. All particles oscillate around the reference orbit as Fig. 3.1 shows. The longitudinal coordinate is labeled as $\hat{S}$ and the perpendicular coordinate $\hat{X}$ coincides with the $\hat{r}$ direction, and $\hat{Y}$ is perpendicular to $\hat{S}$ and $\hat{X}$.

3.1 Mathieu-Hill Equations

The systems to transport a particle beam are in general a periodic magnetic lattice that makes the beams particles oscillate around a reference point following linear or circular

14
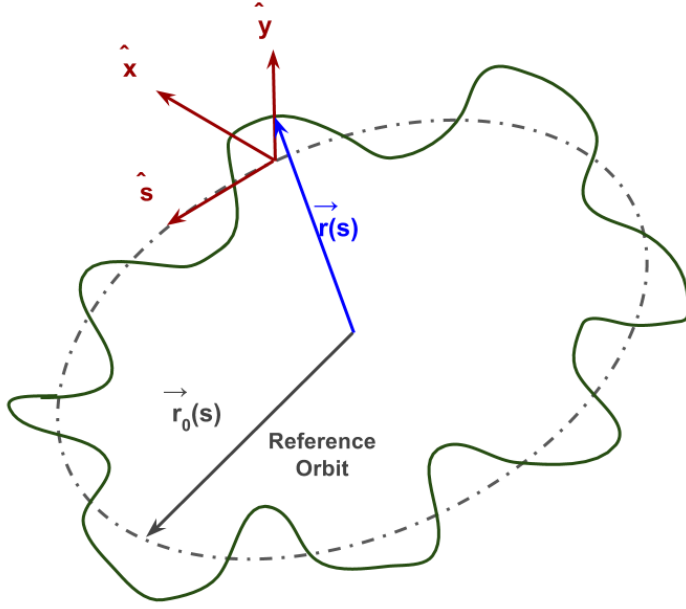
Figure 3.1. Coordinate system for a circular path.

trajectories. The dynamics of a beam particle on a periodic lattice is described by the Mathieu-Hill equations.

$$u'' + K(s)u = 0 \tag{3.2}$$

where u is a spatial coordinate and $K(s)$ is periodic restoration force $K(s) = K(z + L_p)$ with L_p as the periodic longitude.

$$K(s) = B'/(B\rho) + \rho^{-2} \tag{3.3}$$

Hill's equations have a solution in the form of:

$$u(s) = A\sqrt{\beta_s} \cos(\psi_s + \delta)) \tag{3.4}$$

$$u'(s) = -\frac{A}{\sqrt{\beta_s}} [\alpha_s \cos(\psi_s + \delta)) + \sin(\psi_s + \delta)] \tag{3.5}$$

where β_s is the amplitude function or betatron function, $\alpha_s = -\beta_s/2$, and ψ_s is the particle

phase advance. Every particle in the beam oscillates with amplitude β_s that satisfies the Courant-Snyder [52] invariant eqn. 3.6:

$$A^2 = \gamma_s u(s)^2 + u_s u_s' \beta_s + \alpha_s u'(s)^2 u(s)^2 \tag{3.6}$$

where $\alpha_s = \frac{-\beta'}{2}$ and $\gamma_s = \frac{1+\alpha_s^2}{\beta_s}$. The periodic solution of Hill's equation makes it possible to determine the beam behavior at any position in a periodic magnetic lattice if the initial conditions are given. Several lattice properties can be determined such as stability and beam admittance that will be explained in the following sections.

3.2   Emittance

When particles are collected into a beam they are moving in the same direction on average. But, the particles always have some momentum and position distribution with respect to the bunch center. In other words, they have a temperature with respect to the other particles in the same bunch. To quantify this beam characteristic, the dynamics of a beam bunch is described in a 6D phase space with coordinates x, P_x, y, P_y, s, E or $x, x', y, y', \sigma_z, \delta$. Each coordinate pair forms an ellipse. The emittance is defined as an area or volume in the phase space of the particles. The most common phase space for transverse variables is defined by:

$$u = x, y \tag{3.7}$$

$$u' = \frac{du}{ds} \tag{3.8}$$

For transverse emittance $\epsilon_\perp$ and x, y, x', y', the beam has a elliptical shape with area given by:

$$A = \pi\epsilon \tag{3.9}$$

$$\epsilon = \gamma_s u^2 + 2\alpha_s u u' + \beta_s u'^2 \tag{3.10}$$

The area in eqn. 3.10 is directly related to the Courant-Snyder invariant in eqn. 3.6. Fig. 3.2 shows a graphical representation of the ellipse shape and how it is related to the Courant-Snyder parameters.
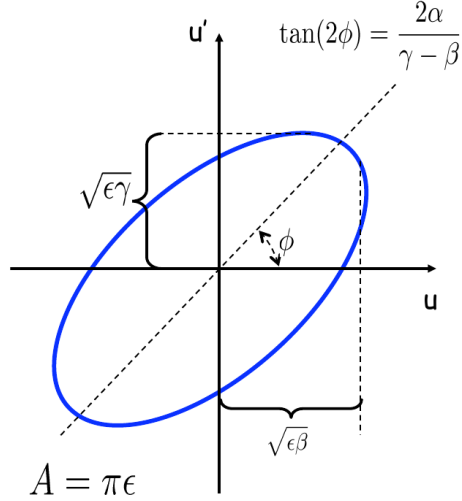
Figure 3.2. Phase space ellipse

The functions related to the ellipse area are:

- α_s - related to the beam tilt

- β_s - related to beam shape and size

- γ_s - dependent on α_s and β_s .

The Courant-Snyder parameters are measured from the u , u' distribution using eqn. 3.13,

$$\beta_s = < u^2 > /\epsilon_{rms} \tag{3.11}$$

$$\alpha_s = < u'^2 > /\epsilon_{rms} \tag{3.12}$$

$$\gamma_s = - < uu' > /\epsilon_{rms} = (1 - \alpha_s^2)/\beta_s \tag{3.13}$$

where term ϵ_{rms} is the beam emittance. The evolution of the $\beta_s, \alpha_s, \gamma_s$ functions can be

calculated using the transfer matrices for each magnetic element of the system, if the initial values are given. Similar treatment can be performed for the longitudinal emittance $\epsilon_\parallel$, but for this case the phase space is the momentum spread and the bunch length. The emittance in terms of the $u(s)$ and $u'(s)$ distribution relation described in eqn. 3.13 is represented as:

$$\Sigma = \begin{bmatrix} <u^2> & <uu'> \\ <uu'> & <u'^2> \end{bmatrix} = \epsilon_{rms} \begin{bmatrix} \beta & \alpha \\ \alpha & \gamma \end{bmatrix} \tag{3.14}$$

But, due to the large number of particles this description is impractical. The definition of the rms emittance ϵ_{rms} is given by:

$$\epsilon_{rms} = \sqrt{<u^2><u'^2> - <uu'>} \tag{3.15}$$

with normalized emittance defined as:

$$\epsilon_N = \epsilon_{rms}\beta\gamma \tag{3.16}$$

The admittance is defined as the maximum emittance that a magnetic lattice can accept and is defined as:

$$\text{Admittance} = \left[\pi \frac{a(s)^2}{\beta}\right] \tag{3.17}$$

3.3 Transfer Matrices

The solution of Hill's equation 3.5 lets us know the position of every particle, if the initial conditions and the magnetic restoration force is given. The transformation at any S point from the initial position in terms of matrices can be written as follows:

$$\begin{bmatrix} u_1 \\ u'_1 \end{bmatrix} = \begin{bmatrix} m_{11} & m_{12} \\ m_{21} & m_{22} \end{bmatrix} \begin{bmatrix} u_0 \\ u'_0 \end{bmatrix} \tag{3.18}$$

where the matrix elements $m_{i,j}$ are determined by the magnetic field that characterizes each component of the magnetic lattice. Every single element has it own transfer matrix. The transfer matrix for any system is the multiplication for each individual element transfer matrix, including drift spaces. See eqn. 3.19.

$$M_{system} = [M_{Q1}] \times [M_{D1}] \times [M_{Q2}] \times [M_{D2}] \times \ldots \tag{3.19}$$

Knowing the position of every beam particle is important for tracking and optimization tasks. But, the number of particles in a beam makes it impractical to use the transfer matrix 3.19 to describe the whole beam behavior. Fortunately, the Courant-Snyder invariant 3.6 is described in terms of three variables called Courant-Snyder parameters: $\alpha_s, \beta_s, \gamma_s$. These parameters can be found to any position in the magnetic lattice using the 3.18 matrix elements. The transformation for the Courant-Snyder Parameters is:

$$\begin{bmatrix} \gamma_1 \\ \alpha_1 \\ \beta_1 \end{bmatrix} = \begin{bmatrix} m_{22}^2 & -2m_{21}m_{22} & m_{21}^2 \\ -m_{12}m_{22} & m_{11}m_{22} + m_{12}m_{21} & -m_{11}m_{21} \\ m_{12}^2 & -2m_{12}m_{11} & m_{11}^2 \end{bmatrix} \begin{bmatrix} \gamma_0 \\ \alpha_0 \\ \beta_0 \end{bmatrix} \tag{3.20}$$

The Courant-Snyder parameters are useful tools. These parameters are related to the $u(s)$ and $u'(s)$ distributions at any point in the lattice as the relation 3.13 shows. Knowing these parameters, it is possible to determine the beam size and other useful lattice characteristics like the phase advance 3.21 $\Delta\psi$.

$$\Delta\psi = tan^{-1}\left(\frac{m_{12}}{\beta_1 m_{11} - \alpha_1 m_{12}}\right) \tag{3.21}$$

The parameter $\Delta\psi$ is calculated using only the parameters m_{11} and m_{12} and they depend only of the magnetic gradient of the elements and the particle momentum.Thus, $\Delta\psi$ has to be real for stable transmission and it determines the momentum range for lattice transport.

3.4   Transverse Quadrupole Focusing

For applications like colliders and cooling channels, it is necessary to focus the beam in a certain region. Focusing the beam minimizes the betatron function β_s in the target region. There are several ways to focus the beam using devices such as sector bending magnets, solenoids, and magnetic quadrupoles.

3.4.1   Quadrupole Magnets

Particle trajectories in a quadrupole field can be described using Hill's equation 3.5. The matrix formalism allows us to determine the Courant-Snider parameter evolution and to calculate where the betatron function will be a minimum. See eqn. 3.18. A quadrupole field shape is plotted in Fig. 3.3. Considering the central field lines, it is clear that the particles are focused in the $\hat{Y}$ direction, but they are defocused in the $\hat{X}$ direction. So, a quadrupole acts like a focusing lens in one dimension and a defocussing lens in the other. The transfer matrix is described in eqns. 3.22 and 3.23.

Focusing Quadrupole   **Defocusing Quadrupole**
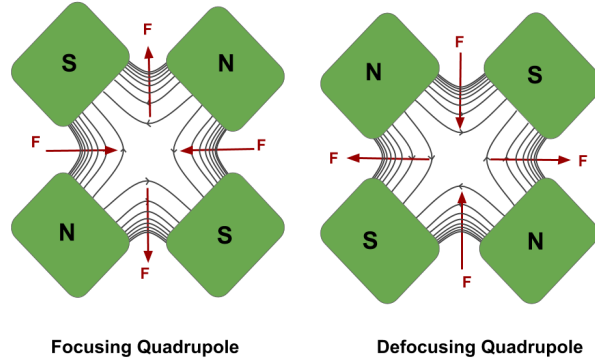
Figure 3.3. Transverse field lines for quadrupole magnets.

For the focusing plane the matrix is:

$$M_{focus} = \begin{bmatrix} cos(\sqrt{k}l) & \frac{sin(\sqrt{k}l)}{\sqrt{k}} \\ -(\sqrt{k})sin(\sqrt{k}l) & cos(\sqrt{k}l) \end{bmatrix} \tag{3.22}$$

For the de-focusing plane the matrix is:

$$M_{de-focus} = \begin{bmatrix} cosh(\sqrt{k}l) & \frac{sinh(\sqrt{k}l)}{\sqrt{k}} \\ sinh(\sqrt{k}l)/\sqrt{k} & cosh(\sqrt{k}l) \end{bmatrix}$$

(3.23)

To obtain effective focusing in both dimensions the quadrupoles have to be placed as a series of alternating focusing and defocusing elements. The most common configuration used to focus is the triplet focusing system, represented by thin lenses in Fig. 3.4. To calculate the β_s function evolution and get the minimum β_s position for the system, the matrix for each element, including the drift spaces between quadrupoles is multiplied to get the total transfer matrix for the focusing system.
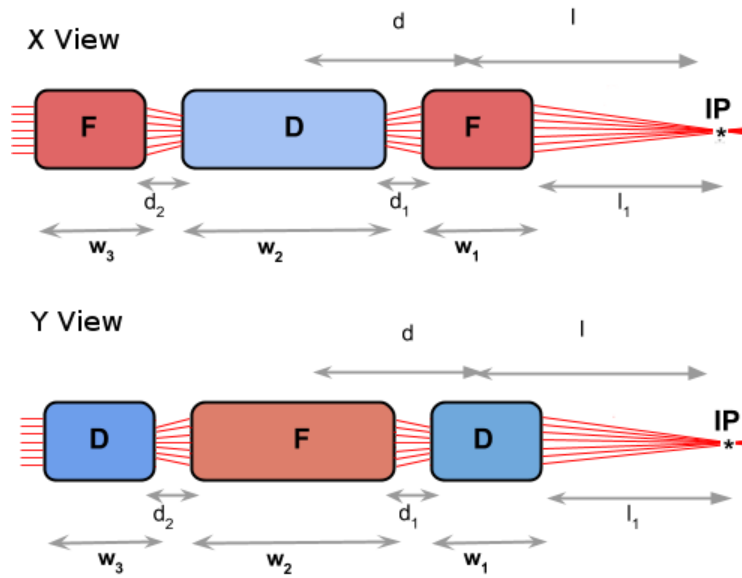
Figure 3.4. Focusing lens triplet: Focus-Defocus-Focus and Defocus-Focus-Defocus configurations.

The triplet focusing system has the transfer matrix shown in equation 3.24. It is estimated using the thin lens approximation as a single lens located at the center of each quadrupole.

$$M_{triplet} = \begin{bmatrix} 1 & 0 \\ -\frac{1}{f} & 1 \end{bmatrix} \tag{3.24}$$

If the triplet focal length is greater than the cell length, the approximation given by eqn. 3.26 is valid to approximate the magnetic strength for each quadrupole [53].

$$f_x = f_y = l + d \tag{3.25}$$

$$-f_1/l_1 = d/f_2 = -2d/f_3 = \pm\sqrt{2d/l_1 + d} \tag{3.26}$$

3.4.2   Average Betatron Functions in the Focus Region

For cooling purposes the average of the betatron function in a drift regions is more important than the minimum value. For a drift space the transfer matrix is:

$$M_{drift} = \begin{bmatrix} 1 & d \\ 0 & 1 \end{bmatrix} \tag{3.27}$$

For a drift space the Courant-Snyder matrix 3.19 becomes

$$\begin{bmatrix} \beta_1 \\ \alpha_1 \\ \gamma_1 \end{bmatrix} = \begin{bmatrix} 1 & -2L & L^2 \\ 0 & 1 & L \\ 0 & 0 & 1 \end{bmatrix} \begin{bmatrix} \beta_0 \\ \alpha_0 \\ \gamma_0 \end{bmatrix} \tag{3.28}$$

Thus, the expression for $< \beta_\perp >$ is given by:

$$< \beta_\perp > = \beta_0 - \alpha_0 L + \left(\frac{1+\alpha_0^2}{\beta_0} \right) \frac{L^2}{3} \tag{3.29}$$

3.5 Longitudinal Motion

The longitudinal motion treatment is similar to the matrix formalism described in previous sections for the transverse motion. The particles in the longitudinal dimension are accelerated and de-accelerated making oscillations with respect to the reference orbit as well. Here the main reasons for the oscillation is that off momentum particles follow different orbits in the magnetic fields or have different velocities. Particles arrive late or early with respect to the reference particle. In other words, the particle has a different phase advance according to its momentum.

Radio frequency cavities are set up to accelerate the reference particle giving an energy that depends on the ϕ_s angle and the radio frequency voltage gradient. Particles that arrive with different phase advances are displaced with respect to the reference particle angle. A particle that arrives late, gets more energy that another one that arrives early. So, the kick strength is higher for slower particles and weaker for faster particles. This effect is used to produce synchrotron focusing.

3.5.1 Energy Gain and Transit-time Factor

A particle that travels though a series of RF cavities does not feel a uniform field due to the gap within the RF cavities [54]. Thus, the effective field is reduced by a transit time factor. See eqn. 3.30.

$$T_{factor} = \frac{\sin(\pi L_{RF}/\beta\lambda_{RF})}{\pi L_{RF}/\beta\lambda_{RF}} \tag{3.30}$$

where e is the particle charge, L_{RF} is the radio frequency cavity length, β is the Lorentz relativistic factor, and λ is the wave length. The energy gain for a particle traveling in an RF cavity is given by equation 3.31.

$$\Delta E = eV_{grad}T_{factor}\cos(\phi_s) \tag{3.31}$$

23

where eV_{grad} is the maximum energy gain per transit and ϕ_s is the synchronous phase measured from the crest.

3.5.2   Longitudinal Transfer Matrix

The transfer matrix for the longitudinal motion is presented in eqn. 3.32 [55]. The matrix permits the transfer any S , δ phase space coordinate to any other position in the magnetic lattice.

$$M_{Longitudinal} = \begin{bmatrix} 1 + \frac{2\pi h\eta}{\beta^2 E_s} eV\cos(\phi_s) & \frac{2\pi h\eta}{\beta^2 E_s} \\ eV\cos(\phi_s) & 1 \end{bmatrix} \tag{3.32}$$

where the variables are defined as:

- $\phi_{n+1} = \phi_n + \frac{2\pi j\eta}{\beta_s^2}\Delta E_{n+1}$

- $\Delta E_{n+1} = \Delta E_n + eV(sin(\phi_n) - sin(\phi_s))$

- η rf station transversal index

- h harmonic number

- E Particle energy

- ϕ_s RF synchronous phase

- eV max energy gain per transit

- s synchronous quantity

Similar to the transverse transfer matrix, the longitudinal transfer matrix provides useful lattice properties such as the phase stability condition, eqn. 3.33. The determinant of the longitudinal transfer matrix has to be real for stable transmission.

$$0 < -\frac{\pi h\eta}{\beta_s^2 E_s} eV\cos(\phi_s) < 1 \tag{3.33}$$

24

3.5.3 Dispersion Function

Off momentum particles follow different trajectories with respect to the reference particle. Hill's equation for a particle with a momentum difference Δp is eqn. 3.34 [56].

$$x'' + \left(\frac{1 - \delta}{\rho^2(1 + \delta)} - \frac{K(s)}{1 + \delta} \right) x = \frac{\delta}{\rho(1 + \delta)} \tag{3.34}$$

where $\delta = \Delta p / p$. An off momentum particle moves at some X distance with respect to the reference orbit according to eqn. 3.35.

$$X = D(\rho, s)\delta \tag{3.35}$$

Only magnetic dipoles create dispersion. But, other magnetic elements, such as quadrupoles, can affect the dispersion function. The treatment of the dispersion function also uses transfer matrices. See eqn. 3.36.

$$\begin{bmatrix} D_{s1} \\ D'_{s1} \end{bmatrix} = M_{s1,s2} \begin{bmatrix} D_{s2} \\ D'_{s2} \end{bmatrix} + \begin{bmatrix} d \\ d' \end{bmatrix} \tag{3.36}$$

where $M_{s1,s2}$ is the transfer matrix for the magnetic element or lattice. As an example, components for a sector dipole are shown in eqns. 3.37 for $K_x > 0$ and 3.38 for $K_x < 0$.

$$\begin{bmatrix} d \\ d' \end{bmatrix} = \begin{bmatrix} \frac{1}{\rho K_x}(1 - \cos(\sqrt{K_x}s)) \\ \frac{1}{\rho K_x}(\sin(\sqrt{K_x}s)) \end{bmatrix} \tag{3.37}$$

$$\begin{bmatrix} d \\ d' \end{bmatrix} = \begin{bmatrix} \frac{1}{\rho K_x}(1 - \cosh(\sqrt{K_x}s)) \\ \frac{1}{\rho K_x}(\sinh(\sqrt{K_x}s)) \end{bmatrix} \tag{3.38}$$

where $K_x = (1/\rho^2)$, $\ell = \rho\theta$, and ℓ is the arc length of the sector magnet.

3.6 Chasman-Green Double-bend Achromat

For applications like chromaticity correction or emittance exchange Chasman-Green lattices are useful. They have zones with dispersion localized in a small region. It is desirable to have zero dispersion at the RF cavities location because the change in momentum affects the dispersion.

The right combination of bending dipole magnets and quadrupoles can made a system in which the dipole bend creates dispersion, which keeps increasing with the drift space. Then a quadrupole creates a constant dispersion function in the central region. The other half cell is a mirror image of the first part and reduces the dispersion to zero.

$$\begin{bmatrix} D_c \\ 0 \\ 1 \end{bmatrix} = \begin{bmatrix} 1 & 0 & 0 \\ -1/2f & 1 & 0 \\ 0 & 0 & 1 \end{bmatrix} \begin{bmatrix} 1 & L_1 & 0 \\ 0 & 1 & 0 \\ 0 & 0 & 1 \end{bmatrix} \begin{bmatrix} 1 & L & L\theta/2 \\ 0 & 1 & \theta \\ 0 & 0 & 1 \end{bmatrix} \begin{bmatrix} 0 \\ 0 \\ 1 \end{bmatrix} \tag{3.39}$$

$$f = \frac{1}{2}\left(L_1 + \frac{1}{2}L\right) \tag{3.40}$$

$$D_c = \frac{1}{2}\left(L_1 + \frac{1}{2}L\right)\theta \tag{3.41}$$

where f is the focal lengh, θ and L describe the dipole, and L_1 is the distance from the dipole end to the center [57]. See Fig. 3.5.

3.6.1 Chromaticity Correction

Bending and quadrupole magnets affect the trajectories of charged particles according to their momentum. Faster particles bend less than slower particles. Chromaticity correction can make all particles come to the same focus within a momentum range. The concept of chromaticity correction will be discussed in Chapter 7.
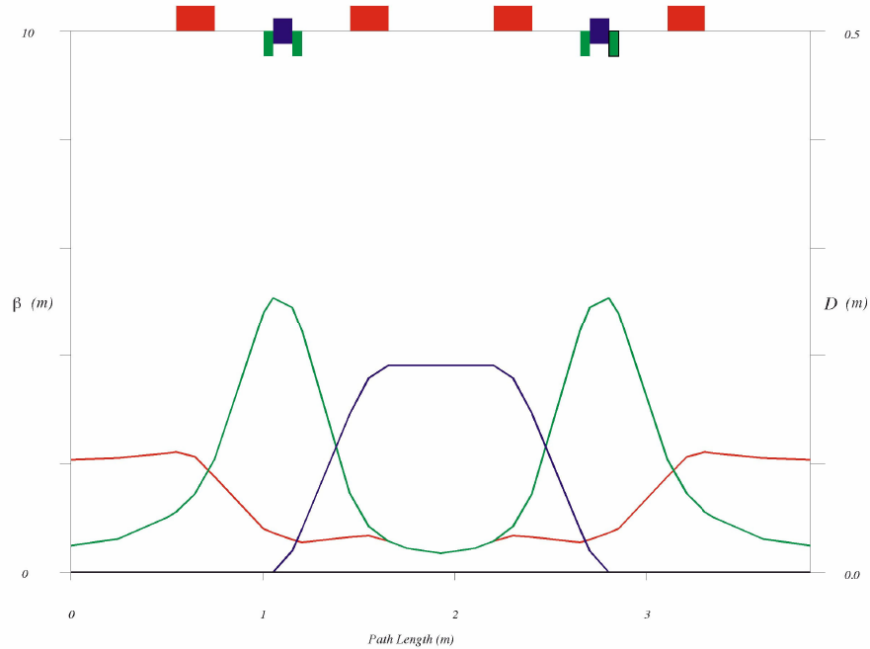
Figure 3.5. Garren lattice [57] showing the Chasman -Green principle. The beam is dispersed (purple line) according to momentum in the center to allow emittance exchange using a lithium hydride wedge. Longitudinal cooling is obtained at the cost of slowing transverse ionization cooling.

3.7 Septa

An alternative to total beam extraction from a ring using strong magnetic kickers is a septa system to slice the beam and extract just a portion of it at a time. A septa is a series of thin electrically charged wires (septum) [10]. Such a system was used at the Fermilab Tevatron for extraction. Fig. 3.6 shows an electrostatic septa diagram.

A septa system uses the electric repulsion between the charged beam and the septum. It slices the beam quickly and efficiently. After the electrostatic septum, a magnetic septum is used to separate the beam further. A system like this has been proposed for use in a future proton-antiproton collider [59–61], in order to increase anti-proton momentum acceptance from ±2% to ±24%.

27
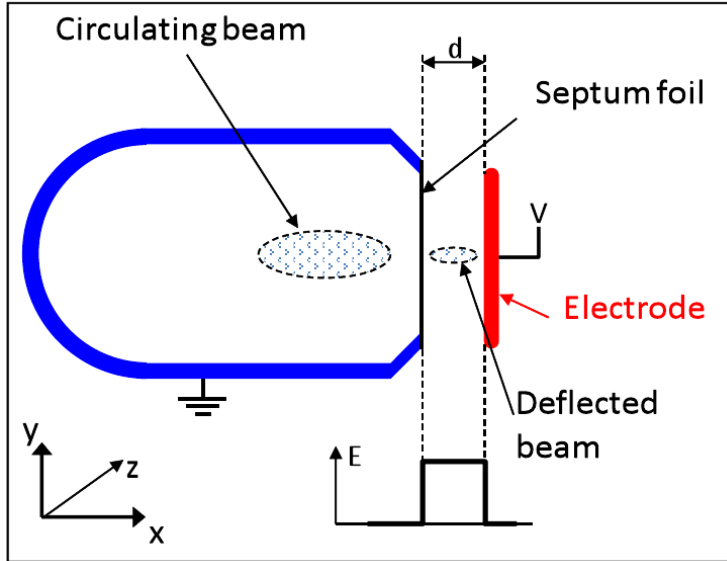
Figure 3.6. Diagram for an electrostatic septa system [58].

3.8   Software Tools

The analytical work produces the general framework, but it is always necessary to make approximations and exclude some variables. That is why it is necessary to run simulation that numerically include more effects and verify the calculations. The software tools used in our investigations are described below.

3.8.1   MAD-X

MAD-X (Methodical Accelerator Design [62]) is a general purpose beam optics and lattice program distributed and supported by CERN. It have been used for more than 20 years to design beam lines and accelerators. In fact, the MAD scripting language is the standard used to describe particle accelerators. MAD-X can to simulate beam dynamics and optimize beam optics for system with thousands of elements The scripting language is similar to C++ syntax and it supports functions and loops.

The basic bend element in MAD-X are sector and rectangular bending magnets. The required parameters are the bending angle θ and the magnet length ℓ. The bending radius is $\rho = \ell/\theta$ [62]. With these values a magnetic field is calculated as:

$$B_y = \frac{1}{e}\frac{pc}{\rho} \tag{3.42}$$

For quadrupoles and sextupoles elements, the main parameters are the length ℓ and the normalized magnetic strength defined as [63]:

$$K_1 = \frac{1}{\beta\rho}\frac{\partial B_y}{\partial x} \tag{3.43}$$

$$K_2 = \frac{1}{\beta\rho}\frac{\partial^2 B_y}{\partial x^2} \tag{3.44}$$

where K_1 is related to the quadrupole focus as:

$$K_1 = \frac{1}{\ell f} \tag{3.45}$$

with f as the quadrupole focal length. The units in MAD-X are given in Table 3.1.

3.8.2 G4Beamline

G4Beamline provides a simple simulation program for the tracking of particles through accelerator systems and through matter. G4Beamline is Java-Geant4 based. It has a graph-

Table 3.1. MAD-X Physical Units

Name	Unit
Length	m (meters)
Angle	rad (radians)
Quadrupole coefficient	m^{-2}
Sextupole coefficient	m^{-3}
Electric voltage	MV (Megavolts)
Frequency	MHz (Megahertz)
Phase angles	2π
Particle energy	GeV
Particle mass	GeV/c^2
Particle momentum	GeV/c

ical environment to plot configurations [65].

3.8.3 ICOOL

ICOOL (Ionization Cooling [66, 67]) operates on similar principles to G4Beamline, also offering a relatively user friendly interface for particle tracking through an arbitrary accelerator system and through material. ICOOL is based on a modified version of GEANT3 [68]. The software comes with a built-in beam analysis tool, ECALC9 [69], which calculates several beam parameters of interest such as emittance. ICOOL has been used for software simulation for several years and is well tested.

CHAPTER 4

MUON IONIZATION COOLING

There are several ways to produce muons that can be used as a beam. The most common method is to collide heavy charged particles with a fixed target. The beam particles can interact with the atomic nuclei in the fixed target. If the collision energy is large enough, the interaction will produce several particles with different charges and masses mostly moving forward from the collision point.

If it is desired to produce a beam of particles, a magnetic field from a lithium lens or a tapered solenoid may be applied to reduce transverse momentum at the expense of the transverse size of the beam. A lithium lens works as an optical lens with a focus at the collision point, so the particles that diverge from the collision point are deflected by the internal field to form a parallel beam. The lithium lens current determines the momentum of the particles that are captured. Then, bending magnets can separate particles by momentum and charge.

For a muon collider, the collected particles are pions that decay into muons. Every decay is random. Decays produce muons and neutrinos with transverse and longitudinal momentum distributions. After drifting a correlation builds up between the muon energy and position. Then a series of radio frequency cavities can be used to make muons move almost at the same velocity. The beam is now easier to handle, but the muons are still moving at a relativity high temperature respect to each other.

Cooling is a challenging task for any high energy collider that uses antiparticles. There are several methods to reduce the temperature or emittance of a particle bunch to the level needed to insure enough collisions in a collider ring. Many of them combine several

methods to prepare the beam before it is injected into a ring. A comparison of the most used methods are shown in Table 4.1.

Table 4.1. Cooling techniques [10]

Cooling Technique	Stochastic	Electron	Synchrotron radiation	Laser	Ionization
Species	ions, $\bar{p}$	ions, $\bar{p}$	e^+e^-	ions	muons
Favored Velocity	high	$0.01 < \beta < 0.1$	$\gamma > 100$	Any	$\gamma < 5$
Beam Intensity	low	any	any	any	any
Cooling Time	$\sim N \cdot 10^{-8}\,\mathrm{s}$	$\sim 10^{-2}\,\mathrm{s}$	$\sim 10^{-3}\,\mathrm{s}$	$\sim 10^{-4}\,\mathrm{s}$	$\sim 10^{-7}\,\mathrm{s}$
Favored Temperature	high	low	any	low	high

Muon emittance has to be reduced quickly because of the muon lifetime, and according to table 4.1 ionization cooling is the fastest method. Ionization cooling is basically electron cooling. The beam transfers part of its energy into the cold electrons of the absorber material. It does not depend on the number of particles in the beam, because the number of electrons is large. The nuclei do cause some multiple scattering.

Some work has been done to try make electron cooling [70–72] fast enough to cool muons [73].

4.1 Ionization Cooling Principle

When heavy charged particles pass through a low Z material, they lose energy by several processes, including ionization, atomic excitation, and bremstrahlung. Fig. 4.1 shows the effect of different processes. The equation that describes the amount of muon energy loss for momentum between 10 MeV/c to 100 GeV/c is given by Bethe and Bloch, eqn. 4.1.

$$-\frac{dE}{dx} = 4\pi N_A \, \rho \, r_e^2 \, m_e \, c^2 \frac{Z}{A} \left[\frac{1}{\beta^2} \ln(\frac{2 \, m_e \, c^2 \beta^2 \, \gamma^2}{I(z)}) - 1 \right] \tag{4.1}$$

32
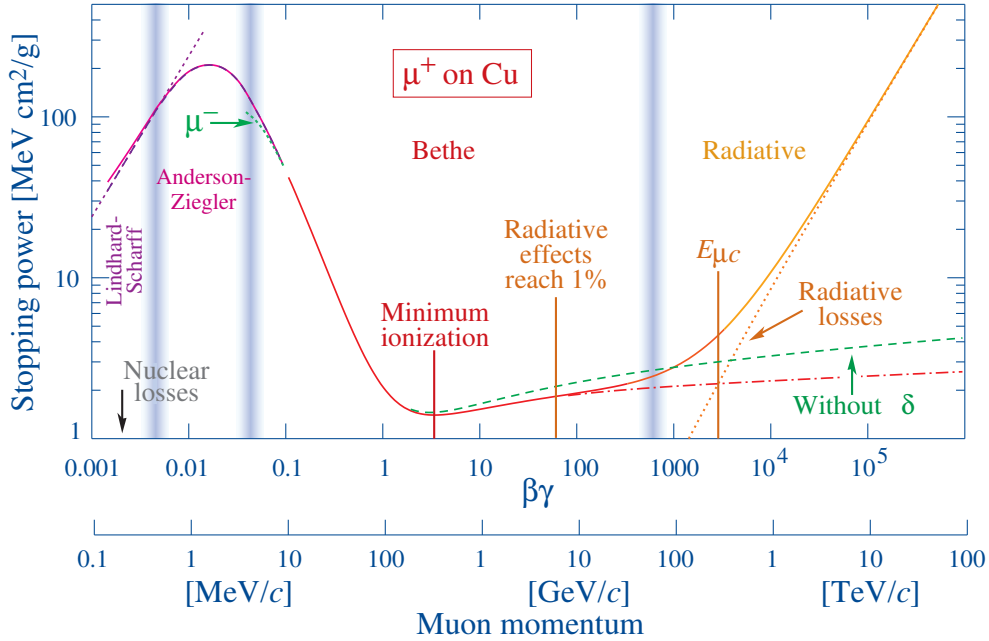
Figure 4.1. Stopping power (energy lost per unit distance) for positive muons in copper as a function of muon momentum [74].

where N_A is Avogadro's number, r_e is the classical electron radius, m_e is the electron mass, β, γ are the Lorentz relativistic factors, and $I(Z)$ is the mean ionization energy. Fig. 4.2 shows the energy lost for particles crossing different density materials. The amount of energy lost increases quickly with density. Only dense absorbers will fit in short low beta regions. For faster cooling, solid material is required. But denser materials do have more multiple scattering than hydrogen.

4.2   The Cooling Formula

Ionization cooling uses the energy loss process to reduce the momentum of beam particles. Each particle loses transverse and longitudinal momentum as Fig. 4.3 shows.

After the beam passes through material, RF cavities restore just the longitudinal momentum. So, after several steps the particles in the beam have a lower transverse momentum spread. The rate at which particles lose energy is given by the Bethe-Bloch formula, eqn. 4.1. Emittance evolution is described by eqn. 4.2 for transverse cooling and eqn. 4.3

33
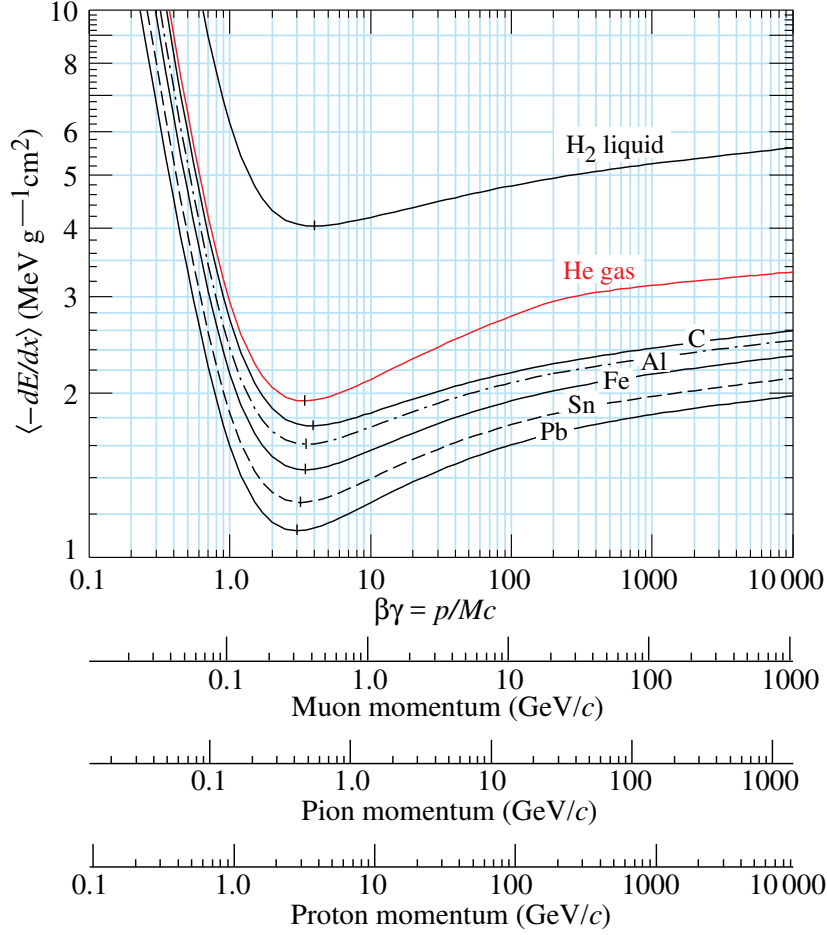
Figure 4.2. Mean energy loss as a function of momentum for muons, pions, and protons crossing different materials [74].

for longitudinal cooling [75, 76].

$$\frac{d\epsilon_\perp}{ds} = -\frac{g_t}{\beta^2}\frac{dE_\mu}{ds}\frac{\epsilon_\perp}{E_\mu} + \frac{1}{\beta^3}\frac{\beta_\perp^*}{2}\frac{(13.6\,\mathrm{MeV})^2}{E_\mu m_\mu c^2 L_R} \tag{4.2}$$

$$\frac{d\epsilon_L}{ds} = \frac{-g_L}{\beta^2 E_\mu}\frac{dE_\mu}{ds}\epsilon_L + \frac{\gamma^3\beta_L}{\beta c^2 p^2}\pi(r_e m_e c^2)^2 n_e(2-\beta^2) \tag{4.3}$$

where dE_μ/ds is the energy lost as calculated by the Bethe-Bloch equation, $\beta_\perp^*$ and β_L are transverse and longitudinal betatron functions, and g_L and g_t are partition numbers that depend on the absorber geometry. Eqns. 4.2 and 4.3 each have two terms. The first term
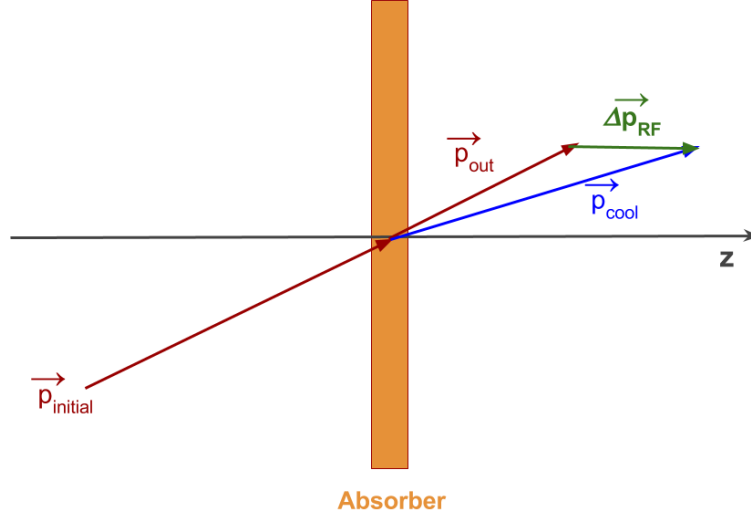
Figure 4.3. Ionization cooling principle. Momentum $p_{initial}$ is reduced transversely and longitudinally, then RF cavities restore the longitudinal momentum lost Δp_{RF}. The final momentum is $p_{final} = p_{out} + \Delta p_{RF}$.

describes the cooling due to momentum loss and the second term describes the heating due to multiple scattering and straggling. When both terms are equal the emittance is in equilibrium. The transverse and longitudinal equilibrium emittances are given in eqns. 4.4 and 4.5:

$$\epsilon_{\perp,eq} \simeq \frac{\beta_{\perp}^{*}(13.6 MeV)^2}{2g_t \beta m_\mu c^2 L_R (dE/ds)} \tag{4.4}$$

$$\epsilon_{L,eq} \simeq \frac{\beta_L m_e c^2 \beta \gamma^2 (2-\beta^2)}{4g_L m_\mu c^2 \left[\ln\left[\frac{2m_e c^2 \gamma^2 \beta^2}{I(Z)}\right] - \beta^2\right]} \tag{4.5}$$

The transverse betatron function at the absorber should be small in order to keep the equilibrium emittance low and to reduce the heating due to multiple scattering. The expression for $< \beta_\perp >$ is given by eqn. 3.29. Strong focusing is required to cool the beam. The terms g_t and g_L are called the transverse and longitudinal partition numbers. Those

terms couple emittance exchange which will be explained in Section 4.2.1. When the muon momentum is below minimum ionizing, the energy loss curve rises. This leads to longitudinal heating unless the absorber shape and partition numbers are used to lower the longitudinal emittance at the expense of the transverse emittance. Not too far above the minimum ionization momentum, straggling becomes a problem. In any case the fractional cooling is proportional to the fractional energy loss. This favors low energy cooling because less RF is needed to replace lost energy.

To have a lower longitudinal equilibrium emittance, it is important to have a low longitudinal betatron function, eqn. 4.6. The variables to get a low longitudinal betatron function are the RF wavelength λ_{RF}, the RF gradient and the RF phase angle ϕ_s. These numbers are not completely free and depend on the lattice optimization given by MAD-X and G4beamline simulations.

$$\beta_L = \sqrt{\frac{\lambda_{RF} \beta^3 \gamma m_\mu c^2 \alpha_p}{2\pi e < V' > \cos(\phi_s)}} \tag{4.6}$$

Emittance evolution is estimated using the cooling characteristic eqn. 4.7, where i = x, y, s [76], and s is the longitudinal dimension.

$$\epsilon_i(s) = (\epsilon_{0,i} - \epsilon_{i,equi}) \exp(-s\frac{g_i(dP_\mu/ds)}{P_\mu}) + \epsilon_{i,equi} \tag{4.7}$$

4.2.1 Longitudinal Cooling and Emittance Exchange

For straight magnetic lattices, the longitudinal and transverse emittances are independent. But, if a bending element creates dispersion, they can become coupled. Dispersion makes off momentum particles follow different trajectories, higher momentum particles travel a different distance as compared to lower momentum particles. Emittance can be exchanged if a wedge absorber is placed in a dispersive region. The wedge has to be placed to make high momentum particles travel through more absorber material and low momentum particles travel through less absorber material. Momentum spread is reduced at cost of increasing
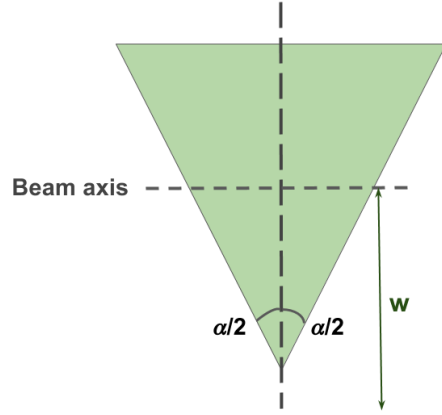
Figure 4.4. Wedge geometry for emittance exchange.

the transverse emittance. The absorber geometry is represented in Fig. 4.4.

The geometry of the wedge defines how the longitudinal and transverse emittances are coupled. The amount of emittance exchange is given by the partition factors g_x, g_y, and g_L. For a dispersion only in the X dimension the partition factors are defined by equations 4.8, 4.9, and 4.10.

$$g_x = 1 - \Delta g \tag{4.8}$$

$$g_y = 1 \tag{4.9}$$

$$g_L = g_{L,0} + \Delta g \tag{4.10}$$

The term Δg is defined as :

$$\Delta g = \eta \frac{\rho'}{\rho_0} \tag{4.11}$$

where η in equation 4.12 is the dispersion function magnitude, $\delta = \frac{\Delta p}{p}$, and ρ'/ρ_0 is the density wedge variation. Usually the wedge density is constant, so the amount of material that a muon goes through is just proportional to W, the distance from the muon to the wedge apex. The relation is shown in eqn. 4.13.

$$\eta = \frac{dx}{\delta} \tag{4.12}$$

$$\frac{\rho'}{\rho_0} = \frac{\eta}{W} \tan\left(\frac{\alpha}{2}\right) \tag{4.13}$$

The term $g_{L,0}$ depends on the particle momentum and the material minimum ionization energy as eqn. 4.14 shows.

$$g_{L,0} = -\frac{2}{\gamma^2} + 2\frac{1 - (\beta/\gamma)^2}{\ln\left(\frac{2m_e c^2 \gamma^2 \beta^2}{I(Z)}\right) - \beta^2} \tag{4.14}$$

The goal for effective cooling is to exchange enough longitudinal emittance to one of the transverse dimensions. It does slow the transverse cooling. The momentum at which cooling is performed affects the partition factors. Fig. 4.5 shows how the factor $g_{L,0}$ varies with the beam momentum. In many cases one is approaching the transverse emittance equilibrium value, and it can be very advantageous to store cooling in the longitudinal dimension via emittance exchange.
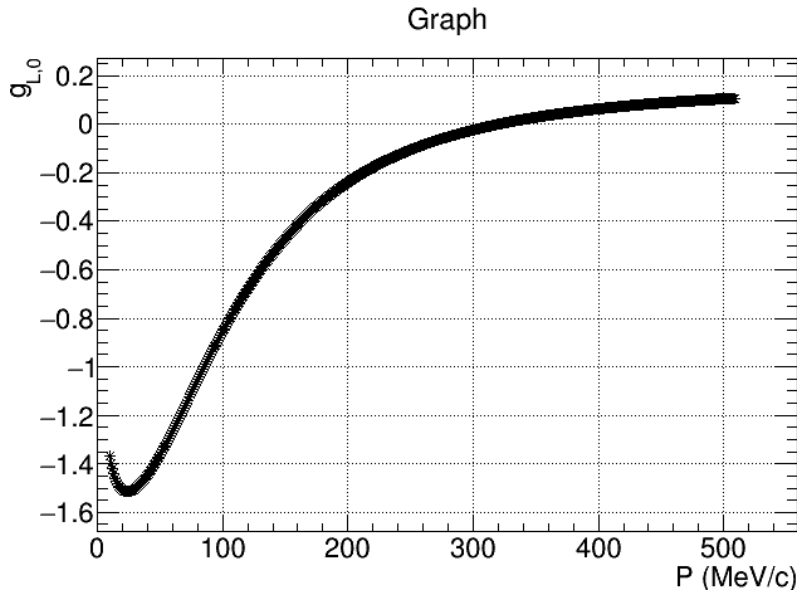
Figure 4.5. Longitudinal partition number $g_{0,L}$ plotted versus muon momentum [76].

Table 4.2. Material properties. Values of density, Z/A, L_R, and ionization energy are from [74]. The value of δE is calculated from eqn. 4.1 and $g_{L,0}$ uses eqn. 4.14.

Material	Density g/cm^3	Z/A	L_R cm	I(Z) eV	δE MeV/cm	g_{L_0} $\times 10^{-2}$
LiH	0.820	0.5032	97.09	36.5	1.6222	2.6483
Be	1.848	0.45	35.28	63.7	3.0745	3.4142
B$_4$C	2.520	0.4706	19.90	84.7	4.3343	3.8357
Diamond	3.520	0.5	12.13	78.0	6.4744	3.7116

4.3 ICOOL Cooling Libraries and Tools

To perform the cooling simulation the selected code is ICOOL [66]. It is used as the simulation code for the Rectilinear Channel in Section 2.2.1. The ICOOL tools are described in [69]. Gregg Penn's program ECALC9 is the standard emittance calculator for the Muon collaboration. The scripts used to calculate the emittance evolution (eigemit.for) on this work are all based on the ECALC9 script and included together with the ICOOL simulation software folder. The code reads the tracking information variables x, y, t, p_x, p_y, E and calculate the 6D covariance matrix as,

$$M_{i,j} = <q_i q_j> - <q_i><q_j> \tag{4.15}$$

where q_i is the independent phase space variable. A statistical weigh w_i is assigned to reduce the particle distribution tails.

$$<q> = \frac{\Sigma_{i=1}^N q_i w_i}{\Sigma_{i=1}^N w_i} \tag{4.16}$$

Thus, the emittance is calculated using m for the muon mass and equation 4.17,

$$\epsilon_{6N} = \frac{c}{m^3}\sqrt{det(M)} \tag{4.17}$$

for the transverse coordinates x, y,

$$\epsilon_{TN} = \frac{c}{m}\sqrt{det(M_T)} \tag{4.18}$$

39

If there is correlation between the transverse and longitudinal emittance, the longitudinal emittance is calculated by equation 4.19. If there are not correlation, the term $M_{3,3}^L$ is set to one.

$$\epsilon_{LN} = \frac{c}{m} \frac{\sqrt{(M_L)}}{M_{3,3}^L} \tag{4.19}$$

4.3.1 Geant3/Geant4

Geant3 and Geant4 are the toolkit for the simulation of the passage of particles through matter. They are widely used to estimate particle energy losses. The beam line software G4beamline simulates all of the energy loss events through absorber materials using Geant4 libraries. ICOOL used a previous Geant3 version. Geant3 and Geant4 cover all relevant physics processes: electromagnetic, hadronic, decay, optical, for long and short lived particles [64]. A complete guide of the physics models used by Geant4 can be found in [77] and [78].

4.3.2 ICOOL Scattering Model

ICOOL simulates the scattering heating process using the Fano model with a Rutherford limit [79]. A comparison of the ICOOL scattering models are presented in the Fernow paper [80]. Several models can be used to approximate the scattering and heating corresponding to the second term of equation 4.2. The Fano model is a correction of the Bethe model that describes heavy particles like muons being scattered by low Z materials. A discussion to the origin of the PDG scattering approximation can be found in Tim Carlisle's thesis [81].

The are three stochastic process that can be activated or deactivated individually in ICOOL that affect how the muons interact with the material. Also, muon decays affect the transmission and affect quality factors, like the Merit factor eqn. 6.1, that give the effectiveness of the cooling. The commands that control the ICOOL stochastic processes are:

- lscatter: Multiple scattering that heats the beam and increases the angular phase space of the beam.

- lstrag: Straggling present due to the natural energy fluctuations that occur during the ionization process. Each simulation software have different models to calculate the energy straggling effect. ICOOL used the Vavilov model [79].

- ldray: Delta rays are fast electrons having the energy to produce a second ionization due a frontal muon collision. A high energy delta ray takes considerable energy from a muon, drastically reducing the muon energy.

- ldecay: Decays are the natural muon behavior and they do not directly affect cooling. The decay has to be considered because the beam cooling has to be done fast enough to avoid beam losses, which lowers transmission.

CHAPTER 5

CELL DESIGN AND SIMULATION

In this chapter we begin the cell design and present simulation results. The cooling cell is designed in order to match the muon collider cooling requirements described in Section 2.2.1. The main parameter is to have a lower transverse equilibrium emittance in the absorber region than the Rectilinear Channel which cooled to 280 μm. Eqn. 4.2 shows that a lower betatron function $\beta_\perp$ is needed to reduce the equilibrium emittance at the absorber. The minimum betatron function that the Rectilinear Channel can archive is 3 cm using magnetic fields up to 16 T as Fig. 2.5 shows. Thus, the equilibrium emittance has to be lower than the final emittance achieved for the Rectilinear Channel final stage. Also, the momentum band has to be wide enough ($\approx 10\%$) to transport longitudinal emittance of 1.537 mm that corresponds to the final longitudinal emittance achieved by the final Rectilinear Channel stage.

The second important requirement is to have dispersion in the absorber region. Dispersion allows a wedge-shaped absorber that makes the emittance exchange described in Section 4.2.1 possible. According to Section 3.4.2 the betatron function at the absorber has a quadratic behavior. So, the average betatron can be calculated using the twiss parameters at the end of the last (Q2) quadrupole using equation 3.29. The goal is a quadrupole cell with a low minimum betatron function that will transport the required beam emittance.

5.1 Matrix Approximation

Using the matrix formalism described in Section 3.3, the magnetic gradients can be initially set to get the required values for the minimum betatron function. An initial approach is made taking a focusing quadrupole triplet system described in Section 3.4. Due
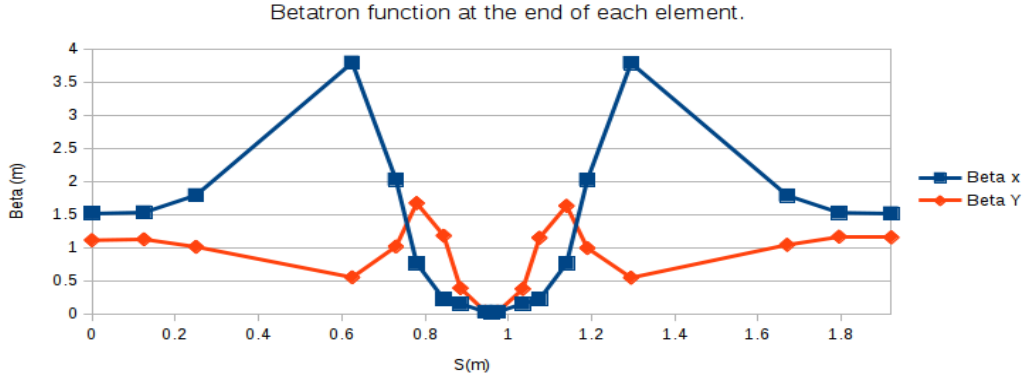
Figure 5.1. Full cell betatron function vs. distance s using matrix multiplication. The Courant-Snyder [52] parameter evolution through the cell is given by MAD-X.

to the relatively long space that the cell should have for RF cavities, a coupling quadrupole is added. The cell has enough space for eight RF cavities to replace the energy lost in the absorbers. Fig. 5.1 shows the betatron function evolution though the cell using matrix multiplication, where the values are calculated at the end of every element or drift space.

The matrix multiplication, using the hard edge model for magnetic quadrupoles (eqns. 3.22 and 3.23) and 3.27 for the drift space, produces a transfer matrix that combines trigonometric and hyperbolic functions making the algebraic procedure difficult. To simplify the process a software package such octave or root is used to sketch the betatron functions verifying the minimum and maximum values are acceptable for practical purposes. Also, getting the matrix is useful to study stability conditions and other variables.The method described has several limitations. The transfer matrix that calculates effects like focusing or dispersion needs to be a full 6D matrix that is difficult to manipulate due to its size. So, it is used only as a first approximation to the cell parameters. To get more accurate values and control more variables a more specific dedicated software package needs to be used.

5.2   MAD-X Simulation

MAD-X, described previously in Section 3.8.1, has several modules to minimize the variable set needed to find an optimal solution for a cell configuration. The magnetic gradient

values gotten by matrix multiplication are used as initial input. The MAD-X configuration file needs a set of values close enough to the right values to produce a successful minimization. There are several minimization methods that can be set in MAD-X. The set of cell constraints imposed on the matching module are shown in Table 5.1. The values for $\beta_{\perp}^*$ are set low to minimize the equilibrium emittance at the absorber. The dispersion η is used for emittance exchange. The variables $\mu_{x,y}$ are the betatron phase advances that keep the central momentum particle far away from the phase stop bands at π and 2π that lead to unstable transmission. Finally, $\partial \mu_{x,y}/\partial \delta$ is the transverse de-tune parameter, which gives off momentum particles a small phase advance variation with respect to the reference particle. All imposed constraints are essential to control the transmission requirements and the stable momentum band.

The MAD-X betatron function evolution for the full cell is shown in Fig. 5.2. It shows a good agreement with the matrix approximation plotted in Fig. 5.1. The dispersion function is included and all the constraints are fulfilled. The transported beam has $\beta_{x,max} \cong 2\beta_{y,max}$.

The bore diameter and length for the first quadrupole magnet Q0 is 12.5 cm. The Q0 magnet works as a coupling quadrupole reducing the betatron function maximum and allows the addition of more RF cavities to increase longitudinal synchrotron focusing. The bore diameter and length of the quadrupoles are optimized to reduce the magnetic field. A long central quadrupole Q3 with 3 cm bore radius is added to reduce both the chromaticity and the minimum beta function. The 1.92 m long full cell has a central 3 cm drift space for

Table 5.1. MAD-X constraints for the cooling cell.

Variable	Value	Unit
β_x^*	2.2	cm
β_y^*	2.7	cm
η	4.1	mm
μ_x	0.7	$\times 2\pi$
μ_y	0.68	$\times 2\pi$
$\partial \mu_x/\partial \delta$	2.6	
$\partial \mu_y/\partial \delta$	2.6	
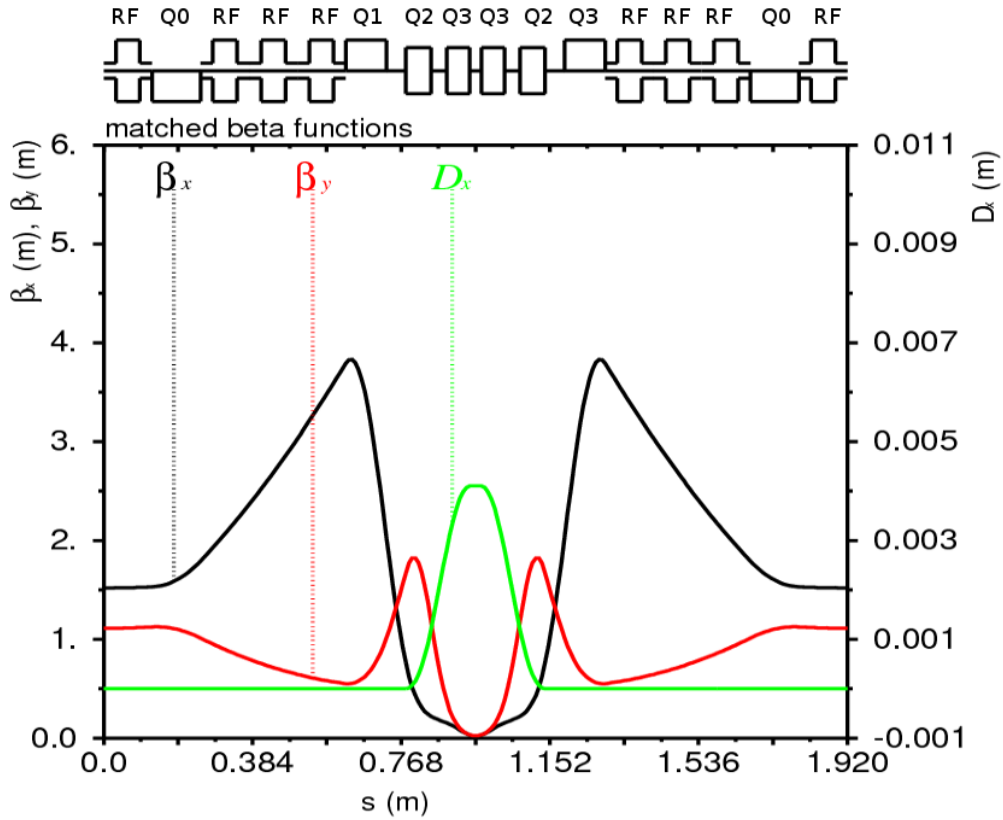
Figure 5.2. Full cell betatron function vs. distance s. The Courant-Snyder [52] parameter evolution through the cell is given by MAD-X.

a wedge absorber in addition to the pair of central quadrupole triplets and the two coupling quadrupoles.

The dispersion function, plotted as the green line in Fig. 5.2, is designed to have a Chasman-Green lattice like behavior as described in Section 3.6. The magnet labeled as Q2 is a combined function magnet that has a dipole moment combined with a quadrupole magnetic field. The Q3 magnet also has a dipole moment. This makes the dispersion constant in the absorber region, The dipole magnetic strength is calibrated to couple to the quadrupole gradient to complete the Chasman-Green configuration [57, 82, 83].

Table 5.3 summarizes the MAD-X simulation output. Some variables are calculated. Parameters to constrain the phase advances are for a 1.92 m long full cell. Dispersion is

Table 5.2. Cell element dimensions and parameter values.

name	L (mm)	R (mm)	RF frequency (MHz)	RF Gradient (MV/m)	ϕ_s (deg)
RF1	125(*1)	100	650	27.87	11.5
RF2	125(*3)	100	650	27.87	11.5
			Magnetic gradient (T/m)	Magnetic Dipole field (T)	
Q0	125	100	-12.23	0	
Q1	105	50	90.04	0	
Q2	65	30	-274.95	± 0.687	
Q3	60	33	337.33	± 0.335	
			Material		
Drift 1	50	100			
Drift 2	40	100			
Absorber	30	30	Lithium Hydride		

flat and constant at the absorber place and zero at the cell ends. The average transverse betatron functions over the 3 cm long absorber regions is less than 3 cm for a 400 MeV/c muon as noted in Table 6.1.

Table 5.3. Main constants used in the calculations

Variable	Value	Unit
p	400	MeV/c
β	0.967	
γ	3.914	
$\beta^*_{x,y}$	(2.2,2.7)	cm
α_p	7.0654×10^{-4}	
$1/\gamma^2$	0.065	
Total L	1.92	m
ALFA	0.0046	
GAMMATR	14.70	
Q1	0.68	
Q2	0.70	
DQ1	-2.547924351	
DQ2	-2.841194469	
DXMAX	41	mm

This design provides strong focusing using magnetic pole tip fields of Q0 = 0.75 T, Q1 = 4.69 T, Q2 = 9.02 T, and Q3 = 11.40 T. Quadrupoles with peak fields of more than

46

12 T have been built with Nb_3Sn [84, 85].

5.3   G4beamline RF Setup

G4beamline offers a tool set to calibrate the RF cavities and test the muon behavior making the simulation more realistic and helping to evaluate the effects of fringe fields as was described in Section 3.8.2.

Fig. 5.3 is the graphical representation for two consecutive cells. The red cylinders represent the RF cavities. Purple, green, yellow, and dark blue are the respective quadrupoles QC, Q1, Q2, and Q3. The 3 cm long Lithium Hydride absorber is between the Q3 quadrupole pairs in the center of each cell. G4beamline automatically sets the RF cavities to restore the reference particle initial momentum at the end of the two consecutive cells. According to the G4Beamline manual [65], "The phase of an RF cavity (pillbox) is determined by its *timeOffset* and *timeIncrement* arguments. If *timeOffset* is not specified it is automatically set to *phaseAcc* by the Tune particle." The full simulation is not performed under G4BeamLine, thus no dispersion is implemented.
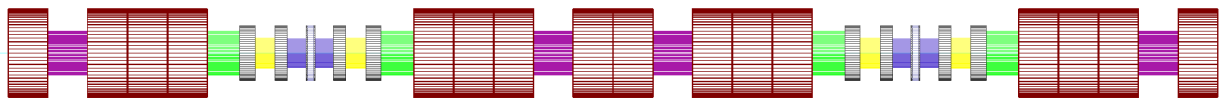
Figure 5.3. G4beamline Cell Configuration.

5.4   ICOOL Simulation

The main simulation is performed in ICOOL for several reasons, even though ICOOL does not have a graphical interface like G4beamline. The simulated particle tracks are stored in the output file *for009.dat*. The most common option to read the information is to use the historoot software. For this work the root code was implemented to plot the

47

particle trajectories together with a series of rectangles representing the cell elements as is shown in Fig. 5.4. Red rectangles represent the RF cavities, green rectangles are de-focusing quadrupoles in the X dimension, and yellow rectangles are focusing quadrupoles. The black triangle represents the wedge absorber. The muon trajectories are represented as blue points.
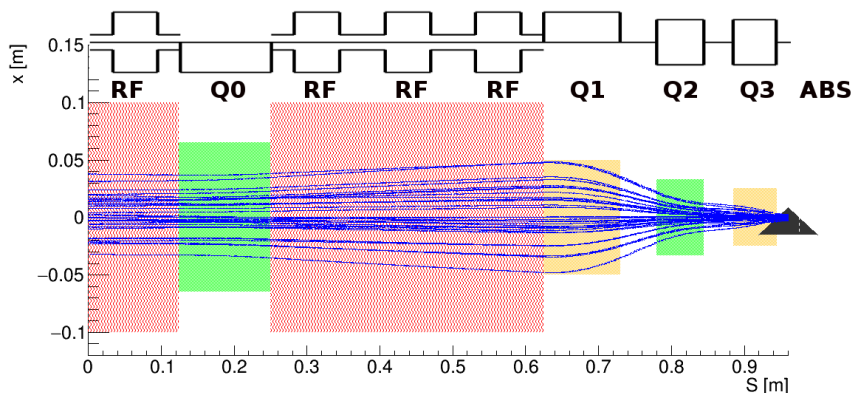
Figure 5.4. Half cell dimensions. Four identical RF cavities occupy a total of 50 cm giving a half cell length of 96 cm.

The ICOOL simulation for 2500 muons through 2 full cells is shown in Fig. 5.5 and Fig. 5.6. The beam trajectories agree with the MAD-X betatron plots in Fig. 5.2. The beam focus is at the absorber position. The X betatron function has maximum at the Q1 quadrupole and the Y maximum betatron function is at the Q2 quadrupole. Thus, the main sources of scraping are the Q1 and Q2 bores. Off momentum particles tend to be scrapped first because according to Fig. 5.10, the maximum momentum offsets double the betatron amplitudes. Hence the need for more chromatic correction.
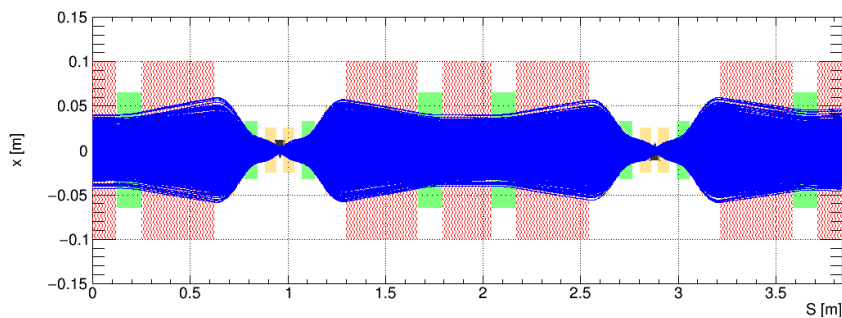
Figure 5.5. ICOOL X view. Wedges are positioned at the centers of the first and second cells.
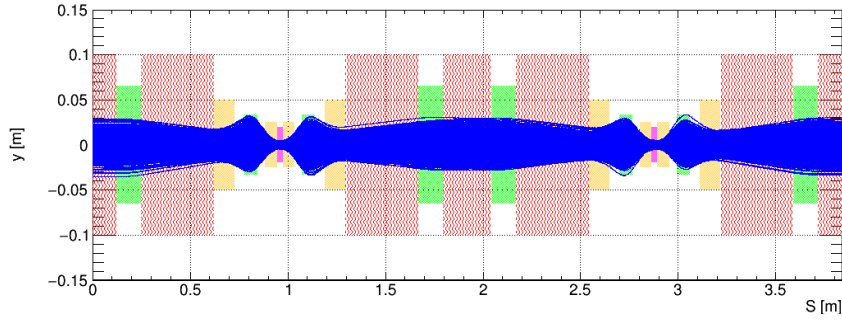
Figure 5.6. ICOOL Y view. Wedges are positioned at the centers of the first and second cells.

5.4.1   ICOOL Dispersion Test

The magnets in this ICOOL run are dipoles which bend the muon tracks. To test the dispersion in ICOOL, 10 muons were sent through the magnetic lattice. The X position for every track is plotted respect to the X coordinate in the Fig. 5.7.
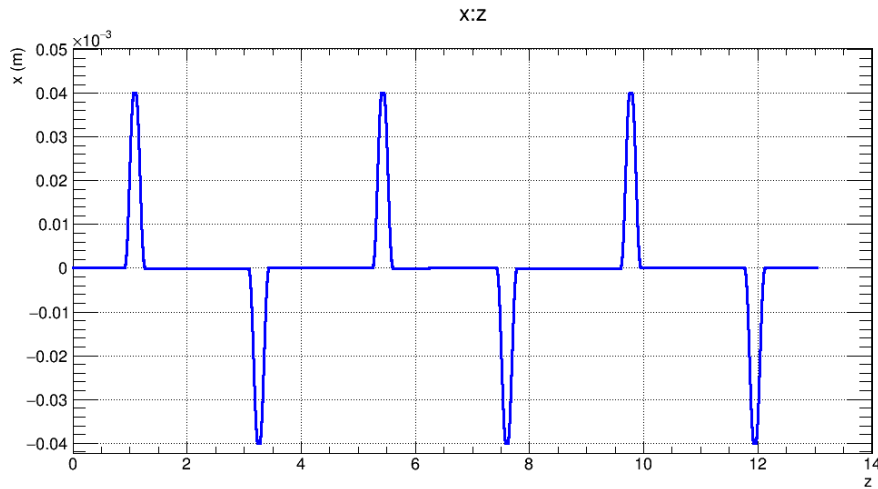
Figure 5.7. x vs s plot for 10 muons sent with an off momentum of p = 404 MeV/c though 6 full cells.

The lattice is designed to make the first cell bend to create dispersion in the positive X dimension, then the second cell bends backwards in order to create a snake and a net bend of zero degrees. The maximum distance in X from the reference center is consistent with the designed dispersion function as in eqn. 5.1. The dispersion is zero in the RF cavities and flat and constant at the absorber, making it consistent with the MAD-X design.

$$\eta = \frac{\Delta x}{\delta} = 4.1 \, \text{mm} \tag{5.1}$$

The test is made with neither RF cavities nor absorber. The purpose is just test the particle behavior in ICOOL and to test the magnetic lattice translation from MAD-X to ICOOL.

5.4.2 Stable Transmission Momentum Bands

To find the maximum and minimum accepted momentum in the lattice, 1000 muons were transported 1 mm away from the lattice axis. The muon momentum varied from 300 MeV/c to 500 MeV/c. See Fig. 5.8. The test was made for X and Y separately. It is related to the stop bands that the cell has. Off momentum particles have a phase advance different than the reference particle. How close they are to the stop band is determined by the μ_x, μ_y parameters. One wants to make $\partial \mu_{x,y} / \partial \delta$ small. Momentum variations also affect the longitudinal locations of β_x^* and β_y^* as Fig. 5.9 indicates and can shift the minimums outside the absorbers, which deceases cooling.
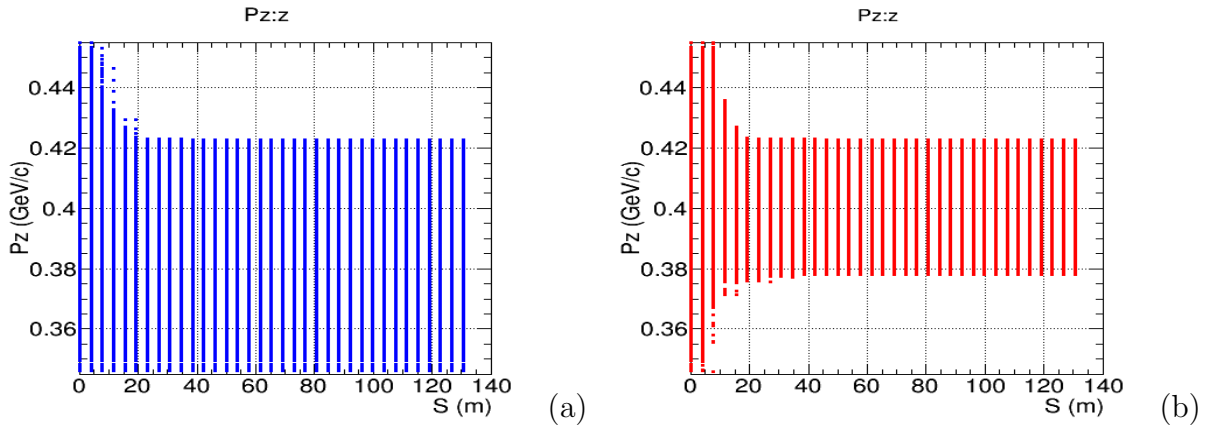
Figure 5.8. Momentum width band for X (a) and Y (b). X shows a stable transmission from p = 350 MeV/c to p = 424 MeV/c. Y shows a stable transmission from p = 378 MeV/c to p = 423 MeV/c

As can be seen in Fig. 5.9, β^* is small only over a limited longitudinal distance, so the absorber must be dense and short [75]. Fig. 5.10 shows more detail of how the betatron functions behaves for off momentum particles. For quadrupole lattice configuration, the
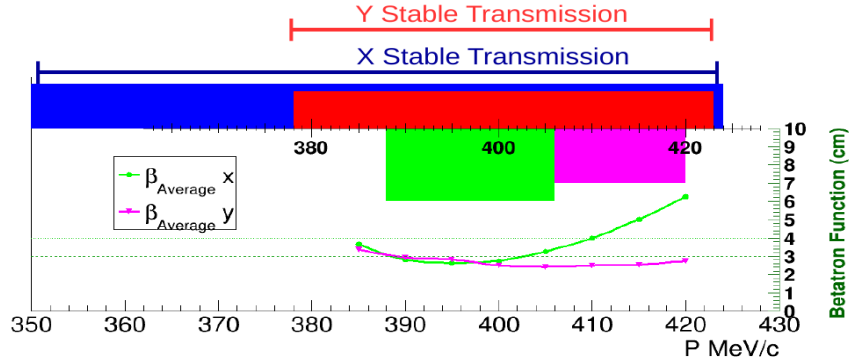
Figure 5.9. The blue bar is the region where the magnetic lattice has stable transmission for X and the red bar shows the stable transmission band for the Y dimension. The green and purple bars indicate that the momentum ranges where $< \beta_x > < 3$ cm and $< \beta_y > < 3$ cm are $350 < p < 424$ MeV/c and $391 < p < 422$ MeV/c, respectively.

absorber is 3 cm long on the reference orbit.
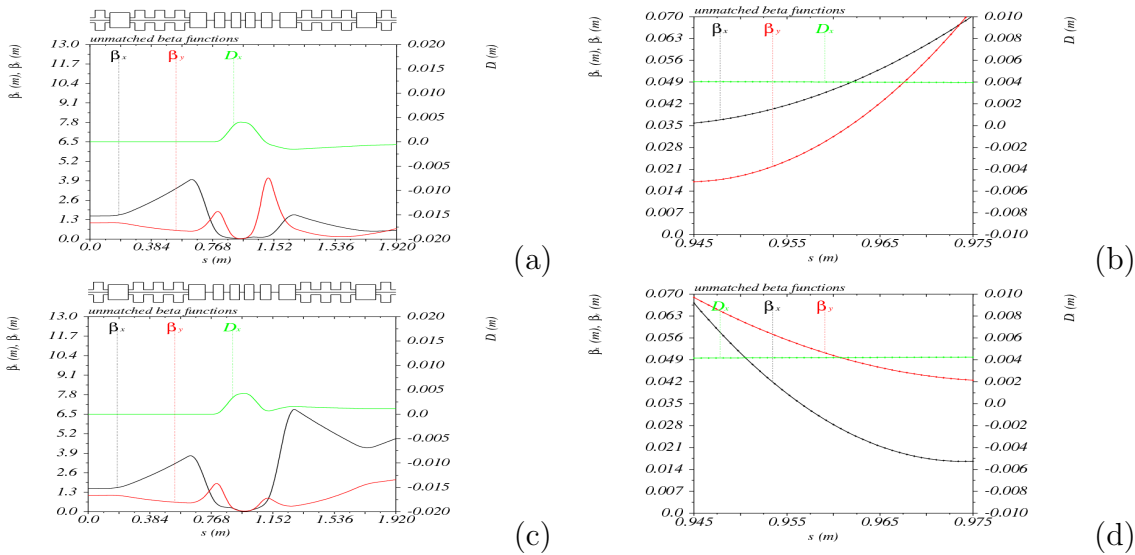
Figure 5.10. MAD-X betatron function for an off momentum particle with p = 420 MeV/c (a), (b) shows the betatron function at the absorber space. (c) and (d) are the betatron function for a particle with p = 380 MeV/c.

5.4.3 Testing Absorber Location

To place the absorber with a wedge shape as described in Section 4.2.1, it is necessary to use the ICOOL command WEDGE. The absorber vertex is located at the center. The base angles go out of the drift space and enter the quadrupoles. To do this extension, additional wedges are placed in the ends of the central quadrupoles. To test the wedge positioning in the cells, the quadrupole gradients are set to zero and stochastic processes are turned off. A uniform distributed muon beam is transported though two cells. Then, the zones in which the muons have lost momentum are plotted. The Fig. 5.11 shows the result of this test. Fig. 5.12 shows the result of muons passing through the wedge with the quadrupoles on.

The cell is designed to focus at the absorber position. Particles with momentum p = 400 MeV/c cross the absorber at the S,X plane. But, due to the dispersion particles for high momentum go through the wide absorber region, particles with lower momentum go through a thin absorber region. Fig. 5.12 shows that the beam waist goes through the absorbers center at the first and second cells. The beam does not exceed the size of the absorber nor does the dispersion affect the beam waist width.
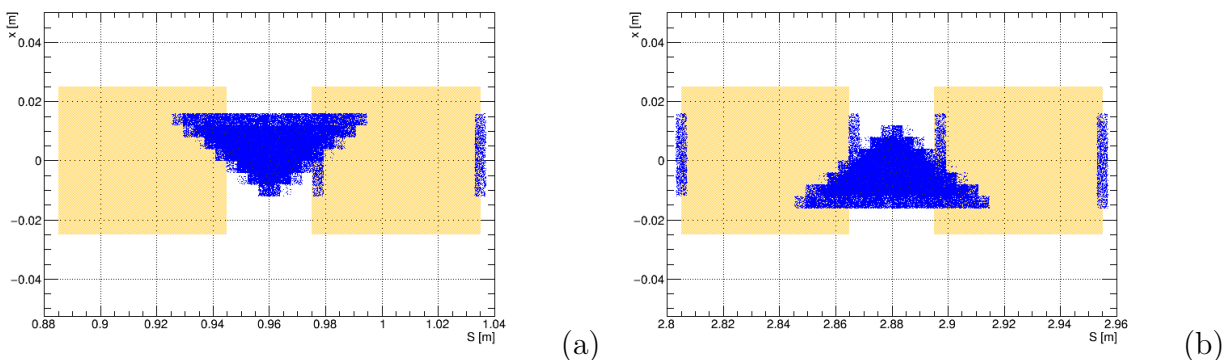
Figure 5.11. Test for the Wedge positions at the centers of the first and second cells. One thousand muons were transported with quadrupoles off. The regions in which the momentum decreases are plotted in blue.
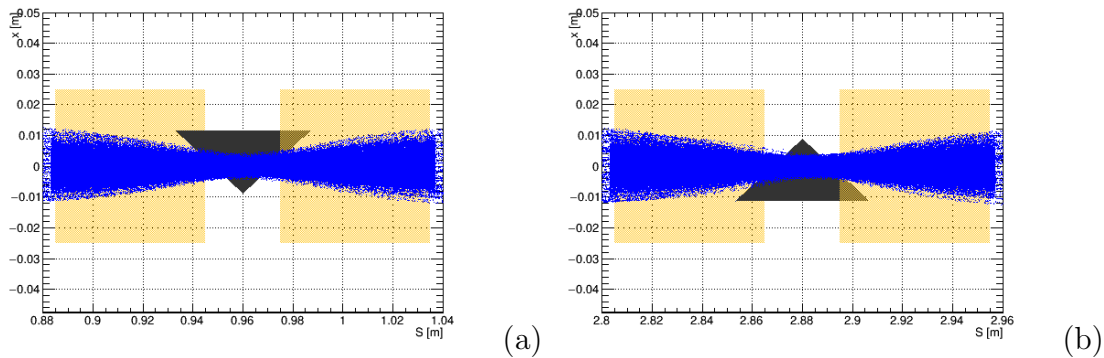
Figure 5.12. Wedge positions at the centers of the first and second cells. The quadrupoles are active to produce focus at the absorber positions.

5.5   ICOOL Setup of Radio Frequency Cavities

The reference particle starts with a momentum of p = 400 MeV/c, but right at the beginning there are RF cavities that increase the momentum over the reference momentum. At the absorber the reference particle loses momentum, and it has to travel though the three following quadrupole magnets before the lost momentum can be replaced by the RF cavities. Fig. 5.13 shows the p_z momentum vs. S position plot for 5 muons going through two cells. The momentum increase in the RF cavities is clear as is the momentum lost in the absorbers. Stochastic processes can affect the muon momentum as well, creating a momentum offset
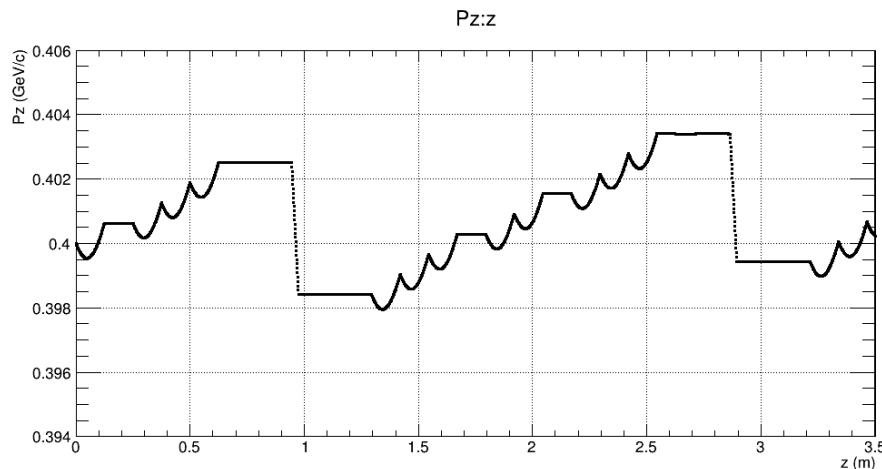
Figure 5.13. Momentum changes through 2 cells due to RF cavities and absorbers.

with respect to the reference particle and an enveloped momentum oscillation that extends

53

through the full channel as is plotted at Fig. 5.14. This oscillation has a Δp amplitude of about 5 MeV/c. Off momentum particles can have larger amplitudes and offsets. This is a main reason to keep the momentum band from Fig. 5.9 as wide as possible.
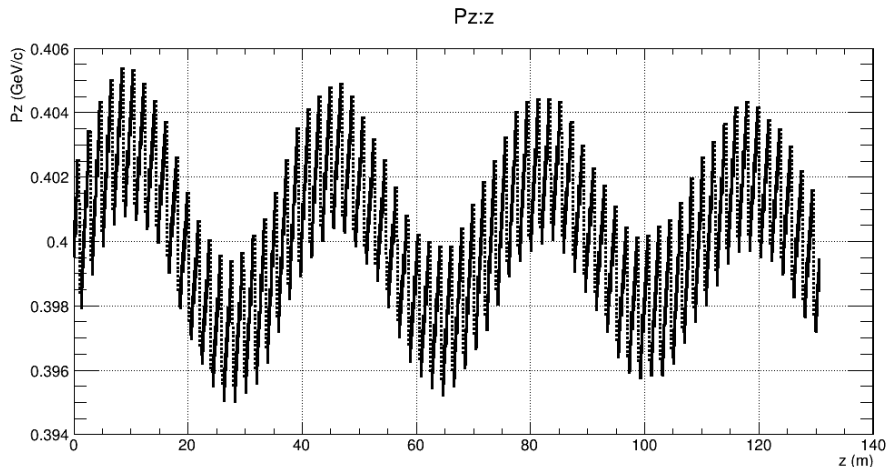
Figure 5.14. Momentum oscillation of one muon in the full channel. All muons do not have the same momentum oscillation.

5.6   Channel Admittance

The admittance as defined in equation 3.17 is tested by sending a beam into the channel with no RF cavities activated and no absorber. An arbitrarily wide beam is transported through the magnetic lattice to test the maximum emittance accepted by the channel. This test is made to feed the cooling simulation to reduce the initial emittance mismatch and reduce the scraping. If the beam is set correctly at the beginning the emittance ellipse area and shape should be constant at the end of every cell. A sample of the px vs x and py vs y distributions is presented in Fig. 5.15. The transverse emittance is $\epsilon_{x,y} = (360, 240)$ mm rad.

When the absorbers and RF are included and the stochastic processes are on except for decays, the transmission drops to 61%. Fig. 6.1 shows transmission vs. distance.
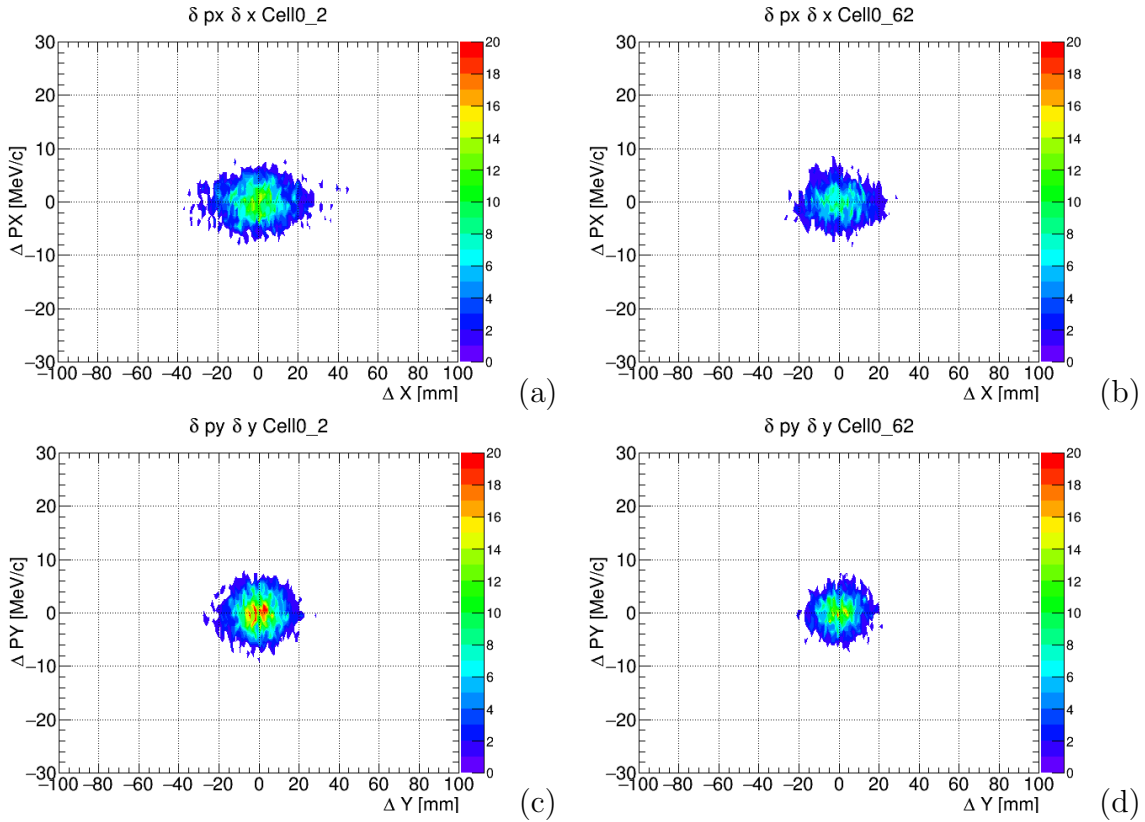
Figure 5.15. 2D histogram filled with Δp_x vs X for 2000 muons at the end of cell 2 (a) and cell 62 (b). Histogram (c) plots py vs Y at the end of cell 2. Plot (d) corresponds to cell 62. The Channel is composed of 68 cells. Here, only 2 sample cells are showed.

CHAPTER 6

COOLING SIMULATION

Cooling simulations were performed using the ICOOL [66] software package. It has the appropriate FORTRAN scripts (EIGEMIT and ECALC9) [69], described in Section 4.3, to calculate the rms emittance at multiple points. Every element in the magnetic lattice is considered as a cylinder. The information u, u' for the generated beam is transported through the cylinder and the final information is stored in a for009.dat file. If the cylinder has absorber material, several physics processes can be activated in order to study how muon tracks are affected by the material interaction, which causes cooling through energy loss but also beam heating.

6.1 Cooling Calculations

The wedge angle to optimize emittance exchange was selected to be $\alpha = 105°$. With it the value of Δg may be calculated as:

$$\Delta g = \frac{4.1\,\text{mm}}{15\,\text{mm}}\tan(\alpha/2) = 0.356$$

The value of $g_{L,0} = 2.6483 \times 10^{-2}$ was taken from the Table 4.2 for p = 400 MeV/c. The partition factors g_x, g_y, g_L are then calculated using eqns. 4.8, 4.9, and 4.10.

$$g_x = 1 - \Delta g = 0.644$$

$$g_y = 1$$

$$g_L = g_{L,0} + \Delta g = 0.383$$

The partition numbers are used in eqns. 4.4 and 4.5. The values gotten from the MAD-X cell simulation for the average betatron function, $< \beta_{x,y} >$, from equation 3.29, are used to calculate the expected cooling by the channel. It is done in order to optimize transverse emittance cooling while avoiding longitudinal emittance heating. The RF cavities configuration values are obtained from the G4beamline simulation. The calculated values are summarized in Table 6.1.

Table 6.1. Cell characteristics: δE_μ is calculated from eqn. 4.1 for a 3 cm LiH absorber. Parameters λ , $V_{RF,grad}$, and ϕ_s are the G4beamline RF setup parameters needed to recover the energy lost. The partition numbers, g_x, g_y, g_L, are then calculated using eqns. 4.8, 4.9, and 4.10. The average beta values are calculated from the MAD-X simulation using eqn. 3.29 and eqn. 4.6. Then eqns. 4.4 and 4.5 are used to find the equilibrium emittances. $T_{transit}$ is the transit time factor from eqn. 3.30.

Parameter	Value	Unit
δE_μ	4.867	MeV
λ_{RF}	461	mm
$T_{transit}$	0.876	-
ϕ_s	11.5	degrees
$V_{RF,grad}$	27.87	MV/m
$g_{L,0}$	0.0265	-
Δg	0.356	-
α wedge	105	degrees
$< \beta_x >$	2.978	cm
$< \beta_y >$	2.540	cm
$< \beta_L >$	34.083	cm
$\epsilon_{eq,x}$	265.84	μm
$\epsilon_{eq,y}$	146.01	μm
$\epsilon_{eq,L}$	1420.8	μm

The reference particle has a momentum of p = 400 MeV/c. It loses energy according to eqn. 4.1 that is calculated using the lithium hydride physical properties extracted from [87] and summarized in Table 4.2. The value for $g_{L,0}$ depends only of the particle mass, momentum, and ionization energy. The values for other materials are also in Table 4.2.

6.2   First Stage Simulation

The cell described previously was implemented in ICOOL. For testing the cooling rate, a 68 cell lattice with 3 cm wedge LiH absorbers at the low beta regions was chosen. To calibrate the RF gradients, as it was explained in Section 3.8.2, a G4beamline simulation was used with two full cells and 3 cm Lithium hydride absorbers. The simulation ran 2500 muons with a central momentum of p $= 400 \pm 13.2$ MeV/c through the channel. The initial transverse emittance is set to match the values given by the maximum transported emittance test as explained in Section 5.6. The initial beam sizes to match the emiitances are $\sigma X = 12.42$ mm, $\sigma p_X = 3.207$ MeV/c, $\sigma Y = 8.402$ mm $\sigma p_Y = 3.094$ MeV/c, $\sigma Z = 10$ mm and $\sigma p_Z = 13.21$ MeV/c. Sixty eight consecutive full cells (total length $= 130.56$ m) were used to test the cooling rate of the channel. Transmission of 58% is observed as Fig. 6.1 shows.
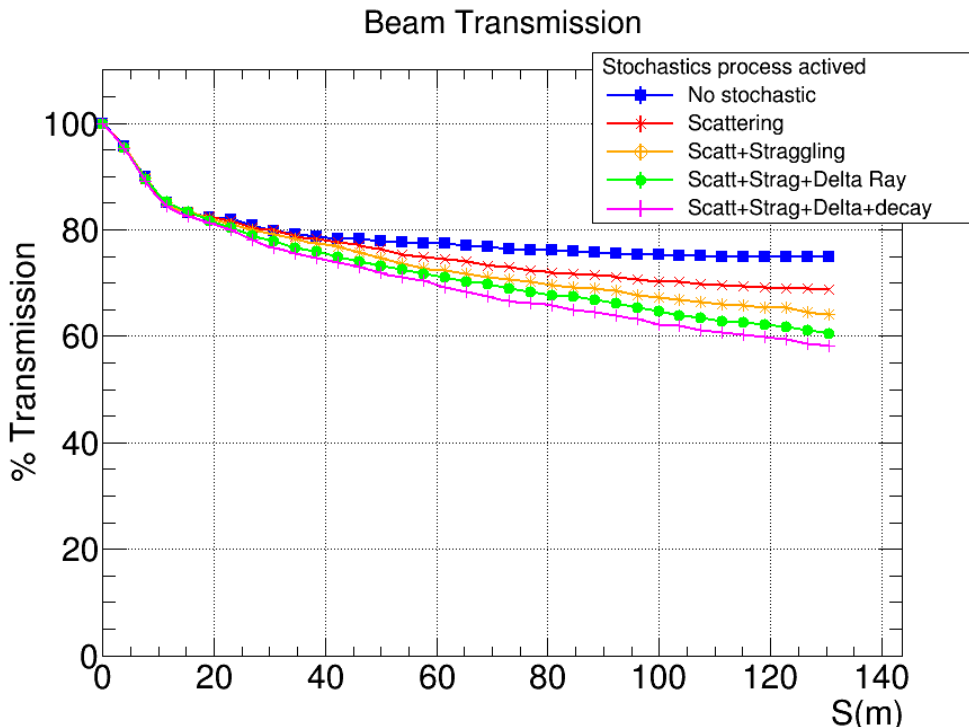
Figure 6.1. Transmission through a 130.56 meters long channel (68 full cells). The pink line is the simulation with all stochastic processes and decays on. The transmission is 58%. The green, yellow, and red lines evaluate the effect of stochastic processes on the transmission. The blue line is the reference line with all stochastic processes off.

The main sources of beam losses are scraping produced by magnet bores and the

low momentum band pass. The muons physics interactions that can be activated in the simulation are scattering, longitudinal strangling, delta rays, and muon decay. Particles can stochastically lose more energy than the value calculated using the Bethe eqn. 4.1. Thus, muons can have momentum below the 380 MeV/c limit. As was shown in Fig. 5.10 (c), the β_Y betatron function can increase in the Q2 magnet exceeding the magnet bore size. If a muon momentum exceeds the 424 MeV/c limit, the scraping takes place in the Q1 quadrupole magnet as was shown in Fig. 5.10 (a).
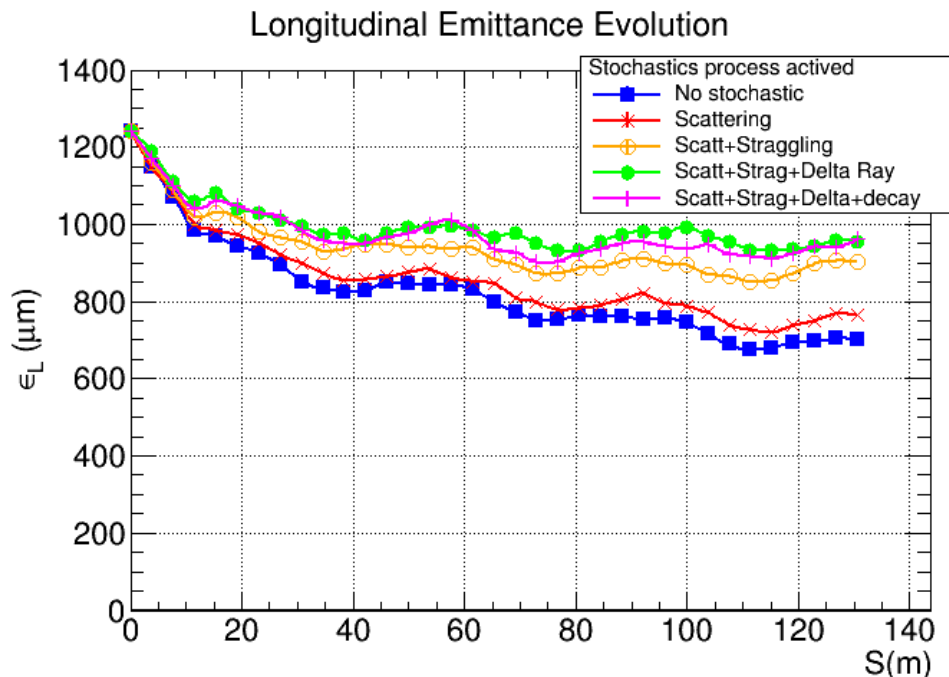
Figure 6.2. Longitudinal emittance evolution for Stage 1. X-Z emittance exchange prevents a natural longitudinal emittance increase.

The beam losses from scraping affect the longitudinal emittance. When stochastic process are turned off, the longitudinal emittance decreases, showing that the emittance exchange works as shown in Fig. 6.2. When the stochastic process are on, the longitudinal heating is due mainly to the strangling and delta ray emission processes. The fluctuations in the energy lost that are produced by straggling and delta rays are the main sources of off momentum particles being lost. If the muons were not quickly lost, cooling might be able to damp them back down into the muon bunch. Fig. 6.3 shows the emittance evolution for X

and Y in the transverse dimension. The additional effects of delta rays and straggling do not affect the transverse cooling significantly. Scraping affects X cooling more than Y cooling. It can perhaps be explained by the presence of the bending in the X plane that increases off momentum particle displacements.
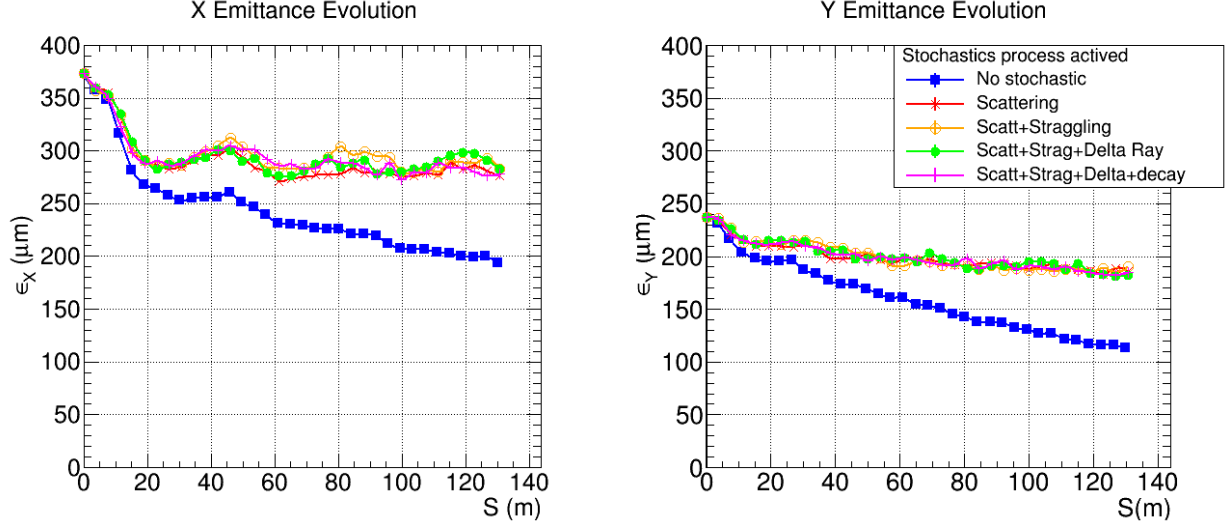
Figure 6.3. Transverse emittance evolution for Stage 1. With all stochastic process activated and decays, the initial X transverse emittance goes from 370 μm to 278 μm, the initial Y transverse emittance goes from 237 μm to 185 μm. Emittances are calculated using the ICOOL's EIGEMIT tool.

The 6D emittance evolution is plotted in Fig. 6.4. Most of the reduction occurs in the first 20 meters of the 130.56 meter long channel. The total $\epsilon_{6D,N}$ emittance is reduced from 0.11 mm^3 to 0.050mm^3. Note that (0.11 mm^3 /0.05 mm^3) is a 54% reduction. This reduction is a combination of beam loss through scraping and some beam cooling.

The first channel stage ICOOL simulation had initial transverse emittances of $\epsilon_{x,y,z}$ = (0.370, 0.237, 1.240) mm. The normalized emittances are reduced to $\epsilon_{x,y,z}$ = (0.278, 0.185, 0.963) mm as Fig. 6.3 shows. A 6D emittance reduction of 2.2 is observed. The emittance reduction is affected by the partition factors g_x, g_y, g_L and the heating. Fig. 6.2 shows the longitudinal emittance decreases. The cell was designed to keep the longitudinal emittance constant, but due to the beam losses it is reduced. Particles with momentum

6D Emittance Evolution
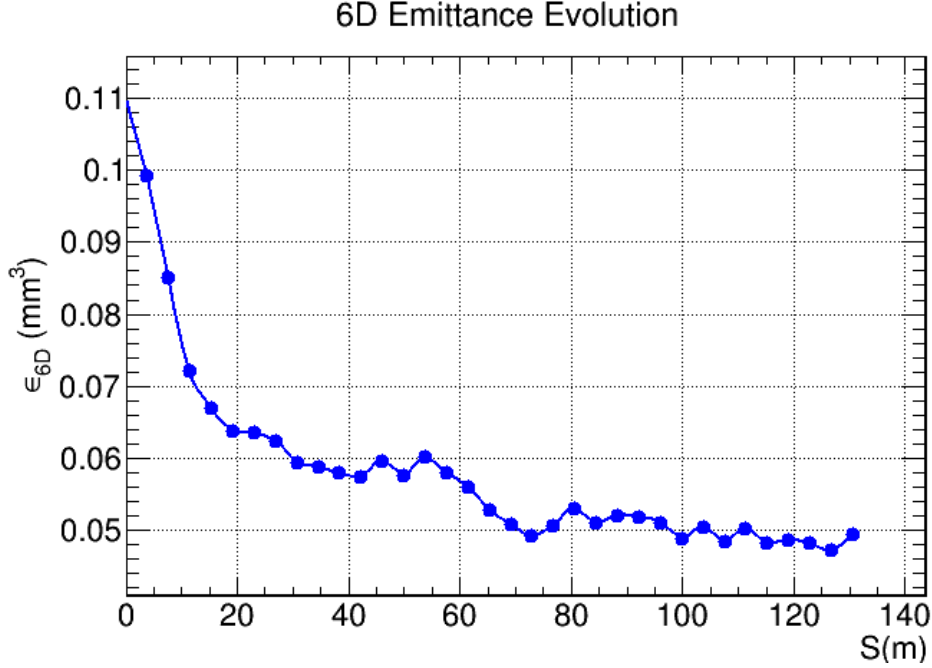
Figure 6.4. 6D emittance evolution for Stage 1. The initial emittance goes from from 0.11 mm^3 to 0.050 mm^3. Emittances are calculated using the ICOOL's EIGEMIT tool.

close to the limit tend to be lost first and it makes the longitudinal emittance decrease. The simulation successfully shows that some cooling using quadrupole focusing to get low betatron functions $(\beta_{x,y})$ at the absorber region is possible. The implemented wedge absorber makes the emittance exchange possible and avoids longitudinal heating.

Decays are unavoidable and the reason for using ionization cooling instead of other methods. The rate of cooling should be substantially faster than the decay rate. A merit efficiency factor [86] is defined by eqn. 6.1.

$$\text{Merit} = \frac{\epsilon_{6D}\text{In}}{\epsilon_{6D}\text{Out}} \times \%\text{Transmission} \tag{6.1}$$

A Merit factor greater than 1 is very desirable. Fig. 6.5 shows the merit factor for the 68 cell simulation with all stochastic process and decays on. The relatively low transmission and the reduction of the cooling rate at after the first 60 meters makes the Merit factor decrease.

61
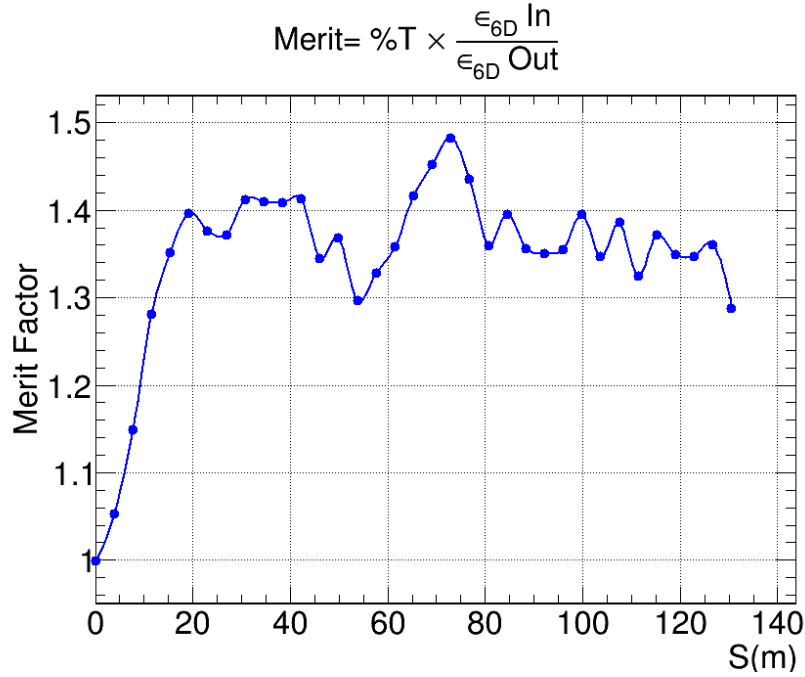
Figure 6.5. Merit cooling factor for Stage 1.

The effectiveness of the magnetic lattice is limited by the momentum acceptance. Especially for the Y momentum transmission band as was shown at Fig. 5.9. Some solutions have been studied such as the use of a short cell that reduces the natural chromaticity or the addition of sextupoles that correct the off momentum particle orbits. Short cells need small quadrupole bores increasing the required magnetic field and scraping beam losses. Sextupoles require dispersion at the sextupole magnets location and a π phase advance between the correction sextupoles in each dimension. Sextupoles probably will increase the length of the cell.

Table 6.2 summarizes the emittances used to get the cooling factor of the first stage. The equilibrium emittance is the minimum possible emittance that the stage can get. To cool under this limit the magnets strength have to be changed in order to lower the average betatron function. The final expected emittances are calculated using the equation 4.7 that take into account the equilibrium emittance, the initial emittance and the distance that the beam travels through the absorber material. The final expected emittances are calculated

Table 6.2. First Stage Channel emittances comparison. Equilibrium emittances are calculated from parameter Table 6.1 using equations 4.5 and 4.4. The initial emittances are set according to the channel admitance showed by the ICOOL simulation (no RF, no absorbers). The expected emittance is calculated using equation 4.7. The final ICOOL emittances are getting from the EIGEMIT ICOOL calculator. The calculated 6D emittance reduction is 1.4× and the ICOOL simulation gives a reduction of 2.2×, which includes some scraping as well as cooling.

| Emittance | ϵ_x | ϵ_y | ϵ_L | ϵ_{6D} |
	mm	mm	mm	mm^3
Equilibrium	0.2658	0.1460	1.4208	0.0551
Initial	0.3727	0.2367	1.2380	0.1092
Final Expected	0.3276	0.1847	1.2905	0.0781
Final ICOOL	0.2779	0.1852	0.9627	0.0496

from equation 4.7 for 68 cells that contains 2.04 m of LiH absorber material. Thus, no scraping is considered. The cooling factor is 1.4× if there is no scraping. Due to the scraping the ICOOL simulation has an emittance reduction factor of 2.2×. Most of the scraping occurs at the X dimension due to the emittance exchange and the narrow stable band width. The final cooling in Y coincides with the expected calculated cooling because the scraping is lower as Fig. 6.3 shows.

6.3 Channel Stages

Calculations [45], but not simulations, have been done for more channel stages to complete the 6D cooling. The low $\beta_\perp^*$ regions of these additional stages are occupied by absorbers made with different low Z materials such as lithium hydride, beryllium, or diamond. Table 6.3 shows why diamond is being considered. In spite of the equilibrium emittance increment of a factor of two from LiH to diamond, the energy lost per centimeter increases by a factor of four. Thus, the absorber thickness can be less with the same energy loss. If β^* is reduced enough, the transverse equilibrium emittance is reduced as well, and the desired cooling can still occur.

To optimize the channel length, four or five stages with different material absorbers

Table 6.3. Calculated equilibrium emittances for various materials. dE/ds is the energy loss at p = 400 MeV/c. The equilibrium emittances are calculated for $<\beta_\perp> = 2.5$ cm, $\beta_L = 40$ cm, wedge angle $\alpha_w = 105°$ and $\Delta g = 0.356$.

Material	dE/ds	$g_{L,0}$	$\epsilon_{X,eq}$	$\epsilon_{Y,eq}$	$\epsilon_{L,eq}$
	MeV/cm	$\times 10^{-2}$	μm	μm	μm
H_2 liquid	0.288	2.004	137.8	88.75	1626
LiH	1.622	2.648	223.2	143.8	1667
Be	3.075	3.414	324.1	208.8	1714
B_4C	4.334	3.836	407.6	262.5	1739
Diamond	6.474	3.712	454.9	288.8	1732

may be required. The expected emittance evolution through the channel is plotted in [45]. For 400 MeV/c muons, each channel stage length can be optimized in order to keep the total length as short as possible. Longitudinal betatron functions for dense materials are lower than 40 cm due to the smaller RF cavity voltage gradients needed to recover the lost energy. This may lower the amount of emittance exchange needed which would lead to lower transverse emittances.

Even the use of several stages is limited by the magnetic field required and by available superconducting quadrupole magnets. Also, reducing the transverse emittance below 100 μm will need longer channels at which the transmission can be affected by decays. A solution for final step in transverse emittance reduction below 100 μm is the use of a septa system. A diagrammatic representation of a septa system is shown in Fig. 6.6. A single
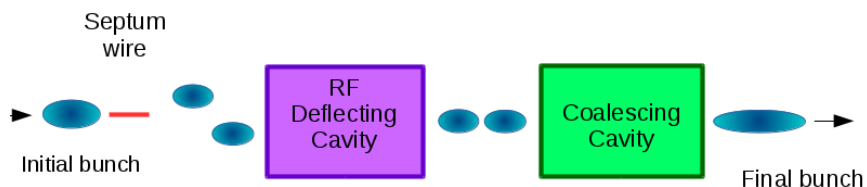
Figure 6.6. Septa scheme for the final step of transverse emittance reduction.

muon bunch is transversely sliced by electrostatic and magnetic septa into 17 parts. The Fermilab fixed target switchyard used septa to create multiple beams [88]. After that a series of RF deflecting cavities, as used in CERN Compact Linear Collider tests, forms a

3.7 meter long bunch train. Finally, snap bunch coalescence with RF combines the 17 muon bunches longitudinally. In snap bunch coalescence, all bunches are partially rotated during a quarter synchrotron period in energy-time space with a linear long wavelength RF bucket and then the bunches drift in a ring until they merge into one bunch and can be captured in a short wavelength RF bucket. Bunches drift together because they each have a slightly different energy set to cause the drift. Sets of 15 bunches were combined at Fermilab in the Tevatron. A 21 GeV ring has been simulated [89] with ESME [90] to demonstrate the coalescing of 17 muon bunches in 55 μs. The muon decay loss was 13%. The RF frequencies were 38.25 MHz and 1.3 GHz. The longitudinal packing fraction was as high as 87% and the initial normalized 2.4 mm longitudinal emittance increased by a factor of 17/0.87 to 47 mm. This is less than the 70 mm needed for a muon collider and allows for some dilution. Table 6.4 shows the train deflector steps to combine the 17 muon bunches into single long bunch.

Table 6.4. Seventeen muon bunches are combined into a 3.7 m long train using 10 RF Deflector Cavities. Each cavity interleaves two or three bunch trains. Deflection is ±4.5 mrad or zero at 300 MeV/c. The RF deflection frequencies are 731, 487, and 650 MHz. The final train has a 231 mm muon bunch spacing for acceleration by 1300 MHz RF cavities.

Number of Trains Interleaving	Number of RF Cavities	RF Wavelength	Output Spacing in Wavelengths	Output Bunch Spacing
$17 \to 6$	6	410 mm	9/4	923 mm
$6 \to 2$	3	616 mm	3/4	462 mm
$2 \to 1$	1	462 mm	1/2	231 mm

CHAPTER 7

CHROMATICITY CORRECTION STUDIES

The cooling channel presented in this work has been successful in showing that quadrupole lattices can produce effective cooling. But, the transmission needs to be improved. The stable transmission momentum band shown in Fig 5.8 is not wide enough to transport the longitudinal emittance, $\epsilon_L = 1600\,\mu\text{m}$, that the beam has at the beginning. The addition of sextupole magnets can produce chromatic correction and may be able to make the momentum band wide enough to increase the transmission to the required level. A momentum band pass increase from 6% to 10% is needed. To create chromatic correction, a sextupole magnet is placed after a quadrupole to correct the orbit of off momentum particles. It is necessary to have a non zero dispersion at the sextupole position as Fig. 7.1 shows.

A sextupole magnet deflects the particles in a different way, according to the position and momentum, making high momentum particles deflect more than low momentum particles. The correction makes the particles focus at the same position regardless of momentum. The sextupole principle has been tested in G4beamline with two muon beams with different central momentum as Fig. 7.2 shows. Focusing with just a single sextupole corrects the focus in the X dimension, but creates a fuzzy focus located at the absorber position.

Sextupole correction proposed by Rainmodi and Seryi [91] for the International Linear Collider (ILC) is shown in Fig. 7.3. The design has two widely separated quadrupole focusing defocussing doublets. Each quadrupole has either an X or a Y sextupole pole with it in a dispersive region. The X and Y sextupoles are interleaved. The phase advance between sextupoles in each coordinate is -I ($\Delta\mu_{x,y} = \pi = 180°$). The quadrupole doublets are point to point focusing, which creates a moderately low beta region half way in between the pairs of quadrupoles. This causes the 180° phase advance.
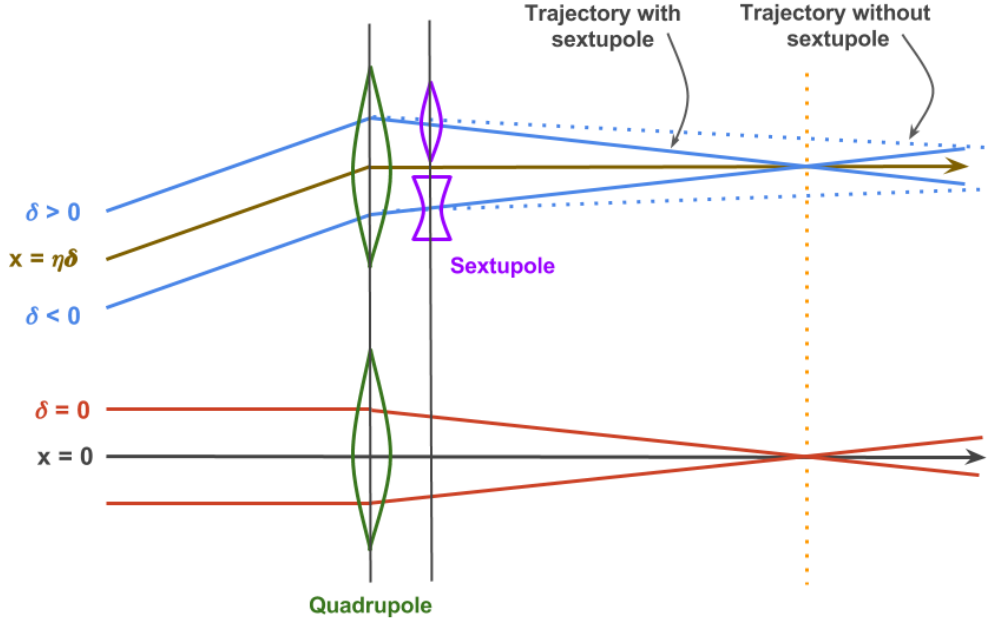
Figure 7.1. Sextupole chromatic correction principle.

Chromaticity is canceled locally by two sextupoles placed with the final focusing doublet. A gentle bend upstream generates dispersion across focusing doublet. Geometric aberrations of the final focusing doublet quadrupole/sextupole system are canceled by two more upstream and interleaved sextupoles (S_{F1}, S_{D1}) placed 180° out of phase with the two sextupoles nearest the IP.

A MAD-8 simulation for the ILC final focus is shown in Fig. 7.4. The sextupole positions are marked with a yellow and green lines. Between the quadrupole doublets the beam has a low beta region as Fig 7.4 (a) shows. This makes the phase advances $\mu_{x,y} = \pi$, as the bottom Fig. 7.4 (b) shows.

The outer final focus quadrupole pole tip field equals 1.60 T with L = 2.2 m. The inner final focus quadrupole pole tip field equals 2.83 T completing the final focus doublet. All other magnets have pole tip fields less than 1.0 T. The system requires relatively low magnetic field because electrons have to be gently bent to reduce synchrotron radiation.

The system can be adapted to the muon configuration by increasing the magnetic
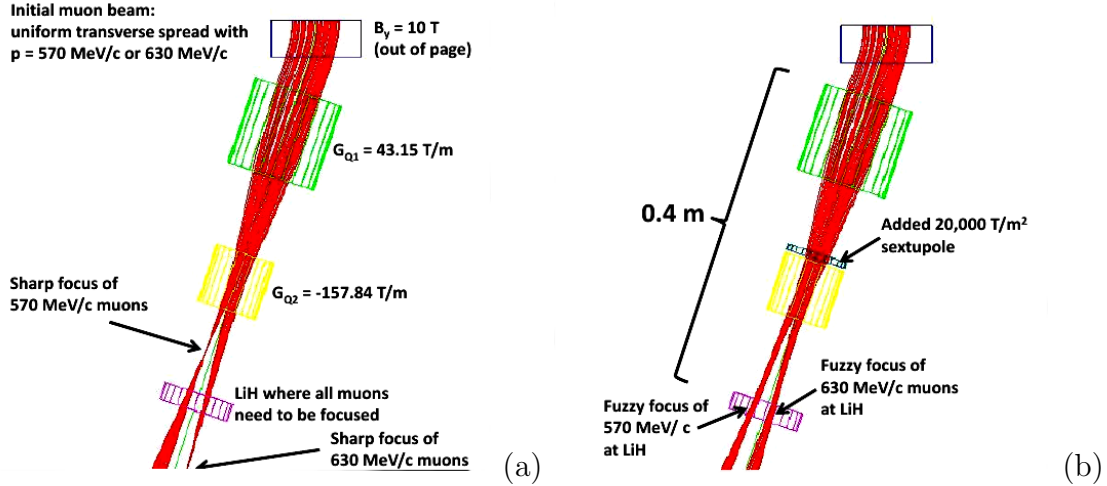
Figure 7.2. Focusing quadrupole doublet with dispersion created by a bending magnet. Two beams with momentum P = 570 MeV/c and P = 630 MeV/c are simulated with G4beamline. In (a) the system does not have a sextupole to correct the focus position. In (b) the focus at the absorber position is improved by the sextupole [92].
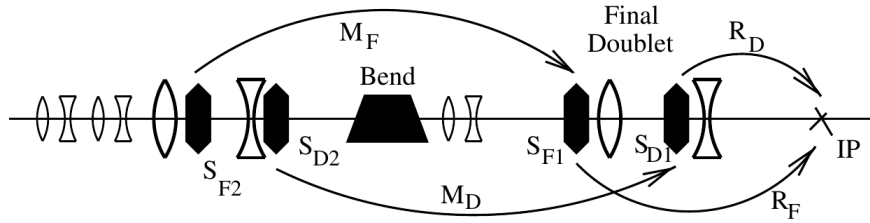
Figure 7.3. Raimondi sextupole layout for the ILC Final Focus [91].

pole tip field and reducing the magnet length. It can be done due to the heavy muon mass respect to the electron. Synchrotron radiation is low for muons. Also, the momentum beam momentum for the muon cooling system is 1250 times lower than the ILC electron momentum. To adapt the ILC final focus to the current quadrupole cooling channel configuration, four sextupoles have to be added. An additional low beta regions has to be located outside the central magnets to make the phase advance equal $\mu_{x,y} = \pi$ between X sextupole pairs and Y sextupole pairs. The possibility of implementing sextupole correction in the quadrupole cooling channel is still under study. The channel admittance and length can be affected and need to be optimized to keep the cooling efficient.

The strength of the chromaticity correction needed scales as the product of the momentum bandpass and the distance between the lithium hydride and the final focus quadrupoles all divided by β^* [93]. The amount of chromatic correction needed for muon cooling is relatively small.
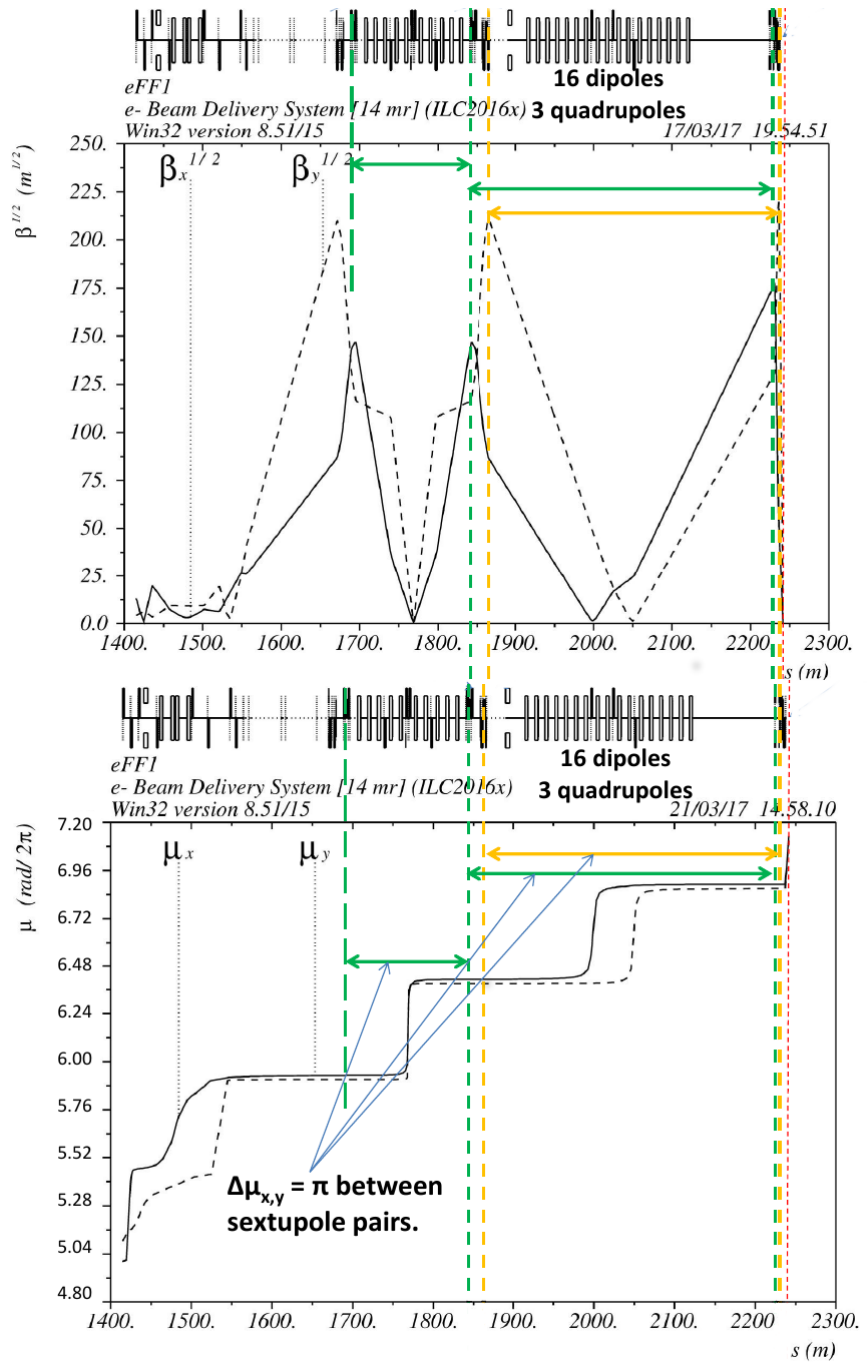
Figure 7.4. Raimondi sextupole plots for the ILC Final Focus [91].

CHAPTER 8

CONCLUSIONS

To meet the luminosity requirements of a muon collider, ionization cooling channels based on magnetic solenoids have been simulated with transverse betatron functions, $\beta_\perp$, as low as 3 cm. Emittance is reduced substantially. Further emittance reduction would provide yet higher muon collider luminosity. Muons in small, low emittance bunches collide more frequently than muons in large, high emittance bunches. The concept of using strong quadrupole focusing [94] with a relatively short cell is explored in this dissertation. Quadrupoles can provide a betatron focusing function below 3 cm, which is required to lower normalized transverse rms emittance below 280 μm. Strong focusing increases the angle at which muons pass through an absorber leading to more transverse momentum loss and more transverse cooling. The longitudinal momentum that is lost is replaced by radio frequency (RF) cavities.

Beam stability criteria, phase advances, and radio frequency cavity parameters were optimized herein to produce a magnetic lattice. Pole tip magnetic fields were limited to 14 T, which can be achieved using Nb_3Sn superconducting magnets. Quadrupole bore diameter and length are taken as equal. The drift spaces between quadrupoles are take to be greater the magnet radius in order to control fringe fields. For this work an ideal hard edge magnet model was used. Further studies of magnetic fringe fields might be considered for future improvements. The models for the physics processes that contribute to multiple scattering are contained in the G4beamline and ICOOL software that were used for quadrupole cooling channel simulation.

Quadrupole triplets provide low $\beta_\perp$ values at the absorber region. The inner quadrupoles are very close to the absorbers. Substantial RF is provided to increase longitudinal focusing.

The RF also replaces the longitudinal momentum lost in the absorbers. The transverse momentum that is lost in the absorbers provides the cooling. Dipole magnets provide dispersion to allow transverse to longitudinal emittance exchange with wedge shaped lithium hydride absorbers in the channel. The dipole bend direction alternates from cell to cell. The dipoles spread the beam so low momentum muons pass through the thin part of the wedge and high momentum muons pass through the thick part of the wedge.

The quadrupole channel herein shows a factor of 2.2 6D emittance reduction with 58% transmission through the first 130.56 meter long stage with scattering, straggling, delta rays, and muon decay turned on. Some of the emittance reduction is due to cooling and some to scraping. Four tapered stages may be required to reduce the 6D emittance to the required level, using various dense absorbers. The momentum acceptance needs to be improved from 6% to 10% by adding chromatic correction with sextupole magnet pairs to improve the transmission to 85%. Reverse emittance exchange with septa [45] and/or wedges [46] might then be used to decrease transverse emittance from 100 to 25 μm at the expense of longitudinal emittance to allow a $\sqrt{s} = 6$ TeV lepton collider [95].

Emittance reduction in Table 6.2 shows a final 6D emittance of 0.0496 mm^3 with 58% transmission using an ICOOL simulation. Some of the reduction is cooling and some scraping. It has been done using a quadrupole magnetic lattice that has lower equilibrium emittances than previous channels. The maximum quadrupole magnetic field required for the final cooling channel is 11.4 T. Superconducting magnets may be made of Nb$_3$Sn and may be able to reduce the equilibrium transverse emittance to levels close to 100 μm. The final 6D emittance obtained via ICOOL simulation indicates that the implementation of quadrupole focusing into a cooling channel with average transverse betatron functions below 3 cm is possible. Emittance exchange with wedges controls the longitudinal heating.

The transmission needs to increased by adding sextupoles to correct the trajectories of off momentum muons. Ignoring scraping, the final calculated but not simulated 6D emittance is 0.078 mm^3. The channel indicates that quadrupole focusing combined with final emittance

exchange may be able to reduce the emittance to the level required for a $\mathcal{L} \sim 10^{34}$ cm^{-2} s^{-1} muon collider.

This is the first time that any ionization cooling channel has indicated a 6D emittance below 0.1 mm^3. Cell transmission improvements should be possible by adding more magnetic elements, but this needs to be demonstrated. This work sets a pathway design for a high luminosity muon collider.

BIBLIOGRAPHY

[1] S. Chatrchyan *et al.* [CMS Collaboration], "Observation of a new boson at a mass of 125 GeV with the CMS experiment at the LHC," Phys. Lett. B **716** (2012) 30.

[2] G. Aad *et al.* [ATLAS Collaboration], "Observation of a new particle in the search for the Standard Model Higgs boson with the ATLAS detector at the LHC," Phys. Lett. B **716** (2012) 1.

[3] Carlo Rubbia, "A complete demonstrator of a muon cooled Higgs factory," arXiv:1306.2234.

[4] J. D. Jackson, "Classical Electrodynamics," ISBN-9780471309321 (1998).

[5] D. Neuffer, M. Palmer, Y. Alexahin, C. Ankenbrandt, and J. P. Delahaye, "A muon collider as a Higgs factory," IPAC-2013-TUPFI056, arXiv:1502.02042.

[6] M. Bonesini, "Perspectives for Muon Colliders and Neutrino Factories," Frascati Phys. Ser. **61** (2016) 11.

[7] D. Stratakis and R. B. Palmer, "Rectilinear six-dimensional ionization cooling channel for a muon collider: A theoretical and numerical study," Phys. Rev. ST Accel. Beams **18** (2015) 031003.

[8] R. B. Palmer, J. S. Berg, R. C. Fernow, J. C. Gallardo, H. G. Kirk, Y. Alexahin, D. Neuffer, S. A. Kakn, and D. Summers "A Complete Scheme of Ionization Cooling for a Muon Collider," Conf. Proc. C **070625** (2007) 3193.

[9] J. Acosta *et al.,* "Generating Low Beta Regions With Quadrupoles for Final Muon Cooling," IPAC-2017-MOPAB014.

[10] M. G. Minty and F. Zimmermann, "Measurement and control of charged particle beams," doi:10.1007/978-3-662-08581-3 (2003).

[11] M. Bogomilov *et al.* [MICE Collaboration], "Design and expected performance of the MICE demonstration of ionization cooling," arXiv:1701.06403.

[12] L. Cremaldi *et al.* [MICE Collaboration], "A Cherenkov Radiation Detector with High Density Aerogels," IEEE Trans. Nucl. Sci. **56** (2009) 1475.

[13] K. Ronald *et al.,* "'RF System for the MICE Demonstration of Ionisation Cooling," IVEC-2017, FERMILAB-CONF-17-071-AD.

[14] C. Rogers, "Measurement of Ionization Cooling With the MICE Experiment," IPAC-2017-WEPAB129.

[15] D. Neuffer *et al.,* "A Wedge Absorber Experiment at MICE," IPAC-2017-WEPAB133.

[16] D. Neuffer *et al.,* "Use of Wedge Absorbers in MICE," MICE-NOTE-508 (2017).

[17] D. Summers *et al.,* "More Muon Cooling plus Emittance Exchange with a Wedge," MICE-NOTE-499 (2016).

[18] A. N. Skrinsky, "Intersecting storage rings at Novosibirsk," Morges 1971, AIP Conf. Proc. **352** (1996) 6.

[19] D. Neuffer, "Colliding Muon Beams at 90 GeV," FERMILAB-FN-0319 (1979).

[20] D. V. Neuffer and R. B. Palmer, "A High-Energy High-Luminosity $\mu^+\mu^-$ Collider," EPAC 2004, BNL-61267.

[21] J. C. Gallardo *et al., $\mu^+\mu^-$* Collider: Feasibility Study," Snowmass 1996, BNL-52503.

[22] C. M. Ankenbrandt *et al.,* "Status of muon collider research and development and future plans," Phys. Rev. ST Accel. Beams **2** (1999) 081001.

[23] M. M. Alsharo'a *et al.,* "Recent progress in neutrino factory and muon collider research within the Muon collaboration," Phys. Rev. ST Accel. Beams **6** (2003) 081001.

[24] D. Neuffer *et al.,* "Muons for Particle Physics - Accomplishments of MAP," IPAC-2017-TUPIK038.

[25] J. P. Delahaye *et al.,* "Enabling Intensity and Energy Frontier Science with a Muon Accelerator Facility in the U.S.: A White Paper Submitted to the 2013 U.S. Community Summer Study of the Division of Particles and Fields of the American Physical Society," arXiv:1308.0494.

[26] R. B. Palmer *et al.,* "Muon Colliders," AIP Conf. Proc. **372** (1996) 3.

[27] R. B. Palmer *et al.,* "Muon Collider Design," Nucl. Phys. Proc. Suppl. **51A** (1996) 61.

[28] S. D. Holmes *et al.,* "Status and Opportunities at Project X: A Multi-MW Facility for Intensity Frontier Research," NAPAC 2013, arXiv:1409.5809.

[29] V. Lebedev and S. Nagaitsev, "Project X ICD-2 and its upgrades for Neutrino Factory or Muon Collider," AIP Conf. Proc. **1222** (2010) 274.

[30] K. T. McDonald *et al.,* "The MERIT High-Power Target Experiment at the CERN PS," Conf. Proc. C **100523** (2010) 3527.

[31] D. Neuffer *et al.* [Neutrino Factory and Muon Collider Collaboration], "Muon capture for the front end of a $\mu^+\mu^-$ collider," Conf. Proc. C **110328** (2011) 157.

[32] D. J. Summers, T. L. Hart, J. G. Acosta, L. M. Cremaldi, S. J. Oliveros, L. P. Perera, and D. V. Neuffer, "Muon Emittance Exchange with a Potato Slicer," arXiv:1504.03972.

[33] C. Yoshikawa *et al.,* "Status of the Complete Muon Cooling Channel Design and Simulations ," IPAC-2014-TUPME016.

[34] Y. Bao, G. Hanson, R. B. Palmer, and, D. Stratakis, "Conceptual design and modeling of a six-dimensional bunch merging scheme for a muon collider," Phys. Rev. Accel. Beams **19** (2016) 031001.

[35] A. Moretti, Z. Qian, J. Norem, Y. Torun, D. Li, and M. Zisman, "Effects of high solenoidal magnetic fields on rf accelerating cavities," Phys. Rev. ST Accel. Beams **6** (2005) 072001.

[36] R. B. Palmer, R. C. Fernow, J. C. Gallardo, D. Stratakis, and D. Li, "RF breakdown with external magnetic fields in 201 and 805 MHz cavities ," Phys. Rev. ST Accel. Beams **12** (2009) 031002.

[37] M. Chung, M. G. Collura, G. Flanagan, B Freemire,, P. M. Hanlet, M. R. Jana, R. P. Johnson, D. M. Kaplan, M. Leonova, A. Moretti M. Popovic, T. Schwarz, A. Tollestrup, Y. Torun, and K. Yonehara, "Pressurized H_2 RF Cavities in Ionizing Beams and Magnetic Fields," Phys. Rev. Lett. **111** (2013) 184802.

[38] B. Freemire, A. V. Tollestrup, K. Yonehara, M. Chung, Y. Torun, R. P. Johnson, G. Flanagan, P. M. Hanlet, M. G. Collura, M. R. Jana, M. Leonova, A. Moretti, and T. Schwarz, "Pressurized rf cavities in ionizing beams," Phys. Rev. Accel. Beams **19** (2016) 062004.

[39] D. Stratakis, "Advanced cooling scheme with gas filled rf cavities and discrete absorbers," AIP Conf. Proc. **1777** (2016) 100008.

[40] D. Stratakis, "A hybrid six-dimentional muon cooling channel using gas filled rf cavities," JINST (2017).

[41] W. E. Parkins, "The uranium bomb, the Calutron, and the space-charge problem," Phys. Today **58N5** (2005) 45.

[42] D. Stratakis, R. B. Palmer, J. S. Berg, and H. Witte, "Complete Six-dimensional Muon Cooling Channel for a Muon Collider," IPAC-2014-TUPME020.

[43] D. Stratakis, R. C. Fernow, J. S. Berg, and R. B. Palmer, "Tapered channel for six-dimensional muon cooling towards micron-scale emittances," Phys. Rev. ST Accel. Beams **16** (2013) 091001.

[44] R. B. Palmer , J. S. Berg, S. B. Bracker, L. M. Cremaldi, R. C. Fernow, J. C. Gallardo, R. Godang, G. G. Hanson, A. Klier, and D. J. Summers, " Ionization cooling ring for muons," Phys. Rev. ST Accel. Beams **8** (2005) 061003.

[45] D. Summers, J. Acosta, L. Cremaldi, T. Hart, S. Oliveros, L. Perera, W. Wu, and D. Neuffer, "Final Muon Emittance Exchange in Vacuum for a Collider," IPAC-2015-TUPWI044.

[46] D. Neuffer, "Phase space exchange in thick wedge absorbers for ionization cooling," AIP Conf. Proc. **441** (1998) 270.

[47] D. J. Summers, L. M. Cremaldi, R. Godang, B. R. Kipapa, H. E. Rice, and R. B. Palmer, "Muon acceleration to 750 GeV in the Tevatron tunnel for a 1.5 TeV $\mu^+\mu^-$ collider," Conf. Proc. C **070625** (2007) 3178.

[48] D. J. Summers *et al.*, "Test of a 1.8 Tesla, 400 Hz Dipole for a Muon Synchrotron," Conf. Proc. C **1205201** (2012) 3542.

[49] R. B. Palmer and R. Fernow, "An Overview of Muon Colliders," ICFA Beam Dyn. Newslett. **55** (2011) 22.

[50] D. J. Summers, "The top quark, the Higgs boson, and supersymmetry at $\mu^+\mu^-$ colliders," Bull. Am. Phys. Soc. **39** (1994) 1818.

[51] F. Su, J. Gao, M. Xiao, D. Wang, Y. W. Wang, S. Bai and T. J. Bian, "Method study of parameter choice for a circular proton-proton collider," Chin. Phys. C **40** (2016) 017001.

[52] E. D. Courant and H. S. Snyder, "Theory of the alternating gradient synchrotron," Annals Phys. **3** (1958) 1.

[53] H. Wollnik, "Optics of Charged Particles," doi:9780323156783 (1987).

[54] F. Tecker, "Longitudinal Beam Dynamics," CERN Accelerator School 2013, arXiv:1601.04901.

[55] A. W. Chao and M. Tigner, "Handbook of accelerator physics and engineering," Singapore: World Scientific (2006) 702 p.

[56] S. Y. Lee, "Accelerator physics," Singapore: World Scientific (1999) 491 p.

[57] A. Garren and H. Kirk, "Muon Cooling Ring Lattices with Quadrupoles and Dipoles," MAP-DOC-4408 (2002).

[58] M. J. Barnes *et al.,* "Injection and Extraction Magnets: Septa," arXiv:1103.1062.

[59] S. J. Oliveros, J. G. Acosta, L. M. Cremaldi and D. J. Summers, "Cooling for a High Luminosity 100 TeV Proton Antiproton Collider," COOL-2015-TUPF01.

[60] S. Oliversos *et al.,* "Exploration of a High Luminosity 100 TeV Proton Antiproton Collider," arXiv:1704.03891.

[61] S. J. Oliveros, "Design of a high luminosity 100 TeV proton-antiproton collider," Ph.D. Dissertation (2017).

[62] H. Grote and F. Schmidt, "MAD-X: An upgrade from MAD8,"

[63] W. Herr and F. Schmidt, "A MAD-X primer," CERN-AB-2004-027-ABP.

[64] S. Agostinelli *et al.,* "GEANT4: A Simulation toolkit," Nucl. Instrum. Meth. **A506** (2003) 250.

[65] Tom Roberts, G4Beamline User Guide 2.16,
http://www.muonsinternal.com/muons3/G4beamline;
T. J. Roberts *et al.,* PAC07-THPAN103 and EPAC08-WEPP120.

[66] R. C. Fernow, "ICOOL: A simulation code for ionization cooling of muon beams," eConf C **990329** (1999) THP31.

[67] R. C. Fernow, "Recent developments on the muon-facility design code ICOOL," Conf. Proc. C **0505161** (2005) 2651.

[68] R. Brun *et al.,* "Geant3," CERN-DD-EE-84-1.

[69] R. C. Fernow, "Physics analysis performed by ECALC9," FERMILAB-MUCOOL-280 (2003).

[70] E. R. Gray *et al.,* "Phase Space Cooling and $\bar{p}p$ Colliding Beams of Fermilab," IEEE Trans. Nucl. Sci. **24** (1977) 1854.

[71] T. Ellison *et al.,* "Electron Cooling and Accumulation of 200-MeV Protons at Fermilab," IEEE Trans. Nucl. Sci. **30** (1983) 2636.

[72] Delbert John Larson, "Intermediate Energy Electron Cooling for Antiproton Sources," FERMILAB-THESIS-1986-15.

[73] D. J. Larson, "Electron Cooling for a Muon Collider," (2011).

[74] C. Patrignani *et al.* [Particle Data Group], Chin. Phys. C **40** (2016) 100001.

[75] D. Neuffer, "Principles and Applications of Muon Cooling," Part. Accel. **14** (1983) 75.

[76] David Neuffer, "Comments on Ionization Cooling Channel Characteristics," MAP-DOC-4371, arXiv:1312.1266.

[77] Geant4 international collaboration,
http://geant4.web.cern.ch/geant4/UserDocumentation/UsersGuides/
PhysicsReferenceManual/fo/PhysicsReferenceManual.pdf

[78] J. Allison *et al.*, J. Phys. Conf. Ser. **396** (2012) 022013.

[79] J. Kunz, M. Berz, and P. Snopok, "Hybrid Methods for Muon Accelerator Simulations with Ionization Cooling," ICAP-2015-WECJI1.

[80] R. C. Fernow, "Scattering in ICOOL," FERMILAB-MUCOOL-336 (2006).

[81] T. Carlisle, "Step IV of the Muon Ionization Cooling Experiment (MICE) and the multiple scattering of muons," Ph.D. Dissertation (Dec 2013).

[82] H. Kirk, D. Cline, Y. Fukui, and A. Garren, "Muon storage rings for 6D phase-space cooling," Conf.Proc. **C030512** (2003) 2008.

[83] A. Garren, D. Cline, S. Kahn, H. Kirk, and F. Mills, "6D Cooling of a Circulating Muon Beam," AIP Conf. Proc. **821** (2006) 415.

[84] F. Borgnolutti *et al.,* "Fabrication of a Second-Generation of Nb$_3$Sn Coils for the LARP HQ02 Quadrupole Magnet," IEEE Trans. Appl. Supercond. **24** (2014) 4003005.

[85] P. Ferracin *et al.,* "Magnet Design of the 150 mm Aperture Low-β Quadrupoles for the High Luminosity LHC," IEEE Trans. Appl. Supercond. **24** (2014) 4002306.

[86] R. B. Palmer, "Cooling Efficiency Factor," NFMCC-DOC-250 (2002).

[87] K. A. Olive *et al.* [Particle Data Group], "Review of Particle Physics," Chin. Phys. C **38** (2014) 090001.

[88] L. W. Oleksiuk *et al.,* "The NAL beam splitting system," IEEE Trans. Nucl. Sci. **20** (1973) 428.

[89] R. P. Johnson, C. Ankenbrandt, C. Bhat, M. Popovic, S. A. Bogacz and Y. Derbenev, "Muon Bunch Coalescing," Conf. Proc. C **070625** (2007) 2930.

[90] S. Stahl and J. MacLachlan, "User's Guide to ESME v.7.1," FERMILAB-TM-1650 (1990).

[91] P. Raimondi and A. Seryi, "A Novel final focus design for future linear colliders," Phys. Rev. Lett. **86** (2001) 3779.

[92] J. G. Acosta *et al.,* "Final Muon Ionization Cooling Channel using Quadrupole Doublets for Strong Focusing," COOL-2015-MOPF07.

[93] Y. Cai, "Analytical approach to chromatic correction in the final focus system of circular colliders," Phys. Rev. Accel. Beams **19** (2016) 111006.

[94] S. Feher and J. Strait, "Estimated inner triplet quadrupole length and aperture for really large hadron colliders of E(beam) = 30, 60, and 100 TeV," Snowmass-1996-ACC042.

[95] M.-H. Wang *et al.,* "Design of a 6 TeV Muon Collider," JINST **11** (2016) P09003.

LIST OF APPENDICES

APPENDIX A: MAD-X CODE

```
// file: QUAD_DOUBLET_FC_4_JOHN.MDX
// MADX test: quadrupole doublet with coupling coils
// Authors: John Acosta and Terry Hart
// Date: May 9, 2016

// positive muon, p in GeV/c, pc in GeV
BEAM, PARTICLE=POSMUON,PC=0.400,DELTAP=0.004;

lQ0=0.125;
lRF=0.125;
lQ1=0.105;
lD1=0.050;
lQ2=0.065;
lD2=0.040;
lQ3=0.060;
lDH=0.015;

d0=lQ0/2.0+lRF;
d1=d0+lQ0/2.0+lRF*3/2.0;
d2=d1+lRF*3/2.0+lQ1/2.0;
d3=d2+lQ1/2.0+lD1+lQ2/2.0;
d4=d3+lQ2/2.0+lD2+lQ3/2.0;
d5=d4+lQ3/2.0+lDH;
d6=d5+lQ3/2.0+lDH;
d7=d6+lQ3/2.0+lD2+lQ2/2.0;
d8=d7+lQ2/2.0+lD1+lQ1/2.0;
d9=d8+lQ1/2.0+lRF*3/2.0;
d10=d9+lRF*3/2.0+lQ0/2;
d11=d10+lQ0/2.0+lRF;

pcm=400;

RF: RFCAVITY,L=lRF,FREQ=650,VOLT=27.8722;LAG=0.2007;
Q0: SBEND,L=lQ0,K1=-11.92727804*(299.792458/pcm);
Q1: SBEND,L=lQ1,K1=89.404784*(299.792458/pcm);
Q2: RBEND,L=LQ2,ANGLE=0.0333556,K1=-277.66542412*(299.792458/pcm);
Q3: RBEND,L=lQ3,ANGLE=0.0220003,K1=379.88547*(299.792458/pcm);
LIH_1: MARKER,AT=d5;
LIH_2: MARKER,AT=d11;

////////////////////////////////////////
//
// The 'at' is location of component center for MAD-X 5.02.00.
// For other MAD-X versions, the 'at' may be for the location
// of the start of the component.
//
FULL_CELL: SEQUENCE,REFER=ENRTY,L=d11;

RF: RF, AT=d0-lRF/2-lQ0/2;
Q0: Q0, AT=d0;
RF: RF, AT=d1-lRF;
RF: RF, AT=d1;
RF: RF, AT=d1+lRF;
Q1: Q1, AT=d2;
Q2: Q2, AT=d3;
```

```
Q3:  Q3,  AT=d4;
LIH_1,   AT=d5;
Q3:  Q3,  AT=d6;
Q2:  Q2,  AT=d7;
Q1:  Q1,  AT=d8;
RF:  RF,  AT=d9−lRF;
RF:  RF,  AT=d9;
RF:  RF,  AT=d9+lRF;
Q0:  Q0,  AT=d10;
RF:  RF,  AT=d10+lRF/2+lQ0/2;
LIH_2,   AT=d11;
ENDSEQUENCE;

USE,  PERIOD=FULL_CELL;
SURVEY,  FILE=survey.test;

TWISS,SAVE,BETX=1.549208885,BETY=1.086433948,alfx=0,alfy=0,dx=0;

PLOT,  NOVERSION=true,  HAXIS=S,  HMIN=d5−0.015,  HMAX=d5+0.015,
VAXIS1=BETX,BETY,  VMIN=0.0,−0.01 VMAX=0.07,0.01,  VAXIS2=DX,
COLOUR=100,  INTERPOLATE=TRUE,SYMBOL=2,  TITLE="unmatched beta functions";

PLOT,  NOVERSION=true,  HAXIS=S,  HMIN=d4−lQ3/2,  HMAX=d6+lQ3/2,
VAXIS1=BETX,BETY,  VMIN=0.0,−0.01 VMAX=0.35,0.01,  VAXIS2=DX,
COLOUR=100,  INTERPOLATE=TRUE,SYMBOL=2,  TITLE="unmatched beta functions";

PLOT,  NOVERSION=true,  HAXIS=S,  HMIN=0.0,  HMAX=d11,  VAXIS1=BETX,BETY,
 VMIN=0.0,−0.02 VMAX=13.0,0.02,  VAXIS2=DX,  COLOUR=100,  INTERPOLATE=TRUE,
 TITLE="unmatched beta functions";

MATCH,  SEQUENCE=FULL_CELL;
VARY,NAME=Q0−>K1,STEP=0.001;
VARY,NAME=Q1−>K1,STEP=0.001;
VARY,NAME=Q2−>K1,STEP=0.001;
VARY,NAME=Q3−>K1,STEP=0.001;
VARY,NAME=Q2−>ANGLE,STEP=0.001;
VARY,NAME=Q3−>ANGLE,STEP=0.001;

CONSTRAINT,SEQUENCE=FULL_CELL,RANGE=LIH_1,BETX=0.027;
CONSTRAINT,SEQUENCE=FULL_CELL,RANGE=LIH_1,BETY=0.022;
CONSTRAINT,SEQUENCE=FULL_CELL,RANGE=LIH_2,MUX=0.68;
CONSTRAINT,SEQUENCE=FULL_CELL,RANGE=LIH_2,MUY=0.70;
CONSTRAINT,SEQUENCE=FULL_CELL,RANGE=LIH_1,DX=0.0041;
CONSTRAINT,SEQUENCE=FULL_CELL,RANGE=LIH_2,DX=0.0;

MIGRAD,CALLS=200000,TOLERANCE=1E−21;  //LMDIF is default.
ENDMATCH;

TWISS;

PLOT,  NOVERSION=true,  HAXIS=S,  HMIN=d5−0.015,  HMAX=d5+0.015,
 VAXIS1=BETX,BETY,VAXIS2=DX,  VMIN=0.0,−0.01,  VMAX=0.03,0.01,
 COLOUR=100,  INTERPOLATE=TRUE,  TITLE="matched beta functions";

PLOT,  NOVERSION=true,  HAXIS=S,  HMIN=0,  HMAX=d11,  VAXIS1=BETX,BETY,
```

```
VAXIS2=DX, VMIN=0.0,−0.01, VMAX=10.0,0.01, COLOUR=100, INTERPOLATE=TRUE,
 TITLE="matched beta functions";

PLOT, NOVERSION=true, HAXIS=S, HMIN=d4−lQ3/2, HMAX=d6+lQ3/2,
VAXIS1=BETX,BETY, VMIN=0.0,−0.01 VMAX=0.35,0.01, VAXIS2=DX,
 COLOUR=100, INTERPOLATE=TRUE,SYMBOL=2, TITLE="unmatched beta functions";

SELECT,FLAG=SECTORMAP,clear;
SELECT,FLAG=TWISS,column=name,s,betx,bety,alfx,alfy,mux,muy,dx,dpx;
TWISS, file=optics.dat;
```

APPENDIX B: ICOOL Configuration file

multipole configuration, (APRIL, 2017) John Acosta

! Determined with MAD–X
! ――――――――――――――――

&SUB NCELLS   34

! wedge parameters (see ICOOL manual for details)

&SUB alpw   105   ! wedge total opening angle (degrees)
&SUB u   0.01151   ! +x displ. of wedge vertex (m) 1.5 cm /tan(alpha/2)
&SUB Zv   0.015   ! absorber half distance
&SUB phiw   180.0   ! rot. of 1st wedge around z axis (degrees)
&SUB W   0.02651   ! x width of wedge (m)
&SUB H   0.03   ! y height of wedge (m)

! set pzmean to 0.400 GeV/c
&SUB PZREF   0.400   ! GeV/c
&SUB XMEAN   0.000   ! m
&SUB YMEAN   0.000   ! m
&SUB ZMEAN   0.000   ! m
&SUB PXMEAN   0.000   ! GeV/c
&SUB PYMEAN   0.000   ! GeV/c
&SUB PZMEAN   0.400   ! GeV/c

! set initial spreads corresponding to what's seen at z = 11.52 m
! (emit_x_N, emit_y_N, emit_L_N) = (377, 246, 1250) microns
! for (beta_x, beta_y) = (1.5492, 1.0864) m

&SUB XSIG   0.01242   ! m
&SUB YSIG   0.008402   ! m
&SUB ZSIG   0.010   ! m
&SUB PXSIG   0.003207   ! GeV/c
&SUB PYSIG   0.003094   ! GeV/c
&SUB PZSIG   0.01321   ! GeV/c

! increase LiH density by 1.0 to make consistent with G4Beamline
&SUB LIHDENSFACTOR 1.0

! Qcoup dimensions and gradient
&SUB Q0LEN   0.125   ! m
&SUB Q0RAD   0.125   ! m
&SUB Q0GRAD   −12.23188 ! ! T/m

! Q1 dimensions and gradient
&SUB Q1LEN   0.105   ! m
&SUB Q1RAD   0.060   ! m
&SUB Q1GRAD   90.03749   ! T/m

! Q2 dimensions and gradient
&SUB Q2LEN   0.0650   ! m
&SUB Q2RAD   0.034   ! m
&SUB Q2DIP   0.68720027 !T

```
&SUB   Q2DIPb          −0.68720027  !T
&SUB   Q2GRAD          −274.94888   !  T/m


! QC  dimensions  and  gradient
&SUB   Q3LEN      0.060     !  m
&SUB   Q3RAD      0.034     !  m
&SUB   Q3DIP      0.33499748  !  T
&SUB   Q3DIPb    −0.33499748  !  T
&SUB   Q3GRAD     337.33070    !  T/m


! drift  spaces
&SUB   Q1Q2          0.050   !  m
&SUB   Q2Q3          0.040   !  m
&SUB   ABS           0.030   !  m


! RF  parameters
&SUB   rfLEN          0.125      !  m
&SUB   rfPH           11.5   degrees  with  respect  to  rising  zero  crossing
&SUB   rfGRAD         27.8722  !  MV/m
&SUB   rfFREQ         650        !  MHz
&SUB   rfRAD          0.125      !  m
&SUB   rfPH2          11.5  !  degrees  with  respect  to  rising  zero  crossing
&SUB   rfGRAD2        27.8722  !   MV/m


! tlh  set  rtuple  and  ntuple  both  to  false
! set  bgen  to  true

&cont npart=3000 bgen=.false. varstep=.true. nprnt=5 prlevel=1
bunchcut=100000000.0 bzfldprd=0.0 diagref=.true. output1=.true.
rtuple=.false. ntuple=.false. rtuplen=1 phasemodel=3 /


! beam  definition

&bmt nbeamtyp=1 /
1 2 1. 1                                            ! 1  mu  frac  gaussian
&XMEAN &YMEAN &ZMEAN &PXMEAN &PYMEAN &PZMEAN        ! mean: x y z px py pz
&XSIG  &YSIG  &ZSIG  &PXSIG  &PYSIG  &PZSIG         ! sigmas
0 /                                           ! If 0 No correlations
0  32.6  1.160  0.00 /
!2  22.4  0.669  0.00 /       ! Palmer correlation if previous parameter not zero


! (17.6 GeV/c, 0.593 m) for y, (1138.9 GeV/c, 15.1 m) for x
! particle interactions
&ints ldecay=.true. ldray=.true. lstrag=.true. lscatter=.true. /
! histograms
! TLH redid nemit planes.
&nhs /
&nsc /
&nzh /
&nrh /
&nem nemit=35 ipzcor=1 / after start and at end of each of 34 full cells
1  46  89  132  175  218  261  304  347  390  433  476  519  562  605  648  691  734  777
820  863  906  949  992  1035  1078  1121  1164  1207  1250  1293  1336  1379  1422  1465
&ncv /
```

```
SECTION
REFP                    ! set reference particle, need phasemodel=3
2 &PZREF 0 0 3    ! muon, pz0, t0, assumes constant reference particle velocity
DENS                    ! increase LiH density by factor of 1.275 to get
                        ! dE/dx = (5.13 MeV)/(3 cm)
LIH &LIHDENSFACTOR
!REPEAT                 ! repeat full cell NCELLS times
CELL
&NCELLS
.true.
NONE
0 0.0 0.0 0 0.0 0.0 0.0 0.0 0.0 0.0   0 0 0 0 0


!set up one full cell
!!!!!!!!!!!!!!!!!!!!!!!!!!!!!!!!!!!!!!!!!!!!!!!!!!!!!!!!!!!Set first single RFS
SREGION                    ! define RF cavity
&rfLEN 1 0.001             ! length, 1 radial region, radial step
1 0.0 &rfRAD               ! 1 radial region, min. and max. radii
ACCEL
2 &rfFREQ &rfGRAD &rfPH 0 0 0 0 0 0 0 0 0 0 0  ! model 1, freq, gradient, phase wrt 0
VAC
NONE
0. 0. 0. 0. 0.    0. 0. 0. 0. 0.


!!!!!!!!!!!!!!!!!!!!!!!!!!!!!!!!!!!!!!!!!!!!!!!!!!!!!!!!!!!End first single  RF set
SREGION                        ! define region of 1st coupling quadrupole
&Q0LEN 1 0.001             ! length, 1 radial region, radial step
1 0.0 &Q0RAD               ! 1 radial region, min. and max. radii
QUAD
1 &Q0GRAD 0 0 0  0 0 0 0 0    0 0 0 0 0    ! hard edge model, T/m
VAC
CBLOCK
0 0 0 0 0 0 0 0 0 0


!!!!!!!!!!!!!!!!!!!!!!!!!!!!!!!!!!!!!!!!!!!!!!!!!!!!!!!!!!!start second three  RF set
SREGION                    ! define RF cavity
&rfLEN 1 0.001             ! length, 1 radial region, radial step
1 0.0 &rfRAD               ! 1 radial region, min. and max. radii
ACCEL
2 &rfFREQ &rfGRAD &rfPH 0 0 0 0 0 0 0 0 0 0 0  ! model 1, freq, gradient, phase wrt 0
VAC
NONE
0. 0. 0. 0. 0.    0. 0. 0. 0. 0.


SREGION                    ! define RF cavity
&rfLEN 1 0.001             ! length, 1 radial region, radial step
1 0.0 &rfRAD               ! 1 radial region, min. and max. radii
ACCEL
2 &rfFREQ &rfGRAD &rfPH 0 0 0 0 0 0 0 0 0 0 0  ! model 1, freq, gradient, phase wrt 0
VAC
NONE
0. 0. 0. 0. 0.    0. 0. 0. 0. 0.


SREGION                    ! define RF cavity
&rfLEN 1 0.001             ! length, 1 radial region, radial step
```

```
1  0.0  &rfRAD                    !  1  radial  region ,  min.  and  max.  radii
ACCEL
2  &rfFREQ  &rfGRAD  &rfPH  0  0  0  0  0  0  0  0  0  0  0  0   !  model  1 ,  freq ,  gradient ,  phase  wrt  0
VAC
NONE
0.  0.  0.  0.  0.     0.  0.  0.  0.  0.


!!!!!!!!!!!!!!!!!!!!!!!!!!!!!!!!!!!!!!!!!!!!!!!!!!!!!!!!!!!!!!!!!! end  second  three  RF  set

SREGION                          !  define  region  of  1st  Q1
&Q1LEN  1  0.001                 !  length ,  1  radial  region ,  radial  step
1  0.0  &Q1RAD                    !  1  radial  region ,  min.  and  max.  radii
QUAD
1  &Q1GRAD  0  0  0   0  0  0  0  0    0  0  0  0  0    !  hard  edge  model ,  T/m
VAC
CBLOCK
0  0  0  0  0  0  0  0  0  0

SREGION                          !  define  first  drift  between  Q1–Q2
&Q1Q2  1  0.001         !  length ,  1  radial  region ,  radial  step
1  0.0  0.5                       !  1  radial  region ,  min.  and  max.  radii
NONE
0  0  0  0  0  0  0  0  0  0  0  0  0  0  0
VAC
CBLOCK
0  0  0  0  0  0  0  0  0  0

SREGION                          !  define  region  of  1st  Q2
&Q2LEN  1  0.001                 !  length ,  1  radial  region ,  radial  step
1  0.0  &Q2RAD                    !  1  radial  region ,  min.  and  max.  radii
DIP
1  &Q2DIP  0.0  &PZREF  &Q2GRAD    0.0  0.0  0  0  0  0  0  0  0  0  0 ! model  1 , dipole  field , − , ref. momentum
VAC
CBLOCK
0  0  0  0  0  0  0  0  0  0

SREGION                          !  define  first  drift  between  first  Q2  and  QC
&Q2Q3  1  0.001                  !  length ,  1  radial  region ,  radial  step
1  0.0  0.5                       !  1  radial  region ,  min.  and  max.  radii
NONE
0  0  0  0  0  0  0  0  0  0  0  0  0  0  0
VAC
CBLOCK
0  0  0  0  0  0  0  0  0  0

SREGION                          !  define  region  of  1st  side  of  QC  containing  vacuum
&Q3LEN  1  0.001            !  length ,  1  radial  region ,  radial  step
1  0.0  &Q3RAD             !  1  radial  region ,  min.  and  max.  radii
DIP
1  &Q3DIP  0.0  &PZREF  &Q3GRAD    0.0  0.0  0  0  0  0  0  0  0  0  0 ! model  1 , dipole  field , − , ref. momentum
LIH
!VAC
WEDGE
&alpw   0.0    0.06    180   0.015   &H   0.  0.  0.  0.  !ANG  RVERT  ZVERT  AZ  DX  DY
!CBLOCK
```

```
!0 0 0 0 0 0 0 0 0 0

SREGION                          ! define first Absorber wedge
&ABS 1 0.001          ! length , 1 radial region , radial step
1 0.0 0.5                          ! 1 radial region , min. and max. radii
NONE
0 0 0 0 0 0 0 0 0 0 0 0 0 0 0 0
LIH
!VAC
WEDGE
&alpw &u &Zv 180 &W &H 0. 0. 0. 0. !ANG RVERT ZVERT AZ DX DY
!CBLOCK
!0 0 0 0 0 0 0 0 0 0


SREGION                          ! define region of 1st side of QC containing vacuum
&Q3LEN 1 0.001          ! length , 1 radial region , radial step
1 0.0 &Q3RAD          ! 1 radial region , min. and max. radii
DIP
1 &Q3DIP 0.0 &PZREF &Q3GRAD  0.0 0.0 0 0 0 0 0 0 0 0 !model 1,dipole field ,−,ref.momentum
LIH
!VAC
WEDGE
&alpw  0.0  0.0  180  0.015  &H  0. 0. 0. 0. !ANG RVERT ZVERT AZ DX DY


SREGION                          ! define first drift between first Q2 and QC
&Q2Q3 1 0.001          ! length , 1 radial region , radial step
1 0.0 0.5                          ! 1 radial region , min. and max. radii
NONE
0 0 0 0 0 0 0 0 0 0 0 0 0 0 0 0
VAC
CBLOCK
0 0 0 0 0 0 0 0 0 0


SREGION                          ! define region of 1st Q2
&Q2LEN 1 0.001          ! length , 1 radial region , radial step
1 0.0 &Q2RAD          ! 1 radial region , min. and max. radii
DIP
1 &Q2DIP 0.0 &PZREF &Q2GRAD  0.0 0.0 0 0 0 0 0 0 0 0 !model 1,dipole field ,−,ref.momentum
VAC
CBLOCK
0 0 0 0 0 0 0 0 0 0


SREGION                          ! define first drift between Q1−Q2
&Q1Q2 1 0.001          ! length , 1 radial region , radial step
1 0.0 0.5                          ! 1 radial region , min. and max. radii
NONE
0 0 0 0 0 0 0 0 0 0 0 0 0 0 0 0
VAC
CBLOCK
0 0 0 0 0 0 0 0 0 0


SREGION                          ! define region of 2st Q1
&Q1LEN 1 0.001          ! length , 1 radial region , radial step
1 0.0 &Q1RAD          ! 1 radial region , min. and max. radii
QUAD
```

```
1 &Q1GRAD 0 0 0   0 0 0 0 0     0 0 0 0 0      ! hard edge model , T/m
VAC
CBLOCK
0 0 0 0 0 0 0 0 0 0


!!!!!!!!!!!!!!!!!!!!!!!!!!!!!!!!!!!!!!!!!!!!!!!!!!!!!!! start  third  three  RF  set


SREGION                        ! define RF cavity
&rfLEN 1 0.001                 ! length , 1 radial region , radial step
1 0.0 &rfRAD                   ! 1 radial region , min. and max. radii
ACCEL
2 &rfFREQ &rfGRAD2 &rfPH2 0 0 0 0 0 0 0 0 0 0 0  ! model 1, freq , gradient , phase wrt 0
VAC
NONE
0. 0. 0. 0. 0.    0. 0. 0. 0. 0.


SREGION                        ! define RF cavity
&rfLEN 1 0.001                 ! length , 1 radial region , radial step
1 0.0 &rfRAD                   ! 1 radial region , min. and max. radii
ACCEL
2 &rfFREQ &rfGRAD &rfPH 0 0 0 0 0 0 0 0 0 0 0  ! model 1, freq , gradient , phase wrt 0
VAC
NONE
0. 0. 0. 0. 0.    0. 0. 0. 0. 0.


SREGION                        ! define RF cavity
&rfLEN 1 0.001                 ! length , 1 radial region , radial step
1 0.0 &rfRAD                   ! 1 radial region , min. and max. radii
ACCEL
2 &rfFREQ &rfGRAD &rfPH 0 0 0 0 0 0 0 0 0 0 0  ! model 1, freq , gradient , phase wrt 0
VAC
NONE
0. 0. 0. 0. 0.    0. 0. 0. 0. 0.


!!!!!!!!!!!!!!!!!!!!!!!!!!!!!!!!!!!!!!!!!!!!!!!!!!!!!!!!!!! end  third  three  RF  set
SREGION                            ! define region of 2st coupling quadrupole
&Q0LEN 1 0.001                 ! length , 1 radial region , radial step
1 0.0 &Q0RAD                   ! 1 radial region , min. and max. radii
QUAD
1 &Q0GRAD 0 0 0   0 0 0 0 0     0 0 0 0 0      ! hard edge model , T/m
VAC
NONE
0. 0. 0. 0. 0.    0. 0. 0. 0. 0.


!!!!!!!!!!!!!!!!!!!!!!!!!!!!!!!!!!!!!!!!!!!!!!!!!!!!!!!!! end  fourth  single  RF  set


SREGION                        ! define RF cavity
&rfLEN 1 0.001                 ! length , 1 radial region , radial step
1 0.0 &rfRAD                   ! 1 radial region , min. and max. radii
ACCEL
2 &rfFREQ &rfGRAD &rfPH 0 0 0 0 0 0 0 0 0 0 0  ! model 1, freq , gradient , phase wrt 0
VAC
NONE
0. 0. 0. 0. 0.    0. 0. 0. 0. 0.
```

!!end fourth three RF set

%%
!set up second full cell
!!start fifth single RF set

SREGION   ! define RF cavity
&rfLEN 1 0.001   ! length, 1 radial region, radial step
1 0.0 &rfRAD   ! 1 radial region, min. and max. radii
ACCEL
2 &rfFREQ &rfGRAD &rfPH 0 0 0 0 0 0 0 0 0 0 0 0 ! model 1, freq, gradient, phase wrt 0
VAC
NONE
0. 0. 0. 0. 0.   0. 0. 0. 0. 0.

!!!end fifth single RF set

SREGION   ! define region of 1st coupling quadrupole
&Q0LEN 1 0.001   ! length, 1 radial region, radial step
1 0.0 &Q0RAD   ! 1 radial region, min. and max. radii
QUAD
1 &Q0GRAD 0 0 0 0 0 0 0 0   0 0 0 0 0   ! hard edge model, T/m
VAC
CBLOCK
0 0 0 0 0 0 0 0 0 0
!!start sixth three RF set

SREGION   ! define RF cavity
&rfLEN 1 0.001   ! length, 1 radial region, radial step
1 0.0 &rfRAD   ! 1 radial region, min. and max. radii
ACCEL
2 &rfFREQ &rfGRAD &rfPH 0 0 0 0 0 0 0 0 0 0 0 0 ! model 1, freq, gradient, phase wrt 0
VAC
NONE
0. 0. 0. 0. 0.   0. 0. 0. 0. 0.

SREGION   ! define RF cavity
&rfLEN 1 0.001   ! length, 1 radial region, radial step
1 0.0 &rfRAD   ! 1 radial region, min. and max. radii
ACCEL
2 &rfFREQ &rfGRAD &rfPH 0 0 0 0 0 0 0 0 0 0 0 0 ! model 1, freq, gradient, phase wrt 0
VAC
NONE
0. 0. 0. 0. 0.   0. 0. 0. 0. 0.

SREGION   ! define RF cavity
&rfLEN 1 0.001   ! length, 1 radial region, radial step
1 0.0 &rfRAD   ! 1 radial region, min. and max. radii
ACCEL
2 &rfFREQ &rfGRAD &rfPH 0 0 0 0 0 0 0 0 0 0 0 0 ! model 1, freq, gradient, phase wrt 0
VAC
NONE
0. 0. 0. 0. 0.   0. 0. 0. 0. 0.

!!!end sixth three RF set

```
SREGION                        ! define region of 1st Q1
&Q1LEN 1 0.001                 ! length, 1 radial region, radial step
1 0.0 &Q1RAD                   ! 1 radial region, min. and max. radii
QUAD
1 &Q1GRAD 0 0 0  0 0 0 0 0    0 0 0 0 0    ! hard edge model, T/m
VAC
CBLOCK
0 0 0 0 0 0 0 0 0 0


SREGION                        ! define first drift between Q1-Q2
&Q1Q2 1 0.001        ! length, 1 radial region, radial step
1 0.0 0.5                      ! 1 radial region, min. and max. radii
NONE
0 0 0 0 0 0 0 0 0 0 0 0 0 0 0
VAC
CBLOCK
0 0 0 0 0 0 0 0 0 0


SREGION                        ! define region of 1st Q2
&Q2LEN 1 0.001                 ! length, 1 radial region, radial step
1 0.0 &Q2RAD                   ! 1 radial region, min. and max. radii
DIP
1 &Q2DIPb 0.0 &PZREF &Q2GRAD   0.0 0.0 0 0 0 0 0 0 0 0 !model 1,dipole field,-,ref.momentum
VAC
CBLOCK
0 0 0 0 0 0 0 0 0 0


SREGION                        ! define first drift between first Q2 and QC
&Q2Q3 1 0.001                  ! length, 1 radial region, radial step
1 0.0 0.5                      ! 1 radial region, min. and max. radii
NONE
0 0 0 0 0 0 0 0 0 0 0 0 0 0 0
VAC
CBLOCK
0 0 0 0 0 0 0 0 0 0


SREGION                        ! define region of 1st side of QC containing vacuum
&Q3LEN 1 0.001                 ! length, 1 radial region, radial step
1 0.0 &Q3RAD                   ! 1 radial region, min. and max. radii
DIP
1 &Q3DIPb 0.0 &PZREF &Q3GRAD   0.0 0.0 0 0 0 0 0 0 0 0 !model 1,dipole field,-,ref.momentum
LIH
!VAC
WEDGE
&alpw   0.0   0.06   0   0.015   &H   0.  0.  0.  0.  !ANG RVERT ZVERT AZ DX DY


SREGION                        ! define first Absorber wedge
&ABS 1 0.001        ! length, 1 radial region, radial step
1 0.0 0.5                      ! 1 radial region, min. and max. radii
NONE
0 0 0 0 0 0 0 0 0 0 0 0 0 0 0
LIH
!VAC
WEDGE
&alpw   &u   &Zv   0   &W   &H   0.  0.  0.  0.  !ANG RVERT ZVERT AZ DX DY
```

```
SREGION                              ! define region of 1st side of QC containing vacuum
&Q3LEN 1 0.001             ! length, 1 radial region, radial step
1 0.0 &Q3RAD               ! 1 radial region, min. and max. radii
DIP
1 &Q3DIPb 0.0 &PZREF &Q3GRAD   0.0 0.0 0 0 0 0 0 0 0 0 !model 1,dipole field,−,ref.momentum
LIH
 !VAC
WEDGE
&alpw   0.0   0.0   0   0.015   &H   0.   0.   0.   0.   !ANG RVERT ZVERT AZ DX DY


SREGION                              ! define first drift between first Q2 and QC
&Q2Q3 1 0.001              ! length, 1 radial region, radial step
1 0.0 0.5                  ! 1 radial region, min. and max. radii
NONE
0 0 0 0 0 0 0 0 0 0 0 0 0 0 0
VAC
CBLOCK
0 0 0 0 0 0 0 0 0 0


SREGION                              ! define region of 1st Q2
&Q2LEN 1 0.001             ! length, 1 radial region, radial step
1 0.0 &Q2RAD               ! 1 radial region, min. and max. radii
DIP
1 &Q2DIPb 0.0 &PZREF &Q2GRAD   0.0 0.0 0 0 0 0 0 0 0 0 !model 1,dipole field,−,ref.momentum
VAC
CBLOCK
0 0 0 0 0 0 0 0 0 0


SREGION                              ! define first drift between Q1–Q2
&Q1Q2 1 0.001           ! length, 1 radial region, radial step
1 0.0 0.5                  ! 1 radial region, min. and max. radii
NONE
0 0 0 0 0 0 0 0 0 0 0 0 0 0 0
VAC
CBLOCK
0 0 0 0 0 0 0 0 0 0


SREGION                              ! define region of 2st Q1
&Q1LEN 1 0.001             ! length, 1 radial region, radial step
1 0.0 &Q1RAD               ! 1 radial region, min. and max. radii
QUAD
1 &Q1GRAD 0 0 0   0 0 0 0 0     0 0 0 0 0     ! hard edge model, T/m
VAC
CBLOCK
0 0 0 0 0 0 0 0 0 0


!!!!!!!!!!!!!!!!!!!!!!!!!!!!!!!!!!!!!!!!!!!!!!!!!!!!start seventh three RF set


SREGION                              ! define RF cavity
&rfLEN 1 0.001             ! length, 1 radial region, radial step
1 0.0 &rfRAD               ! 1 radial region, min. and max. radii
ACCEL
2 &rfFREQ &rfGRAD2 &rfPH2 0 0 0 0 0 0 0 0 0 0 0  ! model 1, freq, gradient, phase wrt 0
VAC
```

NONE
0. 0. 0. 0. 0.   0. 0. 0. 0. 0.

SREGION   ! define RF cavity
&rfLEN 1 0.001   ! length, 1 radial region, radial step
1 0.0 &rfRAD   ! 1 radial region, min. and max. radii
ACCEL
2 &rfFREQ &rfGRAD &rfPH 0 0 0 0 0 0 0 0 0 0 0 ! model 1, freq, gradient, phase wrt 0
VAC
NONE
0. 0. 0. 0. 0.   0. 0. 0. 0. 0.

SREGION   ! define RF cavity
&rfLEN 1 0.001   ! length, 1 radial region, radial step
1 0.0 &rfRAD   ! 1 radial region, min. and max. radii
ACCEL
2 &rfFREQ &rfGRAD &rfPH 0 0 0 0 0 0 0 0 0 0 0 ! model 1, freq, gradient, phase wrt 0
VAC
NONE
0. 0. 0. 0. 0.   0. 0. 0. 0. 0.

!!!end seventh three RF set

SREGION   ! define region of 2st coupling quadrupole
&Q0LEN 1 0.001   ! length, 1 radial region, radial step
1 0.0 &Q0RAD   ! 1 radial region, min. and max. radii
QUAD
1 &Q0GRAD 0 0 0 0 0 0 0 0   0 0 0 0 0   ! hard edge model, T/m
VAC
NONE
0. 0. 0. 0. 0.   0. 0. 0. 0. 0.

!!start eighth single RF set

! tlh put OUTPUT here and removed it from end of SREGION

OUTPUT
SREGION   ! define RF cavity
&rfLEN 1 0.001   ! length, 1 radial region, radial step
1 0.0 &rfRAD   ! 1 radial region, min. and max. radii
ACCEL
2 &rfFREQ &rfGRAD &rfPH 0 0 0 0 0 0 0 0 0 0 0 ! model 1, freq, gradient, phase wrt 0
VAC
NONE
0. 0. 0. 0. 0.   0. 0. 0. 0. 0.
!!!send eighth single RF set
ENDCELL
ENDREPEAT
ENDSECTION

APPENDIX C: G4BeamLine simulation CODE

```
// G4Beam Line Final Cooling cell Simulation
// John Acosta feb 2017
g4ui when=4 "/vis/viewer/set/background 1 1 1"
physics QGSP_BERT_EMX doStochastics=1 disable=Decay list=1


param pi=3.14159265
bug1021



particlecolor reference=0,0,1 mu+=0,0,1
reference referenceMomentum=400 particle=mu+

beam gaussian particle=mu+ nEvents=100 sigmaX=10 sigmaY=9 sigmaZ=12 sigmaXp=0.01 \
    sigmaYp=0.01 meanMomentum=400 sigmaP=12 beamX=0

trackcuts keep=mu+,nu_mu maxTime=100000.0
trace nTrace=10 format=root
param maxStep=0.5 SteppingVerbose=0

 zntuple format=root z=0,2734,1920*4,1920*33,1920*65
 beamlossntuple Lost1 format=root

param RFLEN=125
param RFRad=125
# Q0 dimensions and gradient

param   Q0LEN=125
param   Q0RAD=60
param   Q0GRAD=-12.23188

# Q1 dimensions and gradient
param   Q1LEN=105
param   Q1RAD=60
param   Q1GRAD=90.03749

# Q2 dimensions and gradient
param   Q2LEN=65
param   Q2RAD=32
param   Q2DIP=0.0   # 0.6840855725
param   Q2GRAD=-274.94888

# Q3 dimensions and gradient
param   Q3LEN=60
param   Q3RAD=30
param   Q3DIP=0.0   # 0.33499748
param   Q3GRAD=337.33070

# drift spaces
param   lD=50
param   lD1=40

tune Grad1 z0=0 z1=1920*2 initial=27.8722 step=0.01 expr=Pz1-Pz0 tolerance=0.001

pillbox RF1 color=0,1,1,0.4 innerLength=$RFLEN innerRadius=$RFRad+20 frequency=0.650
maxGradient=Grad1 irisRadius=$RFRad phaseAcc=11.5 maxStep=0.1 \
```

```
collarRadialThick=0.0  collarThick=0.0  win1Thick=0.25  \
win1OuterRadius=50  win2Thick=0.0  winMat=Vacuum

genericquad Q0 ironColor=0.26,0.9,0.8 fieldLength=$Q0LEN ironLength=$Q0LEN \
ironRadius=$Q0RAD+5 apertureRadius=$Q0RAD gradient=$Q0GRAD fringe=0 kill=1

genericquad Q1 ironColor=0.26,0.9,0.8 fieldLength=$Q1LEN ironLength=$Q1LEN \
ironRadius=$Q1RAD+5 apertureRadius=$Q1RAD gradient=$Q1GRAD fringe=0 kill=1

genericquad Q2 ironColor=0,1,0 fieldLength=$Q2LEN ironLength=$Q2LEN \
ironRadius=$Q2RAD+5 apertureRadius=$Q2RAD gradient=$Q2GRAD fringe=0 kill=1

multipole Q3 ironColor=1,1,0 fieldLength=$Q3LEN ironLength=$Q3LEN \
ironRadius=$Q3RAD+5 apertureRadius=$Q3RAD dipole=$Q3DIP quadrupole=$Q3GRAD \
 fringe=0 kill=1

tubs D length=$lD outerRadius=50 color=1,1,1 material=Vacuum
tubs D1 length=$lD1 outerRadius=50 color=1,1,1 material=Vacuum
tubs AbsD length=30 outerRadius=30 color=0.6,0.6,0.8 material=LITHIUM_HYDRIDE

group CellA
place RF1
place Q0
place RF1
place RF1
place RF1
place Q1
place D
place Q2
place D1
place Q3
place AbsD
place Q3
place D1
place Q2
place D
place Q1
place RF1
place RF1
place RF1
place Q0
place RF1
endgroup


place CellA copies=2


profile zloop=0:1920*66:1920 particle=mu+ file=profile.txt
```

APPENDIX D: MAD-8 Configuration file for Final ILC focus [91].

```
TITLE, "e- Beam Delivery System [14 mr] (ILC2016x)"

ASSIGN, PRINT="eBDS.print"
ASSIGN, ECHO="eBDS.echo"
OPTION, -INTER, -ECHO, VERIFY

CALL "eBDS.xsif"

! ================================================================
! Input beam definitions
! ----------------------------------------------------------------

! beam

EMITX  := EMITXBDS
EMITY  := EMITYBDS
ESPRD  := ESPRDE

BEAM, PARTICLE=ELECTRON, NPART=NPARTICLES, ENERGY=E0_BDS, &
EX=EMITX, EY=EMITY, SIGT=BLENG, SIGE=ESPRD

! sigma

TGAMX := (1+TALFX*TALFX)/TBETX
TGAMY := (1+TALFY*TALFY)/TBETY
SIG11 := EMITX*TBETX
SIG21 := -EMITX*TALFX
SIG22 := EMITX*TGAMX
SIG33 := EMITY*TBETY
SIG43 := -EMITY*TALFY
SIG44 := EMITY*TGAMY
C21   := SIG21/SQRT(SIG11*SIG22)
C43   := SIG43/SQRT(SIG33*SIG44)
SIG0  : SIGMA0, SIGX=SQRT(SIG11), SIGPX=SQRT(SIG22), R21=C21, &
SIGY=SQRT(SIG33), SIGPY=SQRT(SIG44), R43=C43, &
SIGT=BLENG, SIGPT=ESPRD

! ================================================================
! subroutines
! ----------------------------------------------------------------
/*
MGEO : SUBROUTINE
BEAM, ENERGY=E0_BDS
USE, EBDS
VALUE, TPS2EBDS_x, TPS2EBDS_y, TPS2EBDS_z,&
TPS2EBDS_theta, TPS2EBDS_phi, TPS2EBDS_psi
MATCH, BETA0=TWSS0, SURVEY, &
XS=TPS2EBDS_x, YS=TPS2EBDS_y, ZS=TPS2EBDS_z, &
THETAS=TPS2EBDS_theta, PHIS=TPS2EBDS_phi, PSIS=TPS2EBDS_psi
VARY, TPS2EBDS_x,      STEP=1.0E-06
!VARY, TPS2EBDS_y,      STEP=1.0E-06
VARY, TPS2EBDS_z,      STEP=1.0E-06
!VARY, TPS2EBDS_theta, STEP=1.0E-06
!VARY, TPS2EBDS_phi,    STEP=1.0E-06
!VARY, TPS2EBDS_psi,    STEP=1.0E-06
```

```
WEIGHT, XS=1, YS=0, ZS=1, THETAS=0, PHIS=0, PSIS=0
CONSTR, TEIP, XS=0, YS=0, ZS=0, THETAS=−0.007, PHIS=0, PSIS=0
LMDIF, TOL=1.E−20
MIGRAD, TOL=1.E−20
ENDMATCH
VALUE, TPS2EBDS_x,TPS2EBDS_y,TPS2EBDS_z,&
TPS2EBDS_theta,TPS2EBDS_phi,TPS2EBDS_psi
PRINT, FULL
SURVEY, TAPE="eBDS_survey.tape", &
X0=TPS2EBDS_x, Y0=TPS2EBDS_y, Z0=TPS2EBDS_z, &
THETA0=TPS2EBDS_theta, PHI0=TPS2EBDS_phi, PSI0=TPS2EBDS_psi
ENDSUBROUTINE


! —————————————————————————————————————————————————————————————


MTWSS0 : SUBROUTINE
BEAM, ENERGY=E0_BDS
USE, EBDS
VALUE, TPS2EBDS_TWISS[BETX],TPS2EBDS_TWISS[ALFX],&
TPS2EBDS_TWISS[BETY],TPS2EBDS_TWISS[ALFY]
MATCH, BETA0=TWSS0
VARY, TPS2EBDS_TWISS[BETX], STEP=1.0E−06, LOWER=0
VARY, TPS2EBDS_TWISS[ALFX], STEP=1.0E−06
VARY, TPS2EBDS_TWISS[BETY], STEP=1.0E−06, LOWER=0
VARY, TPS2EBDS_TWISS[ALFY], STEP=1.0E−06
WEIGHT, BETX=1/BXip, BETY=1/BYip
CONSTR, TEIP, BETX=BXip, ALFX=0, BETY=BYip, ALFY=0
LMDIF, TOL=1.E−20
MIGRAD, TOL=1.E−20
ENDMATCH
VALUE, TPS2EBDS_TWISS[BETX],TPS2EBDS_TWISS[ALFX],&
TPS2EBDS_TWISS[BETY],TPS2EBDS_TWISS[ALFY]
PRINT, FULL
TWISS, BETA0=TWSS0, SAVE, &
TAPE="eBDS_twiss.tape", RTAPE="eBDS_rmat.tape"
PLOT, TABLE=TWISS, HAXIS=S, VAXIS=RBETX,RBETY, &
STYLE=100, SPLINE=.T., FILE="eBDS", RANGE=#S/TEIP
PLOT, TABLE=TWISS, HAXIS=S, VAXIS=DX,DY, &
STYLE=100, SPLINE=.F., FILE="eBDS", RANGE=#S/TEIP
ENDSUBROUTINE
*/
! ═══════════════════════════════════════════════════════════
! COMMANDs
! —————————————————————————————————————————————————————————————


SETPLOT, XSIZE=25.4, YSIZE=20.32
SETPLOT, LWIDTH=5, LSCALE=1.5, SSCALE=1.5, RSCALE=1.5
OPTION, ECHO

!MGEO
!MTWSS0
!STOP

!COMMENT
BEAM, ENERGY=E0_BDS
```

```
USE, EBDS
PRINT, FULL
SURVEY, TAPE="eBDS_survey.tape", &
X0=TPS2EBDS_x, Y0=TPS2EBDS_y, Z0=TPS2EBDS_z, &
THETA0=TPS2EBDS_theta, PHI0=TPS2EBDS_phi, PSI0=TPS2EBDS_psi
 !ENDCOMMENT


 !COMMENT
BEAM, ENERGY=E0_BDS
USE, EBDS
PRINT, FULL
SAVEBETA, TWip, TEIP
TWISS, COUPLE, BETA0=TWSS0, SAVE, TAPE="eBDS_twiss.tape"
VALUE, TWip[BETX],TWip[ALFX],TWip[DX],TWip[DPX]
VALUE, TWip[BETY],TWip[ALFY],TWip[DY],TWip[DPY]


PLOT, TABLE=TWISS, HAXIS=S, VAXIS=RBETX,RBETY, &
STYLE=100, SPLINE=.T., TITLE="eBDS", FILE="eBDS"
PLOT, TABLE=TWISS, HAXIS=S, VAXIS=DX,DY, &
STYLE=100, SPLINE=.F., TITLE="eBDS", FILE="eBDS"


PLOT, TABLE=TWISS, HAXIS=S, VAXIS=BETX,BETY, &
STYLE=100, SPLINE=.T., FILE="eBDS", &
RANGE=EBSY1/EBSY2, TITLE="eBSY1+eBSY2"
PLOT, TABLE=TWISS, HAXIS=S, VAXIS=DX,DY, &
STYLE=100, SPLINE=.F., FILE="eBDS", &
RANGE=EBSY1/EBSY2, TITLE="eBSY1+eBSY2"


PLOT, TABLE=TWISS, HAXIS=S, VAXIS=RBETX,RBETY, &
STYLE=100, SPLINE=.T., FILE="eBDS", &
RANGE=ECOL1, TITLE="eCOL1"
PLOT, TABLE=TWISS, HAXIS=S, VAXIS=DX,DY, &
STYLE=100, SPLINE=.F., FILE="eBDS", &
RANGE=ECOL1, TITLE="eCOL1"


PLOT, TABLE=TWISS, HAXIS=S, VAXIS=RBETX,RBETY, &
STYLE=100, SPLINE=.T., FILE="eBDS", &
RANGE=EFF1, TITLE="eFF1"
PLOT, TABLE=TWISS, HAXIS=S, VAXIS=DX,DY, &
STYLE=100, SPLINE=.F., FILE="eBDS", &
RANGE=EFF1, TITLE="eFF1"


PLOT, TABLE=TWISS, HAXIS=S, VAXIS=RBETX,RBETY, &
STYLE=100, SPLINE=.T., FILE="eBDS", &
RANGE=EDL1, TITLE="eDL1"
PLOT, TABLE=TWISS, HAXIS=S, VAXIS=DX,DY, &
STYLE=100, SPLINE=.F., FILE="eBDS", &
RANGE=EDL1, TITLE="eDL1"
 !ENDCOMMENT


! _____


COMMENT
BEAM, ENERGY=E0_BDS
USE, EBSYDL
```

```
PRINT, FULL
SURVEY, TAPE="eBSYDL_survey.tape", &
X0=TPS2EBDS_x, Y0=TPS2EBDS_y, Z0=TPS2EBDS_z, &
THETA0=TPS2EBDS_theta, PHI0=TPS2EBDS_phi, PSI0=TPS2EBDS_psi
ENDCOMMENT


COMMENT
BEAM, ENERGY=E0_BDS
USE, EBSYDL
PRINT, FULL
TWISS, COUPLE, BETA0=TWSS0, SAVE, TAPE="eBSYDL_twiss.tape"
PLOT, TABLE=TWISS, HAXIS=S, VAXIS=BETX,BETY, &
COLOUR=100, STYLE=100, SPLINE=.T., FILE="eBSYDL", &
RANGE=#S/ENDDX, TITLE="eBSYD", VMIN=0, VMAX=400
PLOT, TABLE=TWISS, HAXIS=S, VAXIS=DX,DY, &
COLOUR=100, STYLE=100, SPLINE=.F., FILE="eBSYDL", &
RANGE=#S/ENDDX, TITLE="eBSYD"
ENDCOMMENT


! ————————————————————————————————————————————————————————


STOP
```

APPENDIX E: ICOOL simulation CODE for Garren's Lattice [82].

```
! file:   for001.dat
! Implementation of Garren's Lattice coling ring.
! Authors:   Terry Hart
Test of Ring Cooler−chgr_19_jun_02 qbq
&cont npart=1392   bgen=.false.
varstep=.true.  nprnt=1 prlevel=1 ntuple=.false.
phasemodel=3 output1=.true.  /
&bmt nbeamtyp=1 /
1 2 1. 2
0. 0.00020 0. 360. −0.00025 0.00035
0.0   0.00005 0.0 0.0 0.32 0.72
0
&ints ldecay=.true. ldedx=.true. lstrag=.true. lscatter=.true.
delev=2 straglev=4 scatlev=4  /
&nhs nhist=6   /
−0.25   0.01 50 1 1
−0.25   0.01 50 2 1
−0.50   0.02 50 7 1
−0.25   0.01 50 4 1
−0.25   0.01 50 5 1
0.43 3.4e−3 50 6 1
&nsc nscat=0   /
&nzh nzhist=0   /
&nrh   /
&nem   /
&ncv   /
SECTION
REFP
2 0.2500   0.0 7.107767979 4
! Start cell
REPEAT
256
SREGION             ! RF
0.5   1     1e−3
1   0.    0.21
ACCEL
2.   201.25    16.00   33.867437346975  0.    0. 0. 0. 0. 0.    0. 0. 0. 0. 0. !
VAC
NONE
0. 0. 0. 0. 0.    0. 0. 0. 0. 0.
SREGION           ! Drift
0.050281732  1     1e−3
1   0.    0.21
NONE
0. 0. 0. 0. 0.    0. 0. 0. 0. 0.    0. 0. 0. 0. 0.
VAC
NONE
0. 0. 0. 0. 0.    0. 0. 0. 0. 0.
SREGION           ! QUAD #2
0.200   1     5e−3
1   0.    0.21
QUAD
1.    5.939151800 0. 0. 0. 0. 0. 0. 0. 0. 0. 0. 0. 0. 0. ! Gradient Q2∗1.00
!1. 11.8783036 0. 0. 0. 0. 0. 0. 0. 0. 0. 0. 0. 0. 0.
VAC
```

106

NONE

0. 0. 0. 0. 0.   0. 0. 0. 0. 0.

SREGION   ! drift

0.25532369 1 2e−3

1   0.   0.21

NONE

0. 0. 0. 0. 0.   0. 0. 0. 0. 0.   0. 0. 0. 0. 0.

VAC

CBLOCK

0. 0. 0. 0. 0.   0. 0. 0. 0. 0.

SREGION   ! QUAD #B

0.050   1   5e−3

1   0.   0.21

QUAD

1. −25.402950036 0. 0. 0. 0. 0. 0. 0. 0. 0. 0. 0. 0. 0. ! Gradient QB∗1.00

!1.   −50.80590006 0. 0. 0. 0. 0. 0. 0. 0. 0. 0. 0. 0. 0.

VAC

NONE

0. 0. 0. 0. 0.   0. 0. 0. 0. 0.

SREGION   ! Horizontal bend dipole

0.100   1   5e−3

1   0.   0.21

DIP

1.   3.325238384 0. 0.25385380306549057   0. 0. 0. 0. 0. 0. 0. 0. 0. 0. 0.

!1.   6.650476768 0. 0.507707606   0. 0. 0. 0. 0. 0. 0. 0. 0. 0. 0.

VAC

NONE

0. 0. 0. 0. 0.   0. 0. 0. 0. 0.

SREGION   ! QUAD #B

0.050   1   5e−3

1   0.   0.21

QUAD

1. −25.402950036 0. 0. 0. 0. 0. 0. 0. 0. 0. 0. 0. 0. 0. ! Gradient QB∗1.00

!1.   −50.80590006 0. 0. 0. 0. 0. 0. 0. 0. 0. 0. 0. 0. 0.

VAC

NONE

0. 0. 0. 0. 0.   0. 0. 0. 0. 0.

SREGION   ! drift

0.250   1 2e−3

1   0.   0.21

NONE

0. 0. 0. 0. 0.   0. 0. 0. 0. 0.   0. 0. 0. 0. 0.

VAC

CBLOCK

0. 0. 0. 0. 0.   0. 0. 0. 0. 0.

SREGION   ! QUAD #1

0.200   1   5e−3

1   0.   0.21

QUAD

1.   10.288566494 0. 0. 0. 0. 0. 0. 0. 0. 0. 0. 0. 0. 0. ! Gradient Q1∗1.00

!1.   20.57713298   0. 0. 0. 0. 0. 0. 0. 0. 0. 0. 0. 0. 0.

VAC

NONE

0. 0. 0. 0. 0.   0. 0. 0. 0. 0.

SREGION   ! drift

```
0.035          1  2e−3
1   0.    0.21
NONE
0.  0.  0.  0.  0.    0.  0.  0.  0.  0.    0.  0.  0.  0.  0.
VAC
CBLOCK
0.  0.  0.  0.  0.    0.  0.  0.  0.  0.
SREGION                          ! 1st half 20 deg WEDGE FOR BENDING RING
0.240  1  1e−3
1   0.    0.21
NONE
0.0   0.0   0.0   0.0   0.0    0.    0.  0.  0.  0.    0.  0.  0.  0.  0.
LH
!VAC
WEDGE
40.0   0.329697331323739 0.24   180.0   1.60   0.50   0.  0.  0.  0. !ANG RVERT ZVERT AZ DX DY
SREGION                          ! 2nd half 20 deg WEDGE FOR BENDING RING
0.240  1  1e−3
1   0.    0.21
NONE
0.0   0.0   0.0   0.0   0.0    0.    0.  0.  0.  0.    0.  0.  0.  0.  0.
LH
!VAC
WEDGE
40.0   0.329697331323739 0.00   180.0   1.60   0.50   0.  0.  0.  0. !ANG RVERT ZVERT AZ DX DY
SREGION          !  drift
0.035          1  2e−3
1   0.    0.21
NONE
0.  0.  0.  0.  0.    0.  0.  0.  0.  0.    0.  0.  0.  0.  0.
VAC
CBLOCK
0.  0.  0.  0.  0.    0.  0.  0.  0.  0.
SREGION            ! QUAD #1
0.200  1    5e−3
1   0.    0.21
QUAD
1.    9.975815284 0. 0. 0. 0. 0. 0. 0. 0. 0. 0. 0. 0. ! Gradient Q1*1.00
!1.   19.95163057    0. 0. 0. 0. 0. 0. 0. 0. 0. 0. 0. 0. 0.
VAC
NONE
0.  0.  0.  0.  0.    0.  0.  0.  0.  0.
SREGION            !  drift
0.250          1  2e−3
1   0.    0.21
NONE
0.  0.  0.  0.  0.    0.  0.  0.  0.  0.    0.  0.  0.  0.  0.
VAC
CBLOCK
0.  0.  0.  0.  0.    0.  0.  0.  0.  0.
SREGION            ! QUAD #B
0.050  1    5e−3
1   0.    0.21
QUAD
1.  −24.630752727 0. 0. 0. 0. 0. 0. 0. 0. 0. 0. 0. 0. ! Gradient QB*1.00
```

!1. −49.26150544   0. 0. 0. 0. 0. 0. 0. 0. 0. 0. 0. 0. 0.
VAC
NONE
0. 0. 0. 0. 0.   0. 0. 0. 0. 0.
SREGION   ! Horizontal bend dipole
0.100 1   5e−3
1 0.   0.21
DIP
1. 3.224157993 0. 0.24613717080719084 0. 0. 0. 0. 0. 0. 0. 0. 0. 0. 0.
!1.   6.448315986 0.   0.492274356   0. 0. 0. 0. 0. 0. 0. 0. 0. 0. 0.
VAC
NONE
0. 0. 0. 0. 0.   0. 0. 0. 0. 0.
SREGION   ! QUAD #B
0.050 1   5e−3
1 0.   0.21
QUAD
1. −24.630752727 0. 0. 0. 0. 0. 0. 0. 0. 0. 0. 0. 0. 0. 0. ! Gradient QB∗1.00
!1.   −49.26150544   0. 0. 0. 0. 0. 0. 0. 0. 0. 0. 0. 0. 0.
VAC
NONE
0. 0. 0. 0. 0.   0. 0. 0. 0. 0.
SREGION   ! drift
0.25532369 1 2e−3
1 0.   0.21
NONE
0. 0. 0. 0. 0.   0. 0. 0. 0. 0.   0. 0. 0. 0. 0.
VAC
CBLOCK
0. 0. 0. 0. 0.   0. 0. 0. 0. 0.
SREGION   ! QUAD #2
0.200 1   5e−3
1 0.   0.21
QUAD
1.   5.758613829 0. 0. 0. 0. 0. 0. 0. 0. 0. 0. 0. 0. 0. 0. ! Gradient Q2∗1.00
!1.   11.51722766   0. 0. 0. 0. 0. 0. 0. 0. 0. 0. 0. 0. 0.
VAC
NONE
0. 0. 0. 0. 0.   0. 0. 0. 0. 0.
SREGION   ! Drift
0.050281732 1   1e−3
1 0.   0.21
NONE
0. 0. 0. 0. 0.   0. 0. 0. 0. 0.   0. 0. 0. 0. 0.
VAC
NONE
0. 0. 0. 0. 0.   0. 0. 0. 0. 0.
OUTPUT
SREGION   ! RF
0.5 1   1e−3
1 0.   0.21
ACCEL
2. 201.25   16.00 33.814460000000 0.   0. 0. 0. 0. 0.   0. 0. 0. 0. 0. 0. !
VAC
NONE

0. 0. 0. 0. 0.   0. 0. 0. 0. 0.
ENDREPEAT
ENDSECTION

John G. Acosta Castillo

Education

Ph.D. Candidate in Physics, University of Mississippi - Oxford, 2017.

M.A in Physics, University of Mississippi - Oxford, 2014.

M.S in Physics, University of Puerto Rico - Mayaguez, 2010.

B.S in Physics, District University of Bogota - Colombia, 2005.

Teaching Experience

Teaching Assistant, Department of Physics and Astronomy, University of Mississippi 2011-2013.

Teaching Assistant, Department of Physics, University of Puerto Rico - Mayaguez 2007.

Research Interests

Accelerator Particle Physics

Publications

• J. G. Acosta, et al. Final Muon Ionization Cooling Channel using Quadrupole Doublets for Strong Focusing, COOL-2015-MOPF07.

• T. L. Hart, J. G. Acosta, L. M. Cremaldi, S. J. Oliveros, D. J. Summers and D. V. Neuffer. Final 6d Muon Ionization Cooling Using Strong Focusing Quadrupoles, NAPAC-2016-TUPOB44.

- S. J. Oliveros, D. J. Summers, L. M. Cremaldi, and J. G. Acosta. High Luminosity 100 TeV Proton Antiproton Collider, NAPAC-2016-MOB3CO04.

- S. J. Oliveros, D. J. Summers, L. M. Cremaldi, and J. G. Acosta. Exploration of a High Luminosity 100 TeV Proton Antiproton Collider, SESAPS-2015-C2-3.

- S. J. Oliveros, J. G. Acosta, L. M. Cremaldi, D. J. Summers. Cooling for a High Luminosity 100 TeV Proton Antiproton Collider, COOL-2015-TUPF01.

- David Neuffer, J. Acosta and D. Summers, T. Mohayai and P. Snopok. Wedge Absorbers For Muon Cooling With a Test Beam At MICE. FERMILAB-CONF-16-459-AD-APC. arXiv:1612.07369 [physics.acc-ph]

- Don Summers, John Acosta, Lucien Cremaldi, Terry Hart, Sandra Oliveros, Lalith Perera, Wanwei Wu and David Neuffer. Final Muon Emittance Exchange in Vacuum for a Collider, IPAC-2015-TUPWI044 (arXiv:1505.01832).

- D.J. Summers, T.L. Hart, J.G. Acosta, L.M. Cremaldi, S.J. Oliveros, L.P. Perera and D.V. Neuffer. Muon Emittance Exchange with a Potato Slicer, arXiv:1504.03972.

- T.Rohe, J.Acosta, A.Bean, S.Dambach, W.Erdmann, U.Langenegger, C.Martin, B. Meier, V.Radicci, J.Sibille and, P.Trub. Signal height in silicon pixel detectors irradiated with pions and protons. Nucl.Instrum.Meth.A612:493-496,2010. arXiv:0901.3422 [physics.ins-det].

Colombian Journal of Physics:

- J. Acosta, S. Oliveros, and N. Forero. Diseno y construccion de un monocromador controlado con Labview. En: Colombia Revista Colombiana De Fisica ISSN: 01202650 ed: Revista De La Sociedad Colombiana De Fisica.v.38 fasc.4 p.1655-1659, 2006

- J. Acosta, S. Oliveros, and N. Forero. Determinacion del tiempo de respuesta de una termopila. En: Colombia Revista Colombiana De Fisica ISSN: 01202650 ed: Revista De La Sociedad Colombiana De Fisica v.38 fasc.2 p.758-762, 2006.

- S. Oliveros, J. Acosta, and N. Forero. Analisis espectral de la radiacion termica del tungsteno utilizando Labview . En: Colombia Revista Colombiana De Fisica ISSN: 012022650 ed: Revista De La Sociedad Colombiana De Fisica v.38 fasc.4 p.1671-1675, 2006.

Workshop - Conference Presentations

- Final 6d Muon Ionization Cooling Using Strong Focusing Quadrupoles. NAPAC 2016 Conference, Chicago IL, October 2016.

- Quadrupole Doublet Channel and Septa Emittance Exchange for Muon Collider Final Cooling. SESAPS 2015 Conference, Mobile AL, November 2015.

- Final Muon Ionization Cooling Channel using Quadrupole Doublets for Strong Focusing. COOL Workshop 2015 - Poster Session, Jefferson Lab (Newport News, VA), July 2015.